KU LEUVEN

FACULTY OF SCIENCE

Analysis of the Dynamics observed at the Solar Coronal Poles by the Extreme Ultraviolet Imager onboard Solar Orbiter

Luka VANREPPELEN

Supervisor:
Prof. Dr. Jasmina Magdalenić Zhukov
CmPa, KU Leuven
SIDC, Royal Observatory of Belgium

Co-supervisor:
Dr. David Berghmans
SIDC, Royal Observatory of Belgium

Thesis presented in
fulfillment of the requirements
for the degree of Master of Science
in Astronomy and Astrophysics

Academic year 2025-2026

Preface

To start, I want to thank my supervisor, Jasmina Magdalenić Zhukov, for giving me the opportunity to work on this topic. The combination of following the Space Weather course while doing my thesis on solar physics really resulted in a very nice experience to learn and to ask questions. And let's not forget the Plasma Physics of the Sun course.

I also want to thank my co-supervisor, David Berghmans, for also giving me the opportunity to work on this project. I want to thank him and all the ROB colleagues for the warm welcome I received while first arriving at ROB. I had a very fun stay and obtained a great educational experience each time at ROB. I also want to thank David for providing the necessary papers for the comparison between my results and state-of-the-art works.

I want to thank both my supervisor and co-supervisor again for giving me constant support and feedback on my work and writing. Without them, it wouldn't be possible for me to submit this thesis as it is right now.

Next, I want to thank my two readers, Dr. Eva Laplace and Dr. Ekaterina Dineva, for gladly taking the time to read my thesis and giving me feedback about the work.

Talking about readers, I want to thank my mom and dad for taking the time (whether or not willingly) to read my thesis, although it probably looks like Chinese to them.

I particularly want to thank my friends, who have stood beside me throughout the entire thesis. They gave me support, ideas, and kept pushing me forward to deliver this work. Special thanks goes to Robbe Schoefs, who needed to listen to all my complaints about my own code not working. Another special thanks goes to Jules Mantels, who pushed me to keep working on something I was stuck on for weeks, only to discover my mistake that same evening. Who knows, without that final push, I wouldn't have found the mistake.

And of course, the most gratitude goes to my parents and sister. I appreciate all they have done for me, and not only during this work.

Luka Vanreppelen

Contribution Statement

The candidate developed all the code used in this thesis and performed all data acquisition, measurements, and analyses of the results reported in Chapters 3-5. The candidate also prepared all original figures, tables, and the manuscript.

Scientific supervision, discussion, and feedback were provided by Prof. Dr. Jasmina Magdalenic Zhukov and Dr. David Berghmans. Both supervisors contributed comments and suggestions that improved the clarity and presentation of the manuscript. Dr. David Berghmans additionally provided guidance regarding relevant literature and references.

Results regarding the small-scale ejections are obtained with the help of my colleague Robbe Schoefs.

Abstract

Keywords: Solar Corona – Solar Orbiter – Extreme Ultraviolet Imager – Solar Coordinate System – Differential Rotation

In this thesis, observations from the Extreme Ultraviolet Imager (EUI) aboard Solar Orbiter were reprojected into an equidistant azimuthal (ARC) coordinate system centered on the solar poles. The reprojection is essential because it minimizes foreshortening effects and enables accurate analysis of coronal structures near the poles. Longitude-time maps were constructed for several heliographic latitudes, and the angular velocities of coronal features were determined by manually tracing persistent structures within these maps.

Statistical analysis showed that the distributions of the measured angular velocities are approximately Gaussian, with small non-Gaussian deviations appearing mainly in the outer quantiles. It was found that the angular velocities systematically decrease with increasing heliographic latitude, and this result generally agrees with other empirical differential rotation laws obtained using the coronal bright point tracers. Moreover, the results obtained in this study also improve and refine the description of the existing differential rotation trends in the Sun's high latitudes, which are prone to the projection effect.

The results demonstrate that polar reprojection of Solar Orbiter's EUI observations provides a robust framework for investigating differential rotation and slow coronal dynamics in the polar regions of the Sun. This study employs novel, out-of-the-ecliptic-plane observations by Solar Orbiter for the first time, in a study of the Sun's differential rotation, and lays the methodology for future studies.

Summary

The Sun is a complex plasma ball that does not rotate as a solid body but exhibits differential rotation, meaning that its angular velocity depends on the heliographic latitude. Equatorial regions rotate significantly faster than the polar regions, causing the solar magnetic field to become twisted and stretched. The magnetic field that emerges to the solar surface is therefore concentrated in the so-called active regions, which are the source of the majority of the solar activity. Eruptions from the Sun, with coronal mass ejections (CMEs) being the most prominent ones, are associated with a large number of physical processes, which we commonly name space weather phenomena.

Historically, the polar regions of the Sun were always difficult to observe due to the predominantly equatorial viewing geometry of the majority of the solar missions. The launch of Solar Orbiter has improved the observational coverage of the solar poles by enabling unique observations from increasingly higher heliographic latitudes.

In this thesis, a processing pipeline was developed that reprojects images obtained by the Extreme Ultraviolet Imager (EUI) aboard Solar Orbiter onto a polar coordinate system in which the solar poles are centered and heliographic latitudes are represented as concentric circles. This reprojection reduces projection effects such as foreshortening and allows accurate studies of the coronal structures situated near the Sun's poles.

Longitude-time maps were constructed from the reprojected data in order to measure the rotational motion of low coronal structures at different latitudes. Angular velocities were determined by manually tracing persistent features in these maps and fitting Gaussian distributions to the resulting measurements. The measured angular velocities were subsequently modeled and compared to existing empirical differential rotation profiles obtained from coronal bright point tracers.

Angular velocities obtained from the EUI observations show a systematic decrease with increasing heliographic latitudes. This result not only globally agrees with the existing trends of the differential rotation rate, but it also improves the accuracy of the differential rotation estimate at the mid to close to the pole latitudes, regions which are generally prone to the strong projection effects.

These results demonstrate that polar reprojections of Solar Orbiter / EUI observations provide a scientifically reliable method for studying rotational dynamics in the solar corona and offer a useful framework for future investigations of polar coronal processes.

Summary for General Audience

The Sun is a giant ball of plasma, a hot, electrically charged gas that behaves much like a fluid, rather than a solid object. On a solid structure like a globe, all latitudes rotate together at the same angular speed. This means that, while the globe spins, each point keeps its relative position with respect to the others. This is not the case with the solar surface due to its gaseous nature. Regions around the equator rotate much faster than regions around the poles, taking respectively around 25 to 34 days for the full rotation. This phenomenon is known as differential rotation. It causes twisting and stretching of the magnetic field of the Sun, ultimately creating magnetic structures, so-called coronal mass ejections (CMEs), that erupt from the Sun. CMEs can impact Earth's atmosphere as the solar plasma neatly follows its magnetic field lines. Solar disturbances can even influence satellites, communication systems, or power grids here on Earth. These complex physical processes with solar origin, to which science efforts are devoted, are called space weather.

The polar regions of the Sun are dominated by the open magnetic field lines along which plasma keeps flowing into interplanetary space, and this phenomenon is known as the solar wind. Until recently, the poles of the Sun were poorly understood due to the unfavorable positioning of instruments and observers (mainly equatorial positions). Presently, with the launch of Solar Orbiter, we can more clearly study the polar regions of the Sun as Solar Orbiter travels out of the equatorial plane, arriving at latitudes of about 30°.

This thesis addresses the complex rotational behavior of the Sun's gaseous atmosphere by first reprojecting every image of Solar Orbiter's Extreme Ultraviolet Imager (EUI) such that the North or South pole is in the center of the image and every latitude is evenly spaced out as concentric circles around the pole. This way, the actual shapes and sizes of structures are visible instead of being cropped and foreshortened. Using this method on the EUI data, we obtain results of differential rotation that not only confirm previous measurements but also improve their accuracy. The thesis results also provide a scientifically correct way to handle solar images and confirm that this method can be applied to study processes happening in the solar corona, which is the outermost, least understood region of the Sun's atmosphere.

Glossary

$\mathring{A}$ Angstrom

au Astronomical Unit

$L_\odot$ Solar Luminosity

$M_\odot$ Solar Mass

$R_\odot$ Solar Radius

ω Angular Velocity

Φ Longitude

σ Standard Deviation

t Time

θ Rotation Angle

Θ Latitude

Acronyms

AIA Atmospheric Imaging Assembly

AR Active Region

ARC Azimuthal Equidistant

CME(s) Coronal Mass Ejection(s)

CRLN Carrington Longitude

EUI Extreme Ultraviolet Imager

EUV Extreme Ultraviolet

FSI Full Sun Imager

HCS Heliospheric Current Sheet

HGC Heliographic Carrington

HGS Heliographic Stonyhurst

HMI Helioseismic and Magnetic Imager

HPC Helioprojective Cartesian

LASCO Large Angle and Spectrometric Coronagraph

LT Longitude-time

Q-Q Quantile-Quantile

SDO Solar Dynamics Observatory

SOHO Solar and Heliospheric Observatory satellite

SolO Solar Orbiter

WCS World Coordinate System

Contents

Chapter 1

Introduction

1.1 Context and Motivation

The Sun has been studied for many decades due to its proximity and fundamental role in the solar system. As the Sun is the star closest to Earth and can be observed in great detail, this being both in space and time, it is also a unique laboratory which we can use to understand stellar physics. Despite the great efforts, numerous key physical processes that describe the Sun's behavior are still not fully understood. This is particularly the situation regarding the processes in Sun's outer atmospheric layer, the so-called corona.

Studying the Sun and the solar atmosphere is not only of theoretical importance but also of practical significance through its influence on the space weather. For example, solar activity, which is driven by the Sun's complex magnetic field, can give rise to energetic phenomena such as solar flares and coronal mass ejections (CMEs). When these energetic phenomena propagate towards the Earth, they can greatly affect satellites in the Earth's vicinity, communication systems, and power grids here on Earth. As such, a deeper understanding of the solar atmosphere and its surrounding dynamics is essential for improving space weather forecasting.

While, in general, the internal structure of the Sun together with its basic mechanisms of energy generation are well known, its outer atmosphere remains poorly understood. In particular, the solar corona, being the outermost layer of the Sun, reaches temperatures of several million Kelvin, significantly exceeding temperatures of the underlying layer. One would expect the temperature to decrease with distance, like a hot pot on a stove. This rather counterintuitive temperature profile gives rise to the so-called coronal heating problem and is one of the most central open questions in solar physics.

Within the solar corona, particular importance is given to the polar regions. These special regions are typically associated with mostly open magnetic fields within the large, long-lived coronal holes, so-called polar coronal holes. It is generally accepted that the coronal holes are the primary source of the fast solar wind propagating along the open magnetic field lines into the inner heliosphere and further. As such, even the large-scale structure of the heliosphere is influenced by the solar wind and its transients originating from the solar coronal poles.

However, due to the predominantly near-ecliptic viewing geometry of all previous solar observations, the polar regions are observed under strong projection effects. Therefore, the interpretation of both structures observed in the polar regions and their dynamics is hindered due to these projection effects. As a consequence, the polar corona still remains way less characterized in comparison to the lower latitude regions of the Sun.

Improving our understanding of the dynamics and structure of the polar coronal regions is thus essential for improving our knowledge of the solar wind formation together with the global solar magnetic field configuration, and accordingly, the global solar activity.

To better understand the significance of the open questions related to the solar coronal poles presented above, it is necessary to present some general properties of the Sun. The Sun's global characteristics, such as the solar mass, radius, and luminosity, provide the basis for both theoretical modeling of the solar atmosphere and the observational interpretation that follows.

1.2 General Properties of the Sun

Our closest star, the Sun, is a G-type main-sequence star, with spectral type G2V. The Sun contains up to approximately 99.86% of the total mass inside the entire solar system (ATNF 2026; NCAR 2026; Ridpath, I 2012; NASA 2023). To this date, its general physical parameters are well known and form the basis for solar and stellar modeling.

For example, the solar mass is approximately (Prša et al. 2016; Cayrel de Strobel 1996)

$$M_{\odot} \approx 1.99 \times 10^{30}\, kg, \tag{1.1}$$

and the mean radius is (Cayrel de Strobel 1996)

$$R_{\odot} \approx 6.96 \times 10^{8}\, m. \tag{1.2}$$

The Sun is located at an average distance of 1 astronomical unit (au) from Earth, which corresponds to (Prša et al. 2016)

$$1\, au \approx 1.496 \times 10^{11}\, m. \tag{1.3}$$

Its luminosity, which represents the total energy output per unit time, is approximately (Cayrel de Strobel 1996)

$$L_{\odot} \approx 3.83 \times 10^{26}\, W. \tag{1.4}$$

For its composition, the Sun's mass consists primarily of hydrogen ($\sim 71\%$ by mass) and helium ($\sim 27.1\%$), with the heavier elements contributing only a small fraction (Nave, R 2024).

While these general parameters describe the Sun as a whole, they do not explain how energy is generated and transported within the Sun's interior. These processes are entirely governed by the Sun's internal structure and the physical conditions that are present in different layers of the Sun's interior (Aerts et al. 2021). To explain the energy generation in the Sun's core and its transport to the surface of the Sun, we turn to a description of the solar interior and the mechanisms that are responsible for these processes.

1.3 Internal Structure of the Sun, Energy Generation, and Energy Transport

The solar interior is regulated by the balance between gravitational forces and pressure gradients together with the energy transport (Aerts et al. 2021; Turck-Chièze et al. 1993). These processes govern how energy is generated within the core and is transported outward to the solar surface and further into the Sun's atmosphere.

For its internal structure, the Sun consists of three main layers: a) core, b) radiative zone, and c) convective zone. These layers are illustrated as a schematic presentation in Figure 1.1a (Interrante et al. 2025). Each of these three internal regions is well characterized by several distinct physical conditions and dominant energy transport mechanisms (Aerts et al. 2021).

In the center of the solar interior lies the very dense, heavy core, which extends to approximately $0.25\ R_{\odot}$ (UCAR 2026). In the Sun's core, temperatures reach values up to about $1.5 \times 10^{7}\ K$, and the density gets so high that it exceeds $150\ g\ cm^{-3}$ (Interrante et al. 2025). Under these extreme conditions, nuclear fusion occurs, which converts hydrogen into helium through the proton-proton (pp) chain (Adelberger et al. 2011). In the process of fusion reactions, energy is released in the form of gamma-ray photons, neutrinos, and kinetic energy. Although the carbon-nitrogen-oxygen (CNO) cycle also contributes to energy generation within the Sun's core, its role is small compared to the pp chain (Adelberger et al. 2011).

Then, surrounding the Sun's core lies the radiative zone, which extends from approximately 0.25 to $0.7\ R_{\odot}$ (UCAR 2026). Within the radiative zone, energy, which is generated within the Sun's core, is transported primarily through radiative diffusion. Here, photons that are produced in the core undergo repeated absorption and re-emission, which results in a very slow outward transfer of energy (Aerts et al. 2021). Due to the high density and opacity of the plasma within this region, a single photon may even take up to 170.000 years to escape the radiative zone (Poletti, S 2020).

Finally, beyond the radiative zone lies the convective zone, the last layer of the Sun's interior. The convective zone extends from roughly $0.7\ R_{\odot}$ up to the visible surface of the Sun at 1 solar radius (UCAR 2026). In this outermost layer of the Sun's interior, the temperature gradient becomes sufficiently steep such that radiative transport is no longer efficient to transport the energy in a stable way (Aerts et al. 2021). Instead, convection takes over, and energy is transported by convective motions.

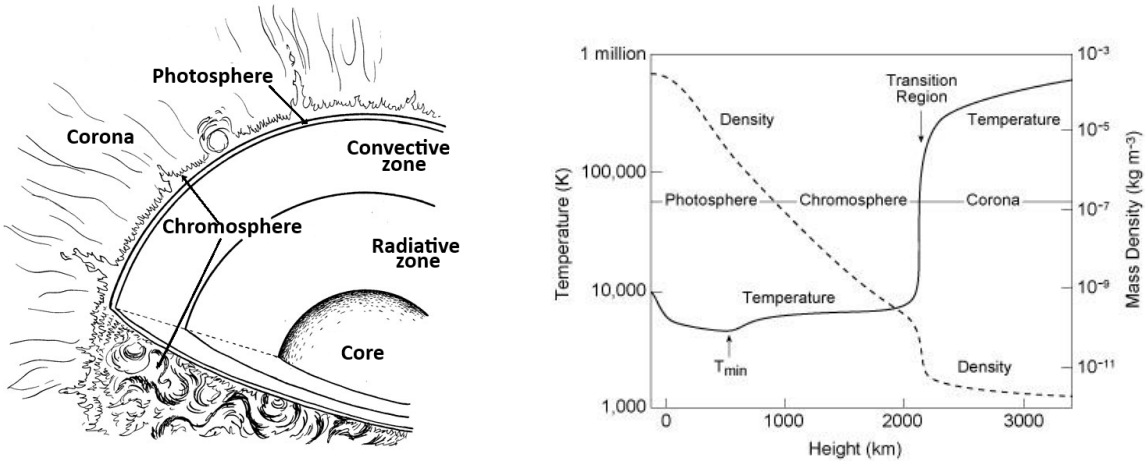

(a) (b)

Figure 1.1: a) Schematic representation of the different layers of the solar interior (Core, Radiative zone, Convective zone) together with the solar atmosphere (Photosphere, Chromosphere, Corona). Source: (Kelley 2019). Each layer is characterized by distinct physical conditions. b) 1D approximation of the temperature profile of the solar atmosphere showing the non-monotonic behavior of the temperature with increasing radial distance from the Sun. Source: (Lang et al. 1999, p. 115). The temperature of the corona jumps from thousands of Kelvin to millions of Kelvin (Interrante et al. 2025). This jump is characterized by the transition region.

Here, hot plasma rises towards the surface, cools, and sinks back down into deeper layers to heat up again. These convective flows give rise to granulation patterns observed at the solar surface (UCAR 2026) and play a crucial role in the generation and evolution of the solar magnetic field through so-called dynamo processes (Schmitt 1993; Miesch 2005), which will be discussed in detail in Sections 1.4 and 1.6.

The transition from radiative to convective energy transport marks an essential change in the dynamics of the solar plasma. While the radiative zone is relatively stable and more stratified, the convective zone consists of highly turbulent and dynamic plasma (Aerts et al. 2021; Schmitt 1993). This turbulent motion is directly linked to the emergence of magnetic fields at the solar surface, which then consequently shape the structure and dynamics of the solar atmosphere (Schmitt 1993; Miesch 2005).

Together with the point that the internal structure of the Sun determines how its energy is transported towards the Sun's surface, it also plays a key role in shaping its large-scale dynamics. In particular, the interaction between convection and internal rotational motions gives rise to the complex rotational behavior of the Sun's surface (Schmitt 1993; Miesch 2005).

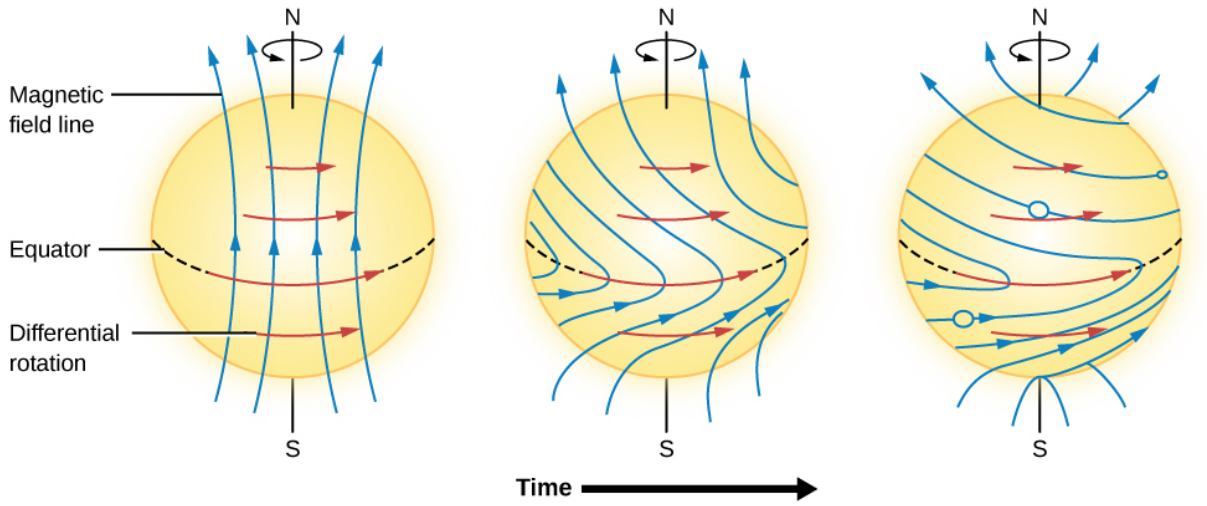

Figure 1.2: Schematic representation of the differential rotation of the Sun. The equatorial regions rotate substantially faster than the polar ones. While equatorial regions take around 25 days to make a full rotation, polar regions can take up to as much as 34 days. Source: (Johns-Krull 2009).

1.4 Solar Rotation and Differential Rotation

The Sun's rotation is not the same across its interior and its atmosphere. Between the radiative and convective zones lies a thin and very important layer of the Sun's interior called the tachocline (Basu et al. 2026). This layer separates regions of the Sun's interior with very different characteristics. The solar interior below the tachocline rotates as a solid body (Basu et al. 2026). In contrast, the Sun's layers above the tachocline rotate differentially. Here, regions of the Sun rotate fundamentally differently from that of a rigid body due to the gaseous, i.e. plasma, nature of the Sun's composition (Beck 2000; Hotta et al. 2022). The rotational velocity of the solar surface is not a uniform value but instead varies with latitude, which is a phenomenon known as differential rotation (Beck 2000; Hotta et al. 2022). The Sun's low latitude regions, i.e. regions close to the Solar equator, rotate faster than areas at higher latitudes, with the rotation rate systematically decreasing as one moves towards the poles. This differential rotation is schematically depicted in Figure 1.2. The unusual rotational behavior of the Sun arises due to the complex interaction between convection, rotation, and magnetic fields deep within the solar interior, as noted earlier (Schmitt 1993; Miesch 2005).

The differential rotation rate of the solar surface is commonly described by an empirical relation of the form (Beck 2000; Snodgrass et al. 1990)

$$\omega(\Theta) = A + B\sin^2\Theta + C\sin^4\Theta, \tag{1.5}$$

where $\omega(\Theta)$ is the angular velocity at heliographic latitude Θ, and A, B, and C are coefficients determined from observations (Snodgrass et al. 1990).

A widely used set of sidereal coefficients (Snodgrass et al. 1990), derived from surface tracers, is given by

$$\begin{aligned} A &= 14.713\,^\circ/day, \\ B &= -2.396\,^\circ/day, \\ C &= -1.787\,^\circ/day. \end{aligned} \tag{1.6}$$

The combination of Equation (1.5) together with the coefficients of Equation (1.6) indicates that the equatorial regions rotate with a period of approximately 25 days, while the rotation period increases significantly toward the poles, even reaching up to 34 days (Beck 2000; Hotta et al. 2022; Snodgrass et al. 1990).

The concept of differential rotation plays a crucial role in the evolution of coronal structures, as it leads to the continuous shearing and redistribution of magnetic field lines across the solar surface (Schmitt 1993; Miesch 2005). In the context of polar observations, the reduced rotation rate influences the apparent motion of features at the solar surface and must be taken into account when interpreting their temporal evolution.

Understanding differential rotation is therefore necessary to analyze time-dependent solar phenomena, in particular when tracking features across multiple observations or constructing longitude-time representations of solar activity, as will be done in this work.

As said, differential rotation has important consequences for the redistribution of plasma and the magnetic field across the solar surface (Schmitt 1993; Miesch 2005). These effects extend beyond the interior and will influence the structure of the overlying atmospheric layers all the way up to the solar corona (Schmitt 1993; Miesch 2005). To understand where and how these processes manifest observationally, we now examine the structure of the solar atmosphere.

1.5 Structure of the Sun's Atmosphere

The solar atmosphere is, similarly to its interior, composed of three distinct layers. Each layer of the solar atmosphere is characterized by different physical conditions described by e.g. density, temperature, and pressure (Aerts et al. 2021; Turck-Chièze et al. 1993). Going from the solar surface outward, these layers are: a) photosphere, b) chromosphere, and c) corona (Interrante et al. 2025). These different layers of the solar atmosphere are illustrated in the schematic presentation of Figure 1.1a.

The first layer of the solar atmosphere, the photosphere, represents the visible surface of the Sun and has a typical temperature of approximately 5800 K (ATNF 2026). Above the photosphere lies the chromosphere, which is a more tenuous layer wherein temperatures initially decrease slightly before rising again to values on the order of 10^4 K (Interrante et al. 2025; Mishra 2022; Bame et al. 1974). The outermost layer of the solar atmosphere, the corona, extends far into interplanetary space and in its lower part even reaches temperatures of several million Kelvin (Interrante et al. 2025; Mishra 2022; Bame et al. 1974) as presented in Figure 1.1b.

This non-monotonic behavior of the temperature profile, in which the temperature steeply increases from the photosphere to the corona, is one of the most "eye-catching characteristics" of the solar atmosphere. The underlying mechanisms responsible for heating the solar corona to these high temperatures remain an open question in solar physics to this day and are commonly referred to as the coronal heating problem (Klimchuk 2006; De Moortel et al. 2015; Kuperus et al. 1981).

As stated above, the various layers of the solar atmosphere have significantly different temperature ranges (Interrante et al. 2025). However, using Wien's law, this means different atmospheric layers will emit radiation at distinct characteristic wavelengths (Ball 2013). As such, observations conducted across multiple wavelengths offer a way to explore different regions of the solar atmosphere and to examine how they interact with one another. An example of using multi-wavelength observations of the different solar layers is shown in Figure 1.3.

Although the solar atmosphere can be described in terms of temperature and density stratification, its true complexity arises from the presence of magnetic fields (Priest 1982). In the outer atmosphere, particularly in the corona, magnetic forces dominate over purely hydrodynamic effects (Gary 2001). This makes the solar magnetic field a central element in understanding the atmospheric structure and dynamics.

1.6 Magnetic Field of the Sun

The Sun's magnetic field fundamentally governs both the structure and the dynamics of the solar atmosphere, as mentioned before (Howard 1967; Wiegelmann et al. 2014; Mackay et al. 2012). In contrast to the lower atmospheric layers, where gas pressure and convection play a dominant role, the corona is characterized by a rather low-density plasma in which magnetic forces dominate and dictate the behavior of the plasma (Gary 2001). As a result, understanding the configuration of the magnetic field is essential to interpret coronal structures and their evolution. As mentioned in Sections 1.3 and 1.4, the magnetic field of the Sun is generated by the dynamo processes operating in the solar interior. These are driven by the interplay between differential rotation and convective motions (Schmitt 1993; Miesch 2005). The magnetic field then emerges through the photosphere and extends into the solar atmosphere, where it governs the structure and the dynamics of the corona (Gary 2001; Howard 1967). To describe the interaction between plasma and magnetic fields in a quantitative way, a theoretical framework is required, which is conveniently provided by the theory of magnetohydrodynamics, see e.g. (Hotta et al. 2022; Moreau 1990).

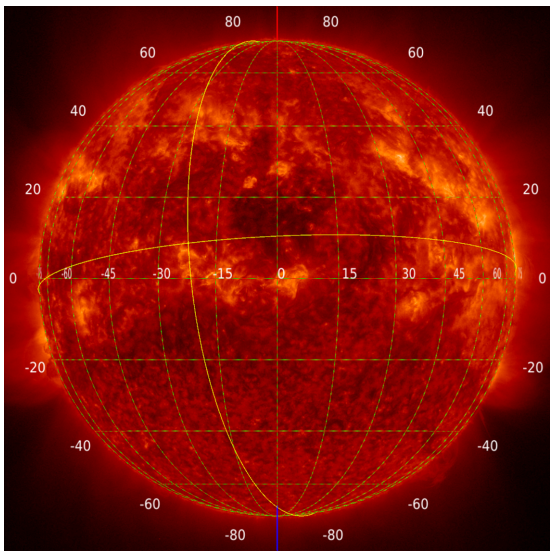

(a) SolO EUI 304 Å

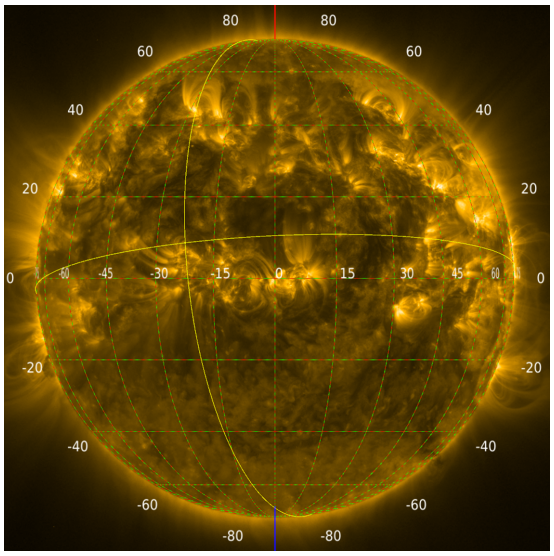

(b) SolO EUI 174 Å

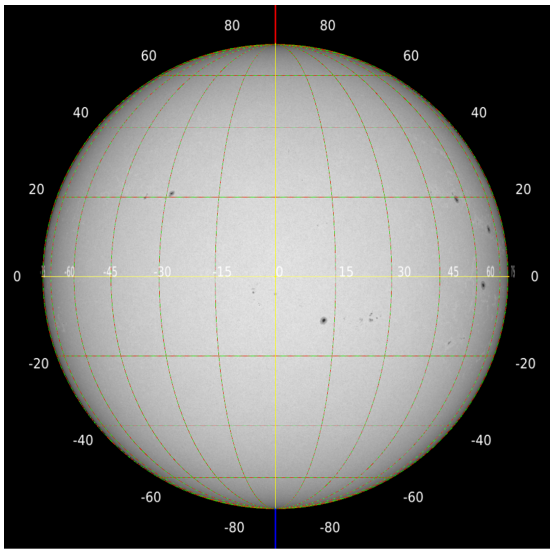

(c) SDO HMI Continuum 6173 Å

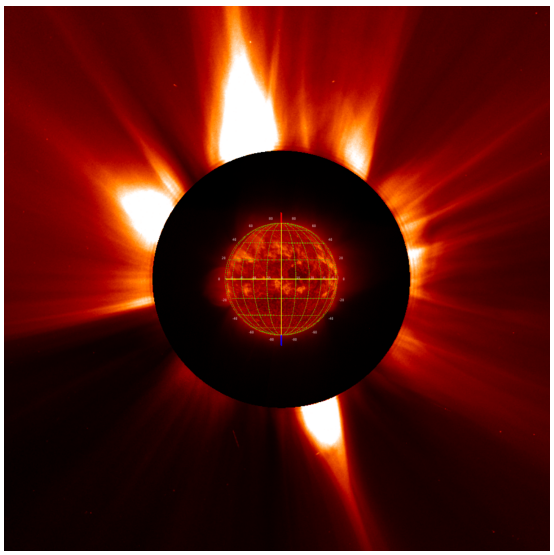

(d) SOHO LASCO C2

Figure 1.3: Multi-wavelength observations of the Sun conducted by SolO EUI/FSI, SDO HMI, and SOHO LASCO on 21 March 2025. a) SolO EUI/FSI (304 Å) probing the chromosphere and transition region, showing filaments and prominences. b) SolO EUI/FSI (174 Å) probing the upper transition region and quiet corona (Rochus et al. 2020). c) SDO HMI (6173 Å) probing the solar surface (Bridgman 2012). d) SOHO LASCO C2 (whitelight) coronograph probing the outer corona (Lamy et al. 2020). All figures created in jHelioviewer (Müller, Nicula, et al. 2017; JHelioviewer - ESA 2017) within the scope of this work.

1.6.1 Frozen-in Conditions and Magnetic Field Dominance

The behavior of plasma residing in the corona can be described within the framework of magnetohydrodynamics (MHD). The MHD theory treats the plasma as a conducting fluid interacting with surrounding magnetic and electric fields. Within this framework, the dynamics of the plasma is governed by a set of coupled equations, including the continuity equation, the momentum equation, and the induction equation (Moreau 1990; Nakariakov 2015; Aschwanden 2005).

$$\frac{\partial \rho}{\partial t} + \nabla \cdot (\rho \mathbf{v}) = 0, \tag{1.7}$$

$$\rho \left(\frac{\partial \mathbf{v}}{\partial t} + \mathbf{v} \cdot \nabla \mathbf{v} \right) + \nabla p - \rho \mathbf{g} - \frac{1}{\mu_0} (\nabla \times \mathbf{B}) = 0, \tag{1.8}$$

$$\frac{\partial p}{\partial t} + \mathbf{v} \cdot \nabla p + \gamma p \nabla \cdot \mathbf{v} = 0, \tag{1.9}$$

$$\frac{\partial \mathbf{B}}{\partial t} - \nabla \times (\mathbf{v} \times \mathbf{B}) = 0, \tag{1.10}$$

$$\nabla \cdot \mathbf{B} = 0. \tag{1.11}$$

where ρ is the plasma density, $\mathbf{v}$ the velocity, p the pressure, $\mathbf{B}$ the magnetic field, and γ the adiabatic index.

A key parameter in determining the relative importance between magnetic and plasma forces is the plasma beta, defined as

$$\beta = \frac{2\mu_0 p}{B^2}, \tag{1.12}$$

which expresses the ratio of the gas pressure to the magnetic pressure. In the solar corona, $\beta \ll 1$, which indicates that the magnetic forces dominate over the pressure forces. This then implies that plasma motions are strongly constrained by the magnetic field within the corona (Gary 2001).

Under these low plasma β conditions, the magnetic field and plasma are closely coupled through the so-called frozen-in condition, which arises from the high electrical conductivity of the plasma (Wiegelmann et al. 2014; Chen et al. 2015). As a result, plasma is prone to flow along the magnetic field lines. Subsequently, the large-scale structure of the corona also reflects the underlying magnetic field configuration. These frozen-in conditions lead to formations of a wide variety of observed features, including coronal loops, plumes, and extended open-field regions, which can be seen in Figure 1.4. As the MHD behavior of the plasma leads to distinct large-scale magnetic configurations in the solar atmosphere, which then determine how plasma is confined or allowed to escape into interplanetary space, it is useful to distinguish between different types of magnetic field structures.

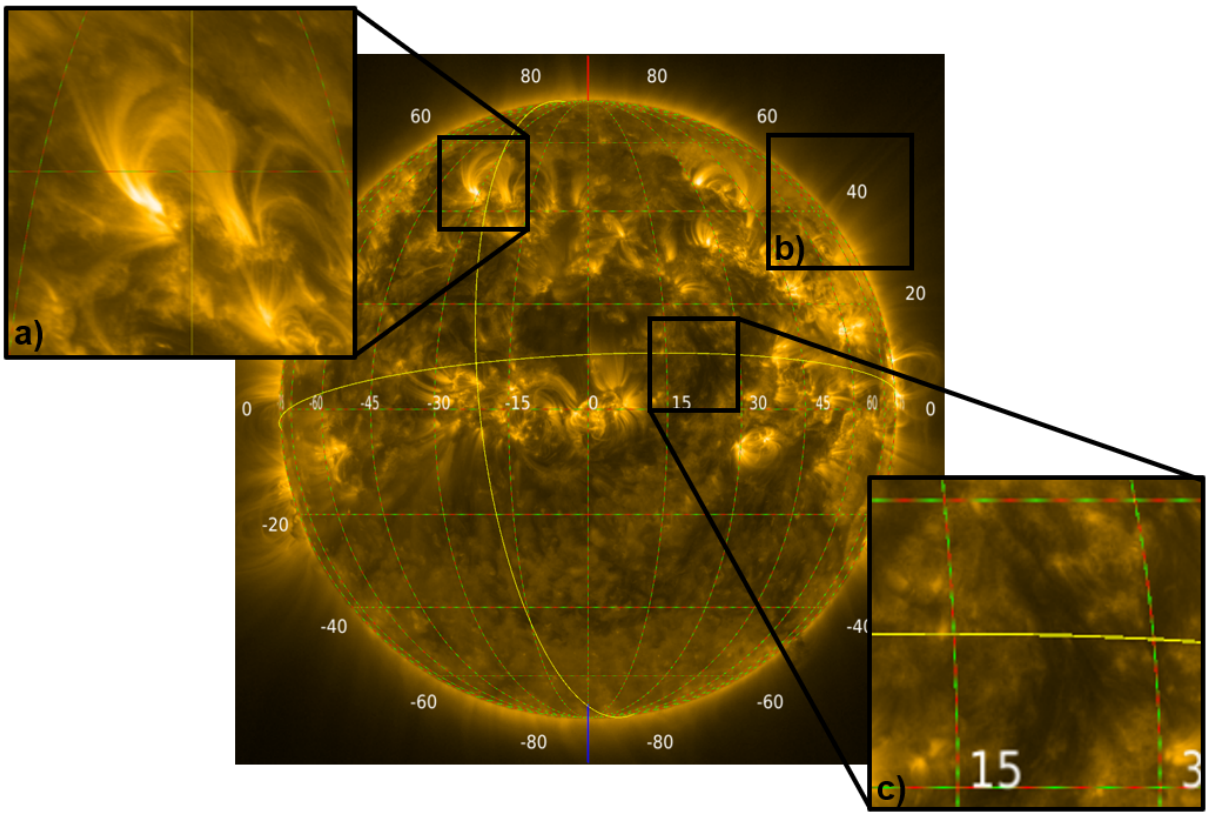

Figure 1.4: Examples of magnetic structures governing the solar atmosphere, taken on 21 March 2025 (SolO EUI/FSI 174 Å). a) Closed magnetic field lines confining plasma. b) Open magnetic field lines extending radially into interplanetary space. c) Magnetic structure (filament) above the solar surface, appearing darker with respect to the background. All figures were created with jHelioviewer (Müller, Nicula, et al. 2017; JHelioviewer - ESA 2017) within the scope of this work.

1.6.2 Open vs Closed Field Regions

While the global magnetic field of the Sun is a dipole, locally the magnetic field of the Sun exhibits both closed and open field configurations (Wiegelmann et al. 2014; Mackay et al. 2012). Closed magnetic field lines are at both ends anchored in the photosphere and form loop-like structures that can confine hot plasma within the corona, as presented in Figure 1.4a. These regions are most frequently associated with enhanced emission and stronger magnetic fields in so-called active regions (ARs) (Wiegelmann et al. 2014; Aschwanden 2005).

In contrast to closed magnetic field lines, open magnetic field lines, as seen in Figure 1.4b, extend outward into interplanetary space and allow plasma to escape along them (Wiegelmann et al. 2014; Mackay et al. 2012). Regions that are dominated by open magnetic field lines are known as coronal holes (Cranmer 2009; Altschuler et al. 1972). Solar coronal holes are characterized by reduced plasma densities and a lower emission in the extreme ultraviolet (EUV) and X-ray wavelengths, and as such, they appear as dark areas in coronal images (Cranmer 2009). Coronal holes play a central role in solar physics, as they are the primary source of the fast solar wind (Cranmer 2009; Altschuler et al. 1972). The fast solar wind is not very dense, and its velocities are of the order of 500 – 800 km s^{-1}, see e.g. Hollweg et al. 2002 and Feldman et al. 2005. We generally distinguish coronal holes depending on their position on the Sun as polar coronal holes, equatorial coronal holes, and low-latitude coronal holes. At the high solar latitudes, particularly during solar minimum, which will be discussed below, large and persistent polar coronal holes are commonly observed (Altschuler et al. 1972), making them key regions for studying the generation of the fast solar wind (Cranmer 2009).

1.6.3 Sunspots

While the large-scale magnetic structures shape the corona, the magnetic fields also manifest themselves clearly at the solar surface. One of the most striking observable signatures of concentrated magnetic flux are sunspots. These are confined regions of the solar photosphere that are characterized by strong magnetic fields and a reduced surface temperature as compared to their surroundings (Borrero et al. 2011; Solanki 2003). As a result of this lower temperature, they appear as dark features (umbra) in visible light observations.

Typically, sunspot regions exhibit magnetic field strengths on the order of 10^3 Gauss, which significantly exceed the average photospheric field, which measures only a couple of hundred Gauss. These strong magnetic fields suppress convective heat transport from the solar interior, which leads to lower temperatures of approximately 4000 K compared to the surrounding photosphere, which measures around 5800 K (See e.g. OpenStax 2017; Solanki 2003).

Characteristically, sunspots occur in pairs or groups with opposite magnetic polarity (Van Driel-Gesztelyi et al. 2015; Bumba et al. 1964; Toriumi and Wang 2019; Toriumi, Schrijver, et al. 2017). These pairs or groups of sunspots are also called active regions, a term introduced in Section 1.6.2.

The top of Figure 1.5 shows the example of AR 4079. The number and distribution of sunspots and ARs vary over the solar cycle (Schmitt 1993; Wiegelmann et al. 2014). Their number increases during the maximum of solar activity and decreases during the solar minimum (OpenStax 2017). Sunspots also systematically migrate towards the solar equator over the course of the solar cycle (Zhang et al. 2018; Kiger 2009), which will be discussed in more detail in Section 1.6.4. This phenomenon is commonly represented in the so-called butterfly diagrams (Zhang et al. 2018; Kiger 2009), an example of which is presented at the bottom of Figure 1.5.

Since the number of sunspots systematically varies over the course of the solar cycle, sunspots serve as important tracers of solar magnetic activity and as such are closely linked to the occurrence of flares, coronal mass ejections (CMEs), and other solar energetic phenomena (Wiegelmann et al. 2014; Mackay et al. 2012). Additionally, sunspots are not randomly distributed in time or space, but instead they follow a well-defined pattern linked to the evolution of the solar magnetic field (Van Driel-Gesztelyi et al. 2015; Bumba et al. 1964; Toriumi and Wang 2019; Toriumi, Schrijver, et al. 2017). Their number, position, and polarity vary systematically over time, and this behavior is further reflected in the solar activity cycle (Schmitt 1993; Wiegelmann et al. 2014).

1.6.4 Solar Activity Cycle

The magnetic field of the Sun evolves on periodic timescales, of which the main one is known as the solar activity cycle (Schmitt 1993; Wiegelmann et al. 2014). This cycle has a typical duration of approximately 11 years (Mackay et al. 2012), and is characterized by the systematic variations of the Sun's magnetic activity. This includes changes in sunspot number, magnetic complexity, and the frequency of eruptive energetic events such as flares and CMEs. This solar activity cycle is presented in Figure 1.6.

One of the fundamental properties of the activity cycle is also the reversal of the Sun's global magnetic field. While the activity cycle spans approximately 11 years, the full magnetic cycle takes twice this time, during which the magnetic polarity returns to its original configuration (Van Driel-Gesztelyi et al. 2015; DeRosa et al. 2012). This flipping of the magnetic field is driven by dynamo processes operating in the solar interior, involving the interaction between differential rotation and convective motions as already discussed earlier (Schmitt 1993; Miesch 2005; Beck 2000; Hotta et al. 2022).

Observationally, the solar cycle is most clearly seen in the distribution of sunspots as mentioned above. At the beginning of each cycle, sunspots and active regions appear at mid-latitudes, and they progressively migrate toward the equator while the cycle advances (Zhang et al. 2018; Kiger 2009). This pattern is commonly represented in butterfly diagrams as previously shown in Figure 1.5. In addition to the migration of sunspots, the magnetic polarity of active regions reverses between two successive cycles, also reflecting the global restructuring of the magnetic field (DeRosa et al. 2012).

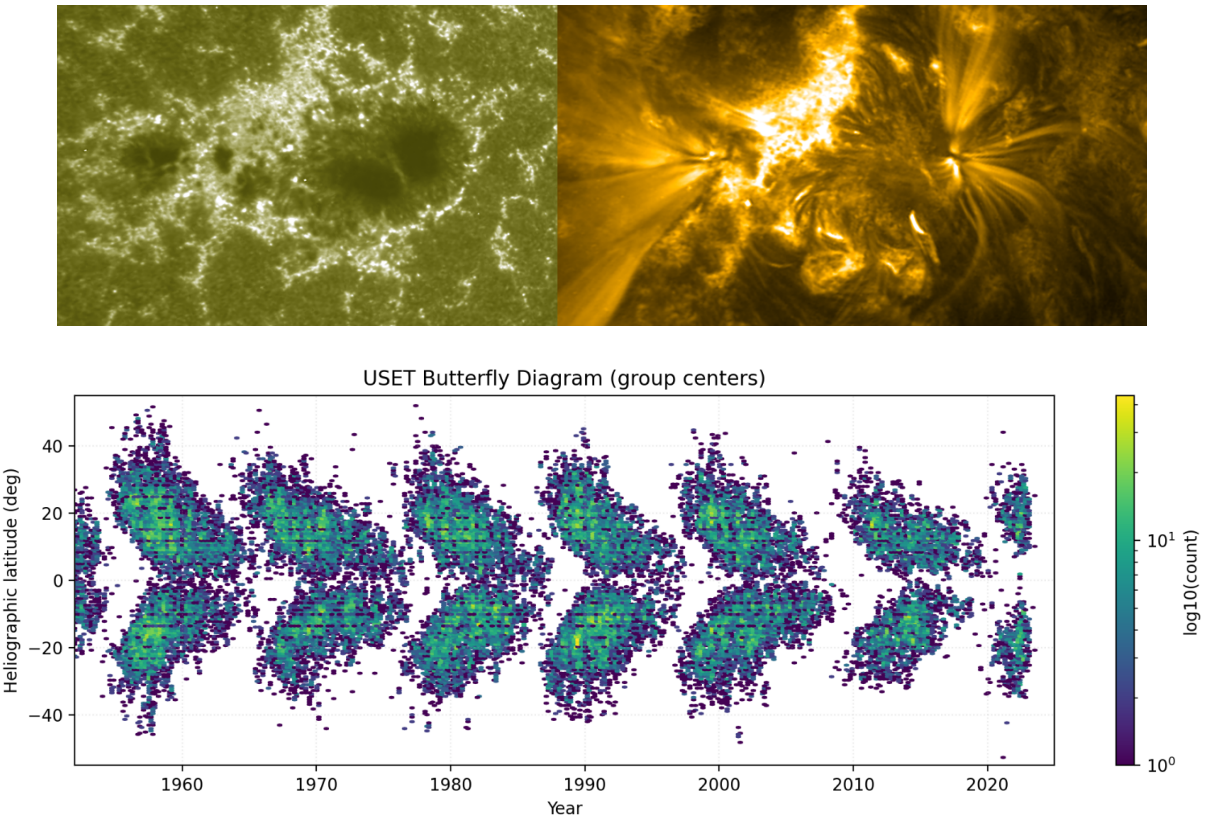

Figure 1.5: Top: Image of active region AR 4079 (2025-05-01) using the SDO AIA 1600 Å channel (left) and the same active region using the SDO AIA 171 Å channel (right). This image shows the plasma following the magnetic field loops. Both images (top left and top right) are created in jHelioviewer (Müller, Nicula, et al. 2017; JHelioviewer - ESA 2017). Bottom: Representation of the evolution of Sunspots with the latitude presented as a function of time. The sunspots' evolution creates a pattern resembling the wings of a butterfly, and it is therefore named the Butterfly diagram. Source: (SIDC 2014).

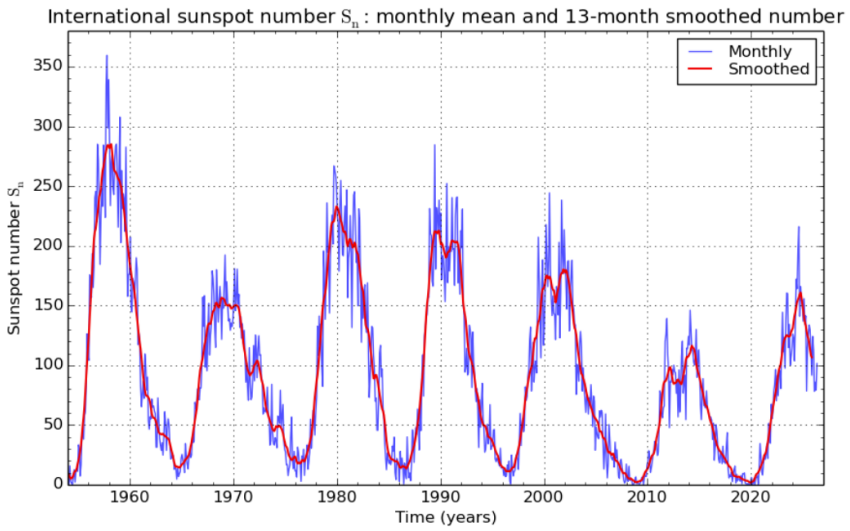

Figure 1.6: Representation of the solar activity cycle through the sunspot number plotted as a function of time. The bright blue curve shows the monthly number of sunspots, while the red curve shows the smoothed version of these measurements. The peaks of the smooth curves represent the solar maxima, while the dips represent the solar minima during the 11-year activity cycle. The considered time interval encompasses six solar cycles and the present ongoing solar cycle. Source: (SIDC 2026).

The solar cycle also strongly influences the large-scale structure of the corona, as already mentioned earlier. On the global scale, the structure of the solar magnetic field extends into the heliosphere and gives rise to the heliospheric current sheet (HCS), which is a thin surface separating the two regions of opposite magnetic polarity (Smith 2001; Hoeksema et al. 1983). The structure of the HCS is shaped by the solar magnetic field and its rotation, and its geometry also varies over the solar cycle. During solar maximum, the magnetic field becomes highly complex and multi-polar, resulting from the increased number of ARs and correspondingly increase of the solar activity across all latitudes (Wiegelmann et al. 2014; Mackay et al. 2012). On the other hand, during solar minimum, the magnetic field is more ordered and symmetrical, with the global dipole field configuration well preserved. This switch in configuration is presented in a schematic way in Figure 1.7. The configuration of the HCS also reflects the large-scale organization of open magnetic field lines and is closely linked to the distribution of coronal holes and the structure of the solar wind (Cranmer 2009; Feldman et al. 2005).

Of particular importance to this work is the evolution of the polar magnetic fields. The polar regions play a key role in the reversal of the global magnetic field. As the cycle progresses, the polar fields weaken, reverse their polarity, and are subsequently rebuilt with opposite polarity (Van Driel-Gesztelyi et al. 2015; DeRosa et al. 2012). The exact and detailed explanation of the solar magnetic field flipping mechanism is still the subject of discussion. The evolution of the solar magnetic field over the activity cycle drives a wide range of dynamic phenomena within the solar atmosphere. These phenomena reflect the continuous buildup and release of magnetic energy, and are collectively referred to as manifestations of solar activity.

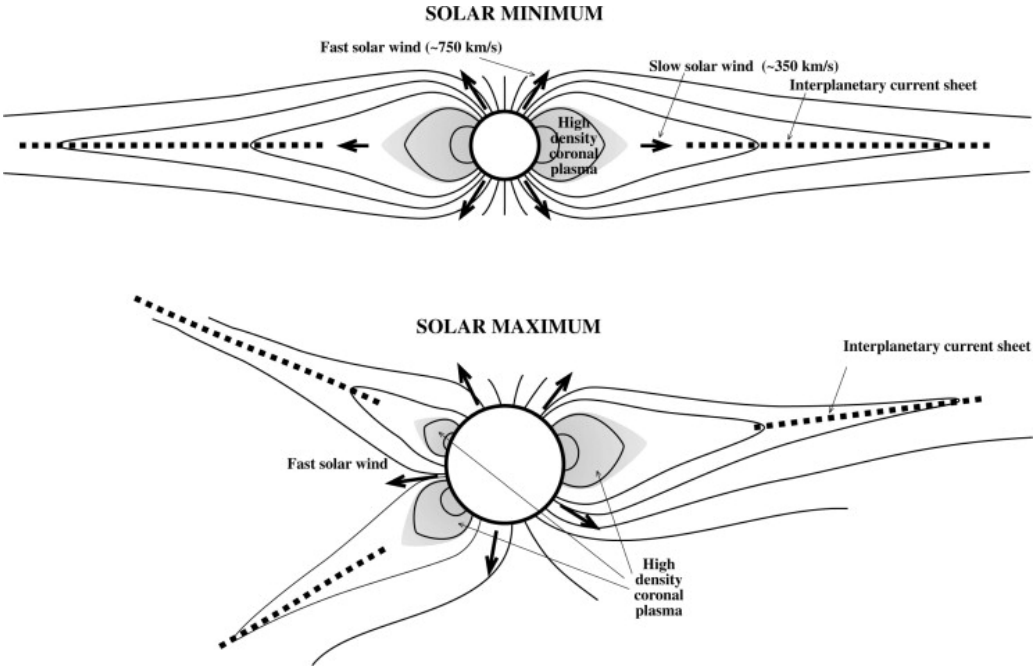

Figure 1.7: The magnetic field of the Sun during solar minimum (Top) and solar maximum (Bottom). Source: (Genç Halit 2021). During solar minimum, the magnetic field is close to being symmetrical, while during solar maximum, it becomes highly complex. The dashed line represents the heliospheric current sheet. At the West and East solar limbs, closed magnetic field lines are visible. At the North and South poles, open magnetic field lines are present.

1.6.5 Manifestations of Solar Activity

As the magnetic activity cycle progresses, the solar magnetic field evolves. This evolution then gives rise to a wide range of dynamic phenomena. These phenomena, which happen primarily in the solar atmosphere, are collectively referred to as solar activity. The main driver behind the solar activity is the storage and release of magnetic energy (Schmitt 1993; Wiegelmann et al. 2014; Mackay et al. 2012).

A direct example of solar activity is the appearance of solar flares. They are one of the most energetic events that can happen in the solar system. They are a result of the magnetic reconnection process during which the magnetic energy is rapidly released (ESA 2022). The process of magnetic reconnection results in the intense emission across the entire electromagnetic spectrum. During these solar flares, plasma is heated, charged particles are often accelerated, and shock waves are generated. The majority of solar flares are associated with CMEs.

CMEs are large-scale events where plasma and magnetic fields are ejected from the solar corona far into interplanetary space (NOAA/SWPC n.d.[a]). These eruptive events can carry vast amounts of mass and energy, and they are a major driver of disturbed space weather conditions. Together with large-scale events such as flares and CMEs, the corona also shows numerous small- and intermediate-scale features. An example of these small dynamic features is spicules. They are narrow, jet-like structures that start in the chromosphere and extend up into the corona. They contribute to

mass and energy transport (SIDC 2023). Another example of more intermediate-scale phenomena is coronal jets. These are fast, narrow outflows of plasma which are often, like flares, associated with the magnetic reconnection, particularly when they appear within coronal holes (Raouafi et al. 2016).

EUV wavelengths are the best way to probe and study these dynamic phenomena that result from the Sun's magnetic activity. The emission from the highly ionized plasma can map different coronal structures and their evolution in the solar atmosphere. Over the course of the activity cycle, the frequency and intensity of these events vary significantly. This behavior links the small-scale dynamics of the corona to the global evolution of the solar magnetic field.

Many of these dynamic processes in the solar atmosphere are most clearly observed in the solar corona, where magnetic structures dominate the behavior of the plasma. The polar regions, in particular, exhibit unique characteristics due to the extensive presence of open magnetic field lines. This makes them especially important for understanding solar dynamics at different scales.

1.7 The Solar Corona and Polar Regions

The corona is typically invisible to the naked eye. It can, however, be observed during total solar eclipses or with the use of a coronagraph such as LASCO (NASA/ESA 2026). These observations reveal that the corona is a highly structured but dynamic plasma environment. In it, flows of charged particles follow the magnetic field lines of the Sun, stated above as the frozen-in condition (Gary 2001; Howard 1967; Wiegelmann et al. 2014; Chen et al. 2015). These magnetic field structures also evolve over the course of the solar cycle. During solar minimum, the corona is structured relatively simple. During solar maximum, on the other hand, it becomes highly complex and dynamic (Van Driel-Gesztelyi et al. 2015; DeRosa et al. 2012).

A feature that is key in the corona is the presence of coronal holes. They are regions that are dominated by open magnetic field lines that extend radially into interplanetary space (Cranmer 2009; Altschuler et al. 1972). In contrast to closed magnetic field regions, open fields allow plasma to escape more easily. As such, coronal holes are therefore associated with lower densities and reduced EUV / X-ray emission, appearing as darker regions in coronal images (Cranmer 2009). These coronal holes are also known to be the primary source of the fast solar wind, with speeds reaching up to approximately 800 km/s (Cranmer 2009; Altschuler et al. 1972; Hollweg et al. 2002; Feldman et al. 2005).

While coronal holes can, in theory, occur at various latitudes and during various phases of the solar cycle, they are particularly noticeable and long-lived in the polar regions, especially during the declining phase of the solar cycle and during solar minimum (Harvey et al. 2002; NOAA/SWPC n.d.[b]). These so-called polar coronal holes can live for several months or years and play a crucial role in shaping the large-scale structure of the solar wind (Harvey et al. 2002; NOAA/SWPC n.d.[b]). Their stability and location at high latitudes make them of particular interest for studies of coronal dynamics and solar wind formation.

Investigating the structure and dynamics of the polar corona requires high-resolution observations with favorable viewing geometries. In this regard, traditional near-ecliptic observations are limited. This then motivates the use of dedicated space missions designed to probe the Sun from new perspectives.

Chapter 2

Observations and Coordinate Systems

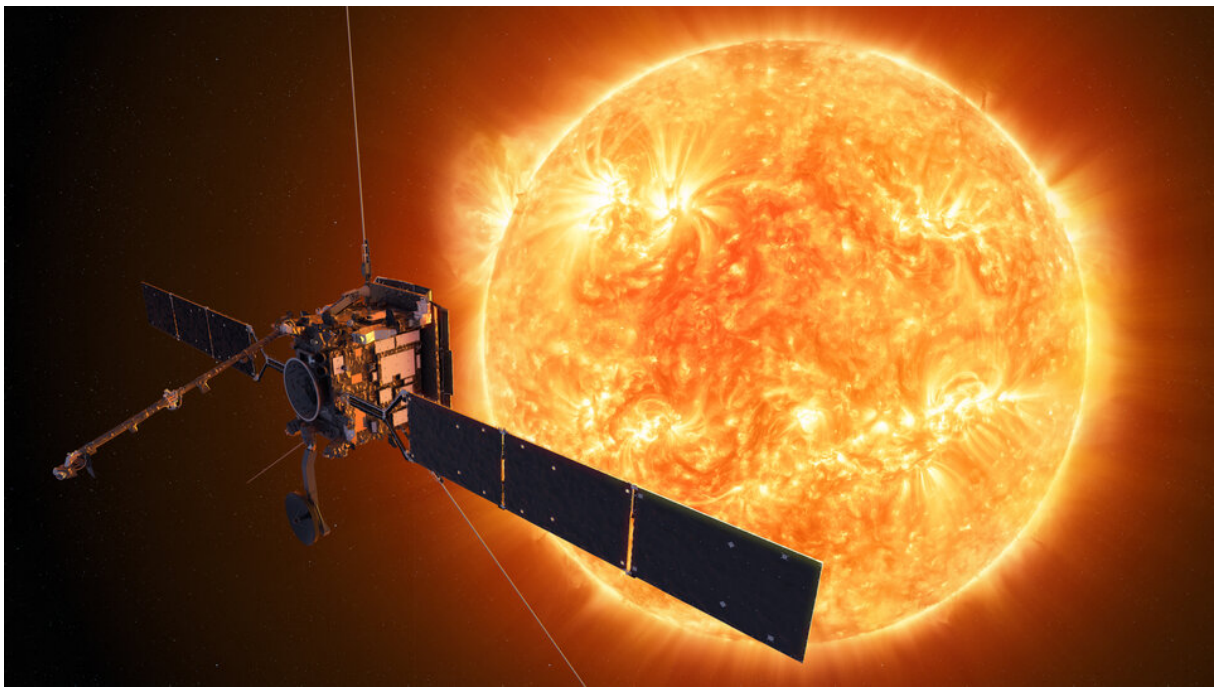

Figure 2.1: Artist impression of Solar Orbiter with the Sun as seen in the EUV wavelength in the background. Source: (ESA 2019)

In this chapter, we briefly introduce the Solar Orbiter observations studied in this thesis. We also highlight the coordinate systems, knowledge of which is essential for the first part of the thesis that focuses on reprojection, which is presented in Chapter 3. We also provide a detailed description of the data that result from the reprojection, as well as the particular way of plotting longitude-time maps.

2.1 Observations: Solar Orbiter and EUI

Solar Orbiter (SolO), as presented in Figure 2.1, is a mission of collaboration between ESA and NASA that is operated by ESA. It is designed to investigate the Sun and heliosphere from different distances from the Sun, and at close proximity and viewing angles like never seen before (ESA 2019). One of its key purposes is to address the fundamental questions that are related to the solar cycle, the origin of the solar wind, and the coronal heating problem (ESA 2019; ESA 2026).

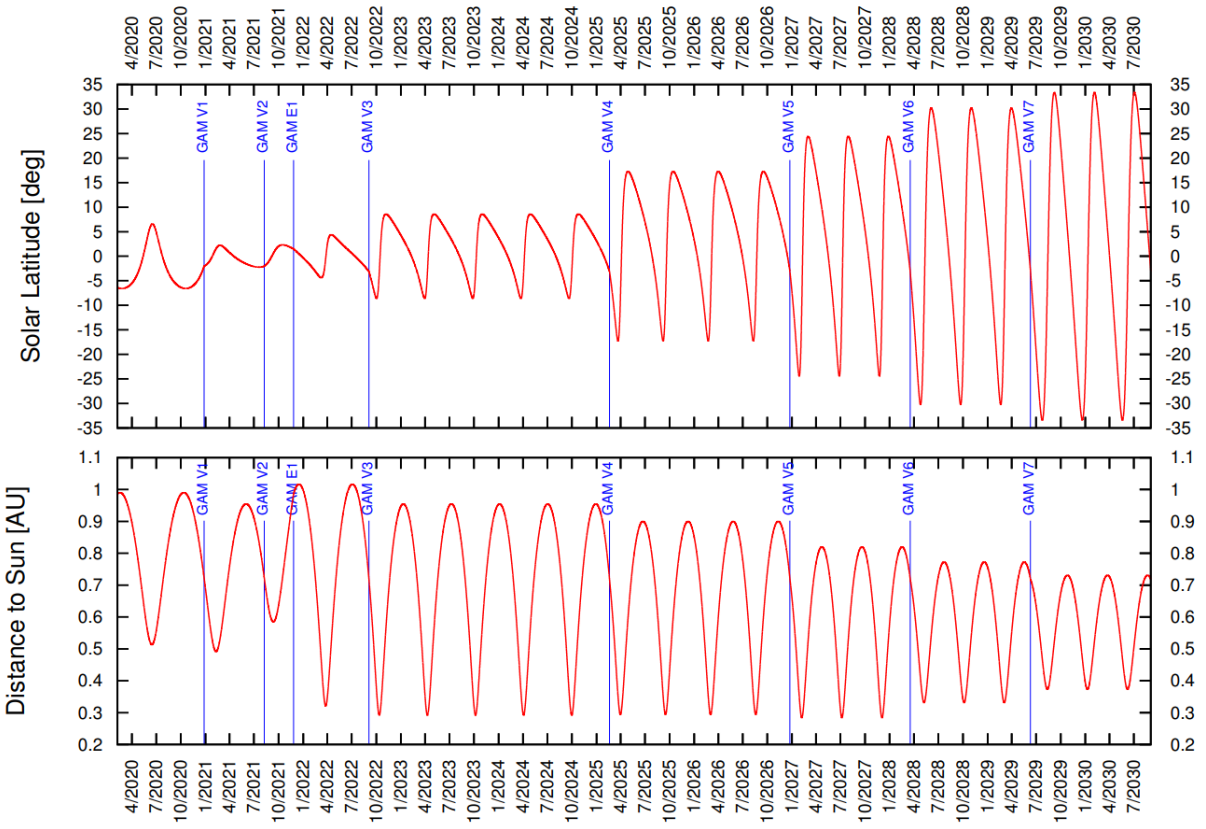

Figure 2.2: Visualization of Solar Orbiter's trajectory. Top: Heliocentric latitude. Bottom: Heliocentric distance. Both plotted in function of time, with the blue vertical lines representing moments of gravitational assists of Earth and Venus. Source: (Müller, St. Cyr, et al. 2020).

In contrast to some other spacecrafts which orbit in Earth's vicinity, such as e.g. the Solar Dynamics Observatory (SDO) (Pesnell et al. 2012), SolO follows a highly elliptical orbit. It is approaching the Sun as close as 0.28 au. Being so close to the Sun, SolO obtains very high-resolution observations of the solar atmosphere (Berghmans et al. 2023). One of the most important key characteristics of SolO is that, together with the close distances to the Sun, it also reaches increasingly higher orbital inclinations, even exceeding 30° as visualized in Figure 2.2 (Müller, St. Cyr, et al. 2020). It needs to be noted that these types of observations have not been performed up to now. This new

viewing angle makes it possible to study the solar coronal poles in greater detail than ever before. Additionally to these remote-sensing observations, SolO also collects in-situ measurements which allow us to investigate the properties of the solar wind and its interactions with the transient phenomena (ESA 2019; ESA 2026).

Among the SolO onboard remote-sensing instruments that show the Sun in great detail is the Extreme Ultraviolet Imager (EUI). EUI is specifically designed to study the structure and the dynamics of the solar atmosphere. It does this at extremely high spatial and temporal resolution (SIDC 2021; Rochus et al. 2020). EUI consists of three telescopes that observe the Sun in the EUV and UV wavelengths. These include 174 Å, 304 Å, and the Lyman-α line (SIDC 2021; Rochus et al. 2020). These three wavelengths correspond to plasma at different characteristic temperatures. This is due to the fact that emission at different wavelengths is directly linked to the energy of the emitting particles in different atmospheric layers (Ball 2013; SIDC 2021; Rochus et al. 2020). In particular, these three wavelengths are sensitive to the plasma at temperatures corresponding to the chromosphere and the corona. As such, these observations enable the investigation of solar phenomena across multiple layers of the solar atmosphere (SIDC 2021; Rochus et al. 2020).

The combination of high-resolution imaging, multi-wavelength observations, and high-latitude viewing angles, like never seen before, makes EUI a very powerful tool for studying the morphology and evolution of coronal structures, particularly in the polar regions.

2.2 Coordinate Systems and Projections Effects

The EUI provides us with high-quality observations of the solar atmosphere. However, the interpretation of these data requires a very precise description of the Sun's and the spacecraft's position in time. This further induces the need for the use of appropriate solar coordinate systems.

Image-based observations of the solar atmosphere require the use of a representable coordinate surface to describe positions. As an image of the Sun is a projection of a 3D object onto a 2D plane, it is necessary to convert positions on the image to physical locations on the surface of the solar sphere. However, unlike a solid body, the Sun lacks fixed reference points to make this conversion easy. Differential rotation even further complicates the description of coordinates. As a result, different coordinate systems are used depending on whether one considers the observer's viewing geometry or the Sun's inherent rotation.

The following subsections address different coordinate systems whose description is based on that of Thompson et al. 2006.

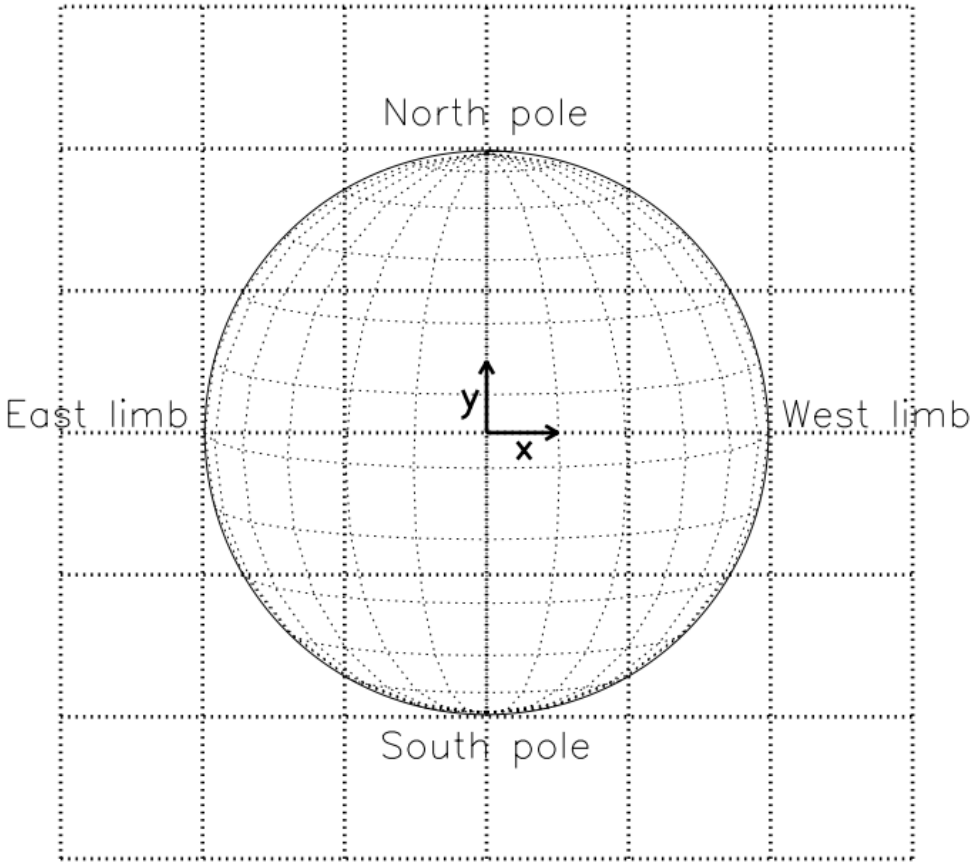

Figure 2.3: Representation of the difference between Helioprojective coordinates (HPC) and Heliographic coordinates (HG). Straight grid lines represent HPC coordinates (expressed in arc sec), while curved lines over the solar surface represent HG coordinates (expressed in longitude and latitude). Source: Thompson et al. 2006.

2.2.1 Helioprojective Cartesian Coordinates - HPC

Solar images obtained from a single point of view, such as SolO, are typically expressed in Helioprojective Cartesian (HPC) coordinates. This coordinate system takes the center of the apparent solar disk as the origin of a 2D grid. Then, each set of coordinates is given by equally spaced angular distances from the center, just like a Cartesian grid, as shown in Figure 2.3. These HPC coordinates are typically expressed as distances in arc seconds (Thompson et al. 2006).

We note that the HPC coordinates are completely observer-dependent as they take the center of the solar disk as seen by that observer as the origin of the projected 2D plane. They also do not take care of the curvature of the solar surface, as coordinates are evenly spaced. As such, they can describe the location of a feature in an image, but they do not provide the physical location on the solar surface and further transformations are required to relate HPC observations to physical solar surface coordinates (Thompson et al. 2006).

2.2.2 Heliographic Coordinates - HG

To obtain physically meaningful positions on the Sun, HPC coordinates are transformed into heliographic (HG) coordinate systems. These coordinates describe locations on the solar surface in terms of latitude Θ and longitude Φ, as presented in Figure 2.3, and can even be extended to three dimensions (3D) by including the radial distance from the Sun's center. This coordinate system can be compared to geographic positions on Earth, where longitude and latitude are also used. Two commonly used heliographic coordinate systems are the Stonyhurst and Carrington systems. These two systems share the same rotational axis but differ in their definitions of longitude (Thompson et al. 2006). While the Earth's surface rotates as a rigid body, the solar surface does not, which makes the definition of longitude arbitrary.

2.2.3 Heliographic Stonyhurst Coordinates - HGS

The Heliographic Stonyhurst (HGS) coordinate system is defined in such a way that the longitude $\Phi = 0^\circ$ corresponds to the central meridian as seen by an observer on Earth at a given time. As a consequence, the longitude grid moves with respect to solar features as the Sun rotates (Figure 2.4 and Thompson et al. 2006).

HGS coordinates are particularly useful for describing instantaneous observations, as they provide a direct mapping between image coordinates and locations on the solar surface. However, because the reference frame is tied to the Earth-facing central meridian, the time-dependency of the longitude of a given feature comes into play (Thompson et al. 2006).

2.2.4 Heliographic Carrington Coordinates - HGC

In order to mitigate the time dependence of the longitude in the case of HGS coordinates, a new set of coordinates, the so-called Heliographic Carrington (HGC) system, is introduced. In contrast to HGS coordinates, the HGC system defines longitude in a frame that co-rotates with the Sun. Rotating with a period of 27.2753 days, it provides a nearly fixed reference frame for tracking solar features over time (Thompson et al. 2006).

The Carrington longitude Φ_C is related to the Stonyhurst longitude Φ through a time-dependent offset:

$$\Phi_C = \Phi + L_0, \tag{2.1}$$

where L_0 is the Carrington longitude of the central meridian as seen by the observer. This transformation ensures a consistent tracking of features across multiple observations (Thompson et al. 2006).

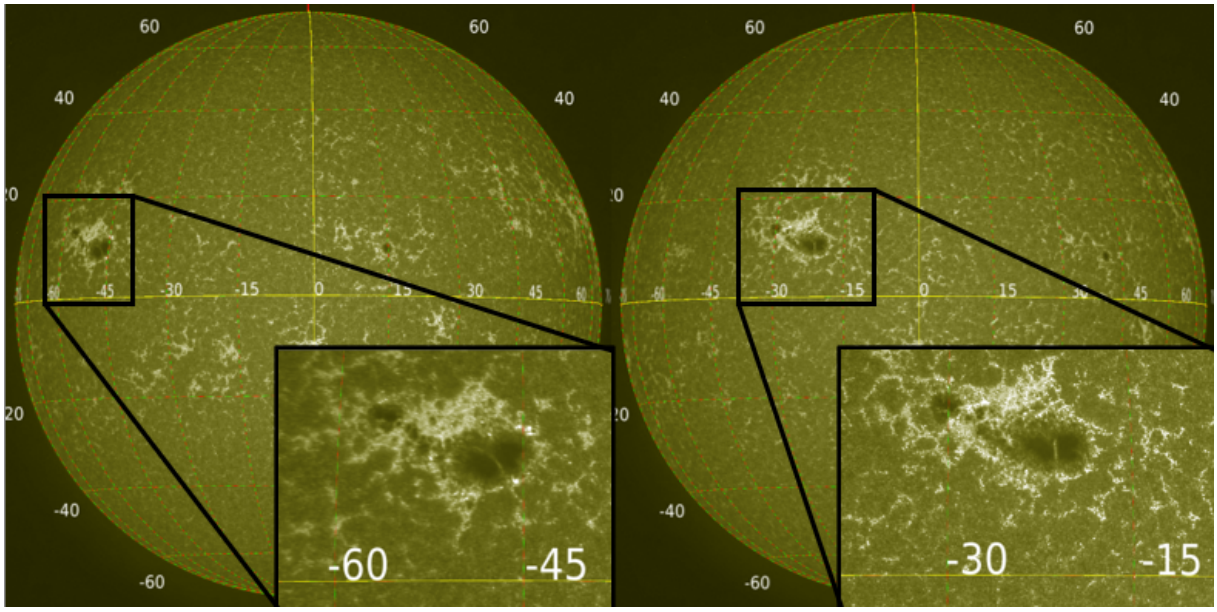

Figure 2.4: Images generated in JHelioviewer (Müller, Nicula, et al. 2017; JHelioviewer - ESA 2017) within the scope of this work using the SDO AIA 1600 Å channel, showing the time dependence of Stonyhurst coordinates. Left: AR 4079 is located between -60° and -45° longitude (2025-05-01). Right: The same AR 4079 now located at around -30° longitude (2025-05-03). Carrington coordinates mitigate this time dependence and keep a relatively fixed position on the coordinate grid.

2.2.5 Coordinate Systems in Practice

In practice, solar observations are typically obtained in HPC coordinates. As such, they need to be transformed into other systems to obtain a physically meaningful position on the solar surface. While HGS coordinates are good in describing instantaneous observations as stated earlier, the HGC coordinates provide a co-rotating frame that allows solar features to be tracked consistently over time (Thompson et al. 2006).

Even when expressed in well-defined coordinate systems such as HGC coordinates, solar observations still remain affected by projection effects due to the viewing geometry. These effects will distort the apparent shape and position of solar features, particularly near the limb and poles. To address this, additional processing techniques are required.

2.3 Image Reprojection for Polar Analysis

Images of the Sun, no matter which coordinates they are expressed in, are inherently affected by foreshortening. This is due to the fact that they represent a two-dimensional view of a three-dimensional structure. Features that are located far away from the Sun's center are, as such, subject to geometric distortions, and they will look smaller than they actually are. This leads to apparent sizes and shapes that completely differ from their true spatial extent.

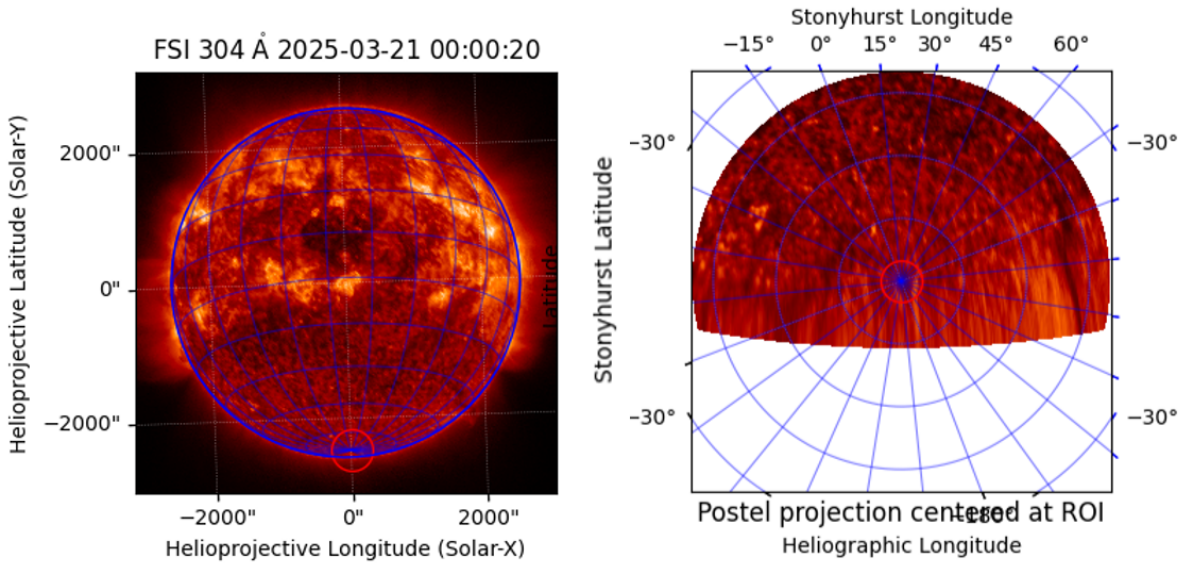

Figure 2.5: Azimuthal equidistant projection (ARC) (Wikipedia 2026a; Snyder 1993) where the South pole of the Sun (left) is reprojected to be in the center of the image (right). Image obtained from SolO EUI/FSI using the 304 Å channel and created within the scope of this work.

In previous solar missions and observations, these effects were especially noticeable towards the polar regions as they were observed at an oblique angle. This again emphasizes the impact SolO's observations will have when they are taken from its high-latitude orbit.

To overcome these limitations of foreshortening of the poles, image reprojection techniques are employed to convert observational data from HPC coordinates into different coordinate systems that more accurately present the positions on the solar surface. This process involves mapping the observed data onto a new coordinate grid, usually based on heliographic coordinates. By doing so, it reduces distortions caused by projection and allows for a more meaningful interpretation of the data.

A common approach is to reproject images onto a latitude-longitude grid using projections that better preserve geometric relationships on the solar surface. In this work, an azimuthal equidistant (ARC) projection is employed, in which distances from a chosen central point are preserved along great circles (Wikipedia 2026a; Snyder 1993), as seen in Figure 2.5. When centered on the solar poles, this projection provides a natural representation of high-latitude regions, reducing the severe foreshortening present in the original image coordinates.

This technique of reprojecting images enables the construction of time-dependent maps, which can be used to analyze the rotational evolution of solar features. These can be particularly suitable for studying radial and rotational patterns around the poles.

Once projection effects have been minimized through reprojection, the data can be analyzed in a more physically meaningful way. In particular, it becomes possible to consistently and accurately study the temporal evolution of different solar structures. A powerful tool for this purpose is the construction of longitude-time maps.

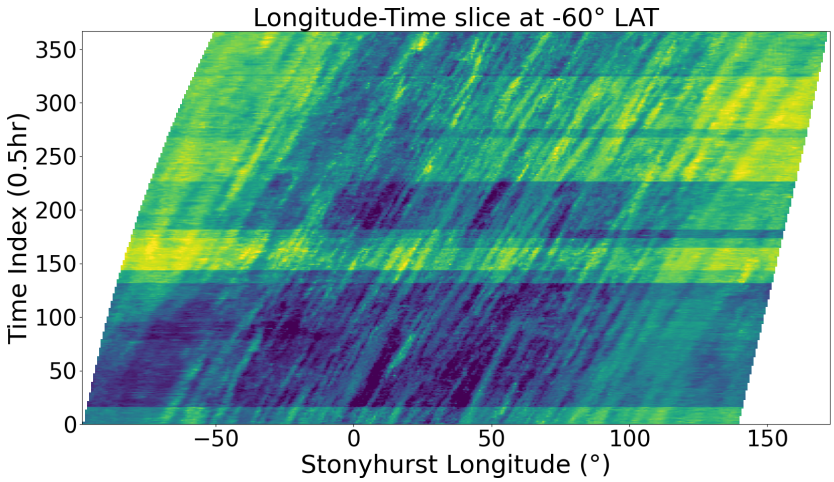

Figure 2.6: Example of a longitude-time map extracted at a heliographic latitude of -60° using the pipeline adopted in this work. The horizontal axis represents heliographic longitude, while the vertical axis shows time in units of 30 minutes. Diagonal lines correspond to the temporal evolution of coronal structures.

2.4 Longitude-Time Maps

Longitude-time maps are a good way to analyze the temporal evolution of solar features (Sheeley et al. 1999; Davies et al. 2009; Conlon et al. 2014; Plotnikov et al. 2016). In the remainder of this thesis, longitude-time maps will be referenced to as LT maps. An example of such an LT map is presented in Figure 2.6. Maps such as these are created by stacking images in time, creating a three-dimensional so-called data cube. This produces a three-dimensional representation where two axes correspond to longitude and latitude, and the third axis corresponds to time (Sheeley et al. 1999; Davies et al. 2009). An LT map is obtained by taking a slice through the data cube at a fixed latitude.

Generally, such LT maps are typically generated from reprojected data expressed in heliographic coordinates. This ensures that the spatial dimensions will correspond to physically meaningful positions on the solar surface. By fixing a given latitude range or averaging over a narrow latitudinal band, the resulting map then highlights the longitudinal evolution of structures as the Sun rotates. Such a representation effectively transforms the rotational motion of solar features into linear patterns, as can be seen in Figure 2.6. LT maps provide, therefore, a straightforward visualization of the rotation of solar structures in the low corona.

2.4.1 Interpretation of Longitude-Time Maps

In an LT map such as seen in Figure 2.6, persistent solar features appear as elongated lines whose orientation reflects their apparent motion. The slope of these lines is directly related to the angular velocity of the corresponding structures, with steeper slopes indicating slower longitudinal motion when time is represented on the y-axis of the two-dimensional map.

For features co-rotating with the Sun, the observed slopes are governed by the rate of the solar rotation, which varies with latitude due to differential rotation as explained above (Hotta et al. 2022; OpenStax 2017). As a result, the inclination of lines in LT maps provides a direct diagnosis of rotational dynamics. Deviations from the expected linear slope may indicate additional effects such as parallax of features at enhanced height above the solar surface.

LT maps are particularly well-suited for studying the rotational behavior and evolution of coronal features (Sheeley et al. 1999; Davies et al. 2009), especially when combined with reprojection techniques that minimize geometric distortion. In the context of polar observations, they provide a valuable means of quantifying the motion of high-latitude structures and relating it to the Sun's underlying differential rotation.

Chapter 3

Reprojection of the Solar Orbiter Polar Observations

This section describes the data-processing pipeline adopted in the herein presented work, from data acquisition to the final use of the processed observations. First, the acquisition of Solar Orbiter data obtained with the Extreme Ultraviolet Imager (EUI) is presented. Next, the preparation of the data is outlined, including image derotation, spatial centering, and the selection of a region of interest, being the poles in this case. Subsequently, the data reprojection onto a common coordinate system is explained. Finally, it is detailed how the reprojected data are used for further analysis, which is presented in the follow-up Chapters 4 and 5.

All the data processing and analysis are performed using Python and, in particular, with the extensive use of the *SunPy* library. SunPy is a community-developed, open-source Python package specifically designed for solar physics research (The SunPy Community et al. 2020). It provides standardized tools for handling solar data, performing coordinate transformations, and processing observations from a wide range of solar instruments, including SolO.

3.1 Data Acquisition

The first step in the data-preparation pipeline needed for the study of Sun's differential rotation is to acquire suitable observations that capture the solar coronal structures with sufficient spatial and temporal resolution. The observational data used in this work are obtained from the EUI instrument onboard the SolO. The EUI instrument provides high-resolution observations of the solar atmosphere in several extreme ultraviolet wavelength bands, enabling detailed studies of coronal structures and their temporal evolution.

All Solar Orbiter data products are stored in a centralized data archive and can be accessed through standardized query interfaces. Instead of manually downloading individual files, data acquisition is automated using *Fido*, SunPy's unified data search and retrieval interface (SunPy n.d.[a]). Fido provides a high-level abstraction that allows users to query multiple solar data repositories using a consistent syntax.

To retrieve the required data, a query is constructed specifying a time range of interest, the observing instrument (EUI), the desired wavelength channel, and the data processing level. Once the query is submitted, Fido searches the relevant archives for matching data products and returns a list of available files. In this work, we focus on processing level L2 data from the Full Sun Imager (FSI) and the High Resolution Imager (HRI) at wavelengths of 174 Å and 304 Å. In the case of L2 data, all images were corrected by the instrument team for all known instrumental defects, such as correcting flat field deviations and removing distortions. For measuring differential rotation (see Chapter 4), we use a cadence of either 30 or 60 minutes over several days. In contrast, for small-scale ejection measurements, we reduce this cadence to a few seconds to accurately capture short-lived features. All measurements were taken during time periods when the Solar Orbiter reached high absolute latitudes (2025-05). The files that meet these criteria are then downloaded locally as FITS (Flexible Image Transport System) files and stored for further processing Group et al. 2016.

Using Fido ensures that the data acquisition process is reproducible and easily adaptable. Changes to the time interval, wavelength, or processing level can be implemented by modifying only a small number of query parameters, which is particularly useful for comparative studies or for extending the analysis to additional datasets.

3.2 Data Preprocessing

After acquiring data, several preprocessing steps are necessary in order to ensure that all observations share a consistent spatial orientation, reference frame, and field of view. This standardization is essential for meaningful comparisons between consecutive images and for reliable tracking of the temporal evolution of solar structures.

All preprocessing is performed using the *Map* framework provided by the SunPy library (SunPy n.d.[b]). A SunPy map is a data structure that combines the image data with its associated metadata, including coordinate information, instrument pointing, and pixel scale. By converting each FITS file obtained with Fido into a SunPy map, the observational data can be handled in a physically meaningful coordinate system and can be visualized in a straightforward, reproducible manner. Throughout this work, each EUI observation is therefore treated as a SunPy map.

3.3 Image Derotation

The first step in this preprocessing pipeline is correcting image orientation via derotation. Due to variations in spacecraft orientation and instrument pointing, the EUI images are not necessarily aligned in a uniform reference frame. To correct for this, each image is derotated as a first preprocessing step. The required rotation angle is obtained from the rotation matrix M_R stored in each file's metadata. For a two-dimensional rotation, the M_R matrix takes the form

$$M_R = \begin{pmatrix} \cos\theta & -\sin\theta \\ \sin\theta & \cos\theta \end{pmatrix} \tag{3.1}$$

where θ is the rotation angle.

By extracting the appropriate components of this matrix, the rotation angle θ is computed using the *atan2* function in Python, which ensures the correct sign and quadrant of the angle. A simple script then determines whether the rotation is clockwise or counterclockwise, after which the image is derotated accordingly using the SunPy *rotate* functionality (SunPy n.d.[c]). This procedure ensures that all images share a consistent orientation, facilitating direct visual and quantitative comparison.

3.4 Centering and Field-of-view Selection

Once all images share a consistent orientation, the next step is to ensure they are aligned with a common spatial reference. Therefore, following derotation, each image is centered on the solar disk. In the original data, the apparent center of the Sun is not always at the image center. Such offsets complicate the comparison of subsequent observations. To address this, all images are recentered on the solar disk center.

SunPy represents solar coordinates in arc seconds (HPC coordinates) relative to the center of the Sun, which is defined as $(0'', 0'')$. This allows the solar center to serve as a natural reference point for image centering. Using this HPC system, each map is recentered by constructing a *submap* around the solar center (SunPy n.d.[d]).

To ensure a consistent physical field of view across all observations, the apparent solar radius in arc seconds is calculated for each image. The submap is then defined using this radius, such that the full solar disk is included. For visualization purposes and to retain a limited off-limb region, a slightly larger field of view is selected. In this work, an outer boundary corresponding to $7/6$ times the solar radius is used. This choice preserves contextual coronal structures beyond the limb while maintaining uniform image dimensions across the dataset.

While this step ensures a consistent field of view, the polar regions of interest are still subject to strong projection effects. This necessitates an additional transformation on the data.

3.5 Reprojection

The reprojection of the EUI observations is one of the most critical steps in the data preprocessing. Although Solar Orbiter reaches increasingly high heliographic latitudes during its mission, the spacecraft is not positioned directly above the solar poles. Consequently, the polar regions of interest are not located at the center of the original images. In the early phases of the mission, when Solar Orbiter remained at relatively low heliographic latitudes, the poles were often only marginally visible near the solar limb. To enable a consistent and detailed analysis of the polar regions, the images must be reprojected so that the visible pole is placed at the center of the field of view.

The first step in this procedure is to determine which solar pole is visible in a given observation. This is accomplished by inspecting the Carrington latitude of the observer, stored in the map's metadata. A positive observer latitude indicates that the spacecraft is located in the northern heliographic hemisphere and that the north solar pole is visible, whereas a negative observer latitude indicates that the spacecraft is in the southern hemisphere and that the south solar pole is visible.

Following the identification of the visible pole, the Carrington longitude of the observer CRLN_OBS is retrieved from the metadata. A new coordinate origin corresponding to the relevant solar pole is then defined. For the Sun's North Pole, this origin is given by $(\mathrm{CRLN\_OBS}^\circ, 90^\circ)$, for the South Pole it is given by $(\mathrm{CRLN\_OBS}^\circ, -90^\circ)$. The coordinate is constructed using the *SkyCoord* class from the *Astropy* library (Astropy n.d.[a]), adopting the Heliographic Carrington reference frame.

The actual reprojection is performed by defining the target map geometry, including the desired image dimensions (1500×1500 pixels), the newly defined pole-centered coordinate origin, an appropriate pixel-to-degree scale, and the projection method. An azimuthal equidistant (ARC) projection is chosen, as it naturally places the pole at the center of the image and preserves equal angular spacing in latitude as a function of radial distance from the pole. This projection is particularly well-suited for studying polar regions, where latitudinal structure is of primary interest. It needs to be noted that this reprojection involves mapping a two-dimensional projection of a spherical surface onto a different two-dimensional plane. As a result, some reprojection artifacts are unavoidable, especially at larger angular distances from the original center. These effects are taken into account in the interpretation of the results.

After the reprojection, the resulting maps are further cropped to enhance the visibility of the polar regions. This is achieved by masking out latitudes more than 50° away from the pole. For the Sun's North Pole, this corresponds to retaining latitudes between 40° and 90°, with the outermost circle in the image representing 40° latitude and the pole at 90° located at the image center. The same procedure is applied analogously for the Sun's South Pole. This final step ensures a uniform and focused view of the polar regions across all observations.

As a result of the described preprocessing steps, the dataset consists of a sequence of uniformly processed, pole-centered images. These images can then be combined into a time-dependent data structure for further analysis.

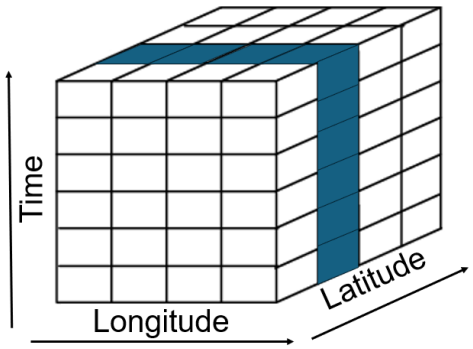

Figure 3.1: The simplified schematic representation of the data cube construction. Two spatial dimensions represent heliographic longitude and latitude, while one dimension represents time. The blue annotation represents a data cube slice at fixed heliographic latitude. Figure created within the framework of this project.

3.6 Data cubes and Slices

After preprocessing and reprojection, the resulting pole-centered images are used to construct a time-dependent representation of the polar regions. This representation serves as the basis for analyzing the temporal evolution of solar structures and the estimation of the differential rotation rate.

To achieve this, the processed images are first combined into a three-dimensional data structure, commonly referred to as a *data cube*. Within this data cube, the two spatial dimensions correspond to the heliographic coordinates in the reprojected polar maps, while the third dimension represents time. Once the data cube has been constructed, slices at fixed heliographic latitudes can be extracted. These slices allow the motion of solar structures along the longitudinal direction to be tracked over time. When visualized as longitude-time diagrams, such slices produce our so-called LT-maps, which are widely used to study the propagation and rotational motion of solar features.

3.6.1 Data cube Construction

The first step in this process is constructing the data cube itself, which is constructed by stacking all reprojected images along the temporal axis. Before stacking, the images are sorted chronologically to preserve the temporal evolution of the observed structures. Because all images have been uniformly processed, i.e., sharing the same orientation, coordinate system, projection, and field of view, the resulting data cube provides a consistent representation of the polar regions across the entire dataset.

Each layer of the data cube, therefore, corresponds to a single observation at a specific time, while successive layers represent the temporal progression of the solar polar region. This data cube construction is presented schematically in Figure 3.1. Navigating through the data cube thus reveals the continuous evolution of the polar structures within approximately 50° of the solar pole, which is arbitrarily chosen.

3.6.2 Determination of Latitude Coordinates

To extract slices at specific heliographic latitudes, it is first necessary to determine how heliographic coordinates correspond to pixel locations within the reprojected maps. This relationship is obtained using the World Coordinate System (WCS) information associated with the maps (Astropy n.d.[b]).

A grid of pixel coordinates is constructed and converted to heliographic coordinates using the *pixel_to_world* transformation provided by SunPy (SunPy n.d.[e]). This transformation maps pixel indices to physical coordinates expressed in degrees of longitude and latitude. Although all the reprojected images share identical WCS information, this transformation needs to be computed for each image as Solar Orbiter moves through space and experiences different tilts and positions at different time steps. We note that for this additional computation, a significant amount of time was needed. With the help of this transformation, two two-dimensional arrays are constructed describing the heliographic longitude and latitude associated with each pixel in the image. These arrays form longitude and latitude grids that can be used to identify pixels corresponding to a desired heliographic latitude.

Since lines of a constant latitude form concentric circles in the polar projection, it is generally not possible to select pixels corresponding to a single exact latitude. Instead, a small tolerance interval of, for example, 0.05-0.2° is introduced around the target latitude. A mask is then constructed according to

$$\text{mask} = |\text{lat}_{grid} - \text{lat}_{target}| < \text{tolerance}, \tag{3.2}$$

which selects all pixels whose latitude lies within the specified interval around the chosen latitude. Applying this mask identifies the pixels that contribute to the latitude slice. The corresponding longitudes can then be extracted and sorted, allowing the total longitudinal coverage of the slice to be determined. For latitudes away from the pole, the resulting longitude span is typically smaller than 360°, reflecting the limited angular coverage of the observations. This limitation is shown in Figure 3.2. It is clear that at very high latitudes, the longitude span approaches 360°, while this significantly decreases towards lower latitude values.

Once this mapping is established, slices corresponding to specific heliographic latitudes can be extracted.

3.6.3 Extracting Longitude-Time Slice

When the pixels corresponding to a selected latitude range are identified, the next step is to extract the temporal evolution of these pixels across the entire dataset. To construct such a map, the spatial dimensions of the data cube are first reorganized in such a way that each time frame is represented as a one-dimensional array containing all spatial pixels. The previously constructed latitude mask is then applied to this flattened spatial dimension. In doing so, only the pixels belonging to the selected latitude band are retained for each time step.

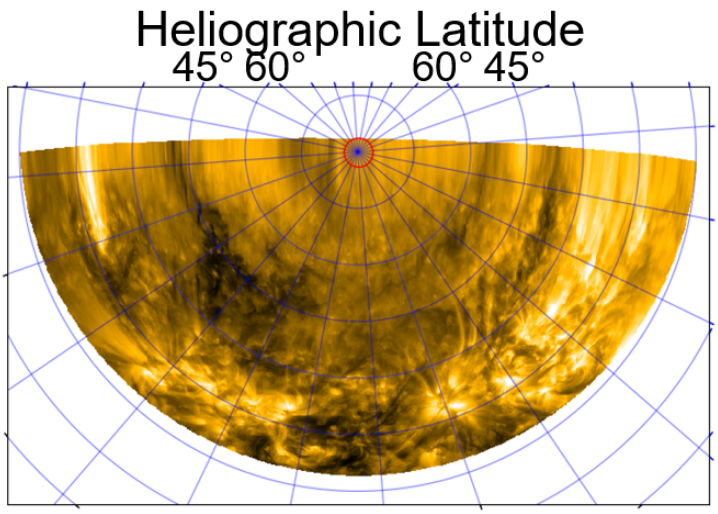

Figure 3.2: Visual representation of the latitude-dependent longitude coverage. Concentric circles represent a constant latitude. Near the pole, within the red circle, the longitude coverage reaches 360°. At lower latitude values, this longitude coverage significantly drops to nearly 180°.

This procedure results in a 2D array in which the rows correspond to time and the columns correspond to individual pixels located within the selected latitude band, as shown in Figure 3.1. However, the pixels within this band are not yet ordered by their heliographic longitude. In order to construct a physically meaningful LT representation, the selected pixels are sorted according to their associated longitude values. This ordering ensures that the horizontal axis of the resulting slice corresponds to the increasing heliographic longitude.

Due to the limited field of view of the observations and the masking applied during preprocessing, some longitude positions may contain missing values at certain time steps, as also seen in Figure 3.2. These missing values appear as *NaN* entries in the data. Columns that consist entirely of missing values across all time steps do not contain useful information and are therefore removed from the slice. This step ensures that the resulting longitude-time map includes only longitudes observed in the dataset.

The final product of this procedure is a 2D array in which the vertical axis represents time and the horizontal axis represents heliographic longitude along the chosen latitude band. Intensity variations within this map trace the motion of different solar structures over time. When visualized, such maps reveal characteristic diagonal lines corresponding to rotating and/or propagating solar features. The slopes of these lines can then be analyzed to infer the apparent rotation rates of structures within the polar regions.

These LT maps serve as the primary diagnostic tool in the study of the apparent rotation and motion of solar structures in the polar regions. By measuring the slopes of the observed lines, the corresponding rotation rates can be quantified (see Chapter 4).

3.6.4 Calculating Rotational Speeds

Once the LT maps are constructed, the apparent motion of solar structures can be identified as diagonal lines within these maps. The inverse slope ($d\Phi/dt$) of these lines represents the longitudinal displacement of a structure as a function of time, and therefore provides a direct measure of its apparent rotational motion. However, we note that for some of the coronal structures, the apparent rotational motion might be combined with the intrinsic motion of the studied structure. We expect that such a structure will provide statistically different rotational speeds.

To determine slopes in the LT maps, individual lines were visually identified. For each selected streak, two points were manually placed along the structure to mark its beginning and end. The coordinates of these points correspond to specific longitude-time pairs within the slice. Using these two coordinates, a straight line connecting the points was defined, and the slope was calculated as the ratio of the longitudinal displacement ($d\Phi$) to the elapsed time (dt), expressed in units of 30 or 60 minutes, depending on the dataset. In the course of visual identification, focus was on the well-defined lines with the clear, straight signatures in the LT maps.

The procedure was repeated for a large number of visible lines in the maps to obtain a representative sample of slope measurements. Because the slope was initially calculated from longitude and time coordinates, the resulting values were expressed in degrees per unit of time. The obtained slopes were subsequently converted to rotational speeds in units of degrees per day, allowing direct comparison with the expected differential rotation profile of the Sun as expressed in Equation (1.5).

It should be noted that this procedure involves manual selection of lines, which introduces some measurement uncertainty. To mitigate this effect, a sufficiently large number of lines was analyzed, enabling the derivation of statistically meaningful averages and uncertainties.

3.7 Saving Data Format

After determining the slopes for a large number of lines, the resulting measurements were stored for the statistical analysis. For each identified streak, the coordinates of the two selected points were recorded together with the corresponding slope value. Since the coordinates of the selected points are known within the longitude-time slice, the intensity values at these positions can also be retrieved from the data. Including the intensity measurements allows potential correlations between brightness and rotational behavior to be investigated during future analysis.

For each tracked streak, the stored dataset therefore consists of the coordinates of the two selected points, the calculated slope, and the corresponding intensity values at those locations. The structure of the stored data is summarized in Table 3.1. Separate text files were created for each analyzed latitude to facilitate subsequent data analysis and comparison across different polar regions.

Pair	X1	Y1	X2	Y2	Slope	Intensity1	Intensity2

Table 3.1: Structure of the stored measurements for a given time–longitude slice. The pair index identifies each tracked streak. (X_1, Y_1) and (X_2, Y_2), corresponding to (Θ_i, t_i) respectively, denote the coordinates of the two manually selected points used to compute the slope. Intensity$_1$ and Intensity$_2$ represent the corresponding pixel intensities at these locations.

3.8 Statistics and Regression Techniques

For each selected latitude band, all manually measured slopes obtained from the LT maps were converted into angular velocities. The resulting distributions were subsequently visualized using histograms. In order to try to characterize these distributions, Gaussian functions were fitted to the measured values, yielding estimates for the mean angular velocity and the associated standard deviation for each latitude band.

To assess whether the measured distributions could reasonably be approximated by Gaussian statistics, quantile-quantile (QQ) plots were constructed. These compare the quantiles of the measured distributions with those expected from an ideal normal distribution. Deviations from linear behavior in the QQ plots therefore indicate departures from Gaussian behavior, particularly in the tails of the distributions.

The latitude dependence of the obtained angular velocities was then compared with empirical solar differential rotation laws. Linear least-squares fitting was applied to determine the coefficients of both a three-coefficient differential rotation model of the form

$$\omega(\Phi) = A + B\sin^2(\Phi) + C\sin^4(\Phi), \tag{3.3}$$

and a simplified two-coefficient model given by

$$\omega(\Phi) = A + B\sin^2(\Phi). \tag{3.4}$$

These fitted profiles were subsequently compared with the results of several previous empirical differential rotation relations obtained from tracing coronal bright points (detailed references and functional dependence can be found in the work of Wöhl et al. 2010).

3.9 Implementation Consideration, Assumptions, and Limitations

In addition to the processing pipeline described above, several practical considerations, assumptions, and limitations must be addressed to properly interpret the results obtained in this study.

3.9.1 Data Handling and Storage

During the preprocessing and analysis stages, missing or invalid data values (NaNs) are sometimes obtained, primarily due to instrumental effects, reprojection boundaries, or incomplete coverage of the field of view. These values are handled carefully to avoid introducing artificial structures or biases in the analysis. In particular, NaNs are preserved throughout the processing pipeline and excluded from calculations where appropriate, ensuring that derived quantities such as slopes are not influenced by non-physical data points.

Alongside positional information, intensity values are retained throughout the analysis. This allows for the identification and tracking of coherent structures in longitude-time maps, as intensity variations provide an additional constraint when distinguishing physical features from noise or artifacts. Furthermore, storing intensity information enables potential extensions of the analysis, such as investigating correlations between brightness and dynamical behavior.

The full data processing and analysis pipeline is implemented in a dedicated code base, ensuring reproducibility of the results. Key steps, including preprocessing, reprojection, data cube construction, and slope extraction, are explicitly defined within this framework.

3.9.2 Assumptions and limitations

The analysis presented in this work relies on several assumptions:

- Coronal structures visible in EUV intensity maps are assumed to trace the underlying plasma motion and, consequently, the rotational behavior of the Sun.
- The reprojection procedure is assumed to sufficiently correct for projection effects, such that the derived spatial coordinates accurately represent the true heliographic positions.
- The manually selected lines in longitude-time maps are assumed to be representative of the overall population of structures, allowing for meaningful interpretation of their measured slopes.

We note that due to the adopted assumptions, like in any other data-based study, inherent uncertainties might appear, and that they need to be taken into consideration when interpreting the results.

Several limitations will affect the analysis and should be taken into account during the interpretation of the results:

- Manual bias: The identification and selection of lines in longitude-time maps are performed manually, which introduces subjectivity. Different selections may lead to variations in the derived slopes. However, these expected variations are small.
- Limited longitudinal coverage: The analysis is restricted to a finite longitude range, which may not fully capture the global rotational behavior.

- Reprojection artifacts: Although reprojection reduces projection effects, it can introduce interpolation errors and distortions, particularly near the edges of the transformed domain. In order to avoid these artifacts, only the observations well beyond the edge of the observations were employed.
- Temporal resolution constraints: The cadence of the observations limits the ability to resolve rapidly evolving structures, potentially leading to underestimation or misidentification of dynamic features.
- Feature bias: Features that are not on the surface of the coronal base but are sticking out of the surface will have a different apparent motion. As we will show in Chapters 4 and 5, this effect can be significant.

3.10 Research Objective and Approach

The complex interplay between energy transport in the solar interior, magnetic field generation through dynamo processes, and the cyclic evolution of the solar magnetic field ultimately governs the structure and dynamics of the solar corona. In particular, the solar activity cycle and the associated reversal of the global magnetic field have a profound impact on the polar regions, where large-scale open magnetic field structures and coronal holes dominate. These regions are key to understanding the origin of the fast solar wind and the global structure of the magnetic field of the Sun, which yet they remain not fully understood due to observational limitations.

With the advent of novel high-latitude observations from SolO, and in particular with the use of the EUI, it is now possible to study the polar corona with unprecedented spatial and temporal resolution. EUV observations provide direct insight into the dynamics of coronal plasma, allowing the tracking of structures shaped by the underlying magnetic field. By analyzing the temporal evolution of these structures through longitude-time representations, it becomes possible to quantify their apparent rotational behavior and investigate how it relates to the Sun's differential rotation and magnetic field configuration.

This work aims to investigate the dynamics of the solar polar corona by analyzing novel polar EUI observations and extracting rotational properties of coronal structures at high latitudes. In doing so, it aims to contribute to a better understanding of how large-scale magnetic fields evolve, particularly in the context of the solar cycle, and how it influences the behavior of the polar corona and its role in the heliosphere.

Chapter 4

Dynamics of the Coronal Structures Observed by EUI on Solar Orbiter

This chapter presents the results obtained in the study of coronal structures, which followed the construction of the data-processing pipeline and data selection as described in Chapter 3. The main objective of the analysis is to test the accuracy of the present estimate of the differential rotation rate employing novel SolO observations. In more detail, we aimed to quantify the apparent rotational behavior of coronal structures observed in the solar polar regions and to compare these measurements with the other differential rotation profiles of the Sun and its corona. To achieve this, the processed EUI observations are transformed into LT maps, from which the slopes of individual intensity lines are measured and converted into angular velocities.

This chapter is organized following the same logical sequence as the analysis procedure presented in Chapter 3. First, several intermediate processing steps are presented to illustrate the transformation from the original EUI observations to the final pole-centered data cubes used in this work. Next, representative LT maps are shown, both before and after manual identification of the tracked lines. The measured rotation rates are then analyzed statistically through histograms, Gaussian fits, and quantile-quantile (Q-Q) plots to asses whether the distributions can be approximated by normal distributions. Following the distributions, the derived angular velocities are compared with the theoretical differential rotation law introduced in Equation (1.5) and other empirical rotation laws based on different types of coronal structures and through different types of observations. Together, these results provide a quantitative description of the rotational dynamics of the solar polar corona and establish the observational basis for the interpretation presented in Chapter 4.

4.1 Verification of the Data Processing Pipeline

Before analyzing the rotational properties of coronal structures, it is necessary to verify that the preprocessing pipeline transforms the original EUI observations into a consistent representation of the solar polar regions. The top left panel in Figure 4.1 shows the original Level 2 EUI observation retrieved through the SunPy Fido interface. Because the Full Sun Imager (FSI) was used, the entire solar disk is visible within the field of view. Due to the spacecraft's distance from the Sun and the large detector size, the solar disk occupies only a relatively small fraction of the image, approximately one-ninth of the total frame. In addition, the image is slightly rotated counterclockwise with respect to the standard solar orientation.

To obtain a consistent representation of the observations, each image was first centered on the solar disk and corrected for the rotation angle derived from the metadata. A heliographic coordinate grid was then overlaid to identify the visible solar pole, which in the presented example corresponds to the South Pole, as presented in the top right panel of Figure 4.1. Using this information, the image was reprojected onto an azimuthal equidistant (ARC) projection centered on the visible pole, as shown in the bottom left panel. Finally, the reprojected image was masked to retain only the region within 50° of the pole, corresponding to heliographic latitudes between -90° and -40° in this example. This masking is shown in the bottom right panel of Figure 4.1.

4.2 Pipeline Performance Metrics

The analysis presented in this work is based on a set of EUI observations acquired during a period when Solar Orbiter was located at high southern heliographic latitudes (around -16.3°). The primary dataset used throughout this study consists of observations obtained in the 304 Å channel between 2025 March 21 at 00:00:20 and 2025 March 28 at 15:30:20. This time interval provides continuous coverage of the South Pole region during the time interval of more than seven days.

Table 4.1 summarizes the main characteristics of the dataset, including the observation interval, wavelength, number of processed FITS files, and temporal cadence. These parameters determine both the temporal coverage and the time resolution of the resulting data cubes and LT maps.

The original dataset retrieved through Fido had a cadence of 10 minutes, resulting in more than 1000 individual images. Downloading and processing such a large number of files would have substantially increased the computational costs and execution time of the analysis pipeline. To reduce the processing time while preserving sufficient temporal resolution to track the rotational motion of coronal structures, the dataset was downsampled to a cadence of 30 minutes. This yielded 368 final observations.

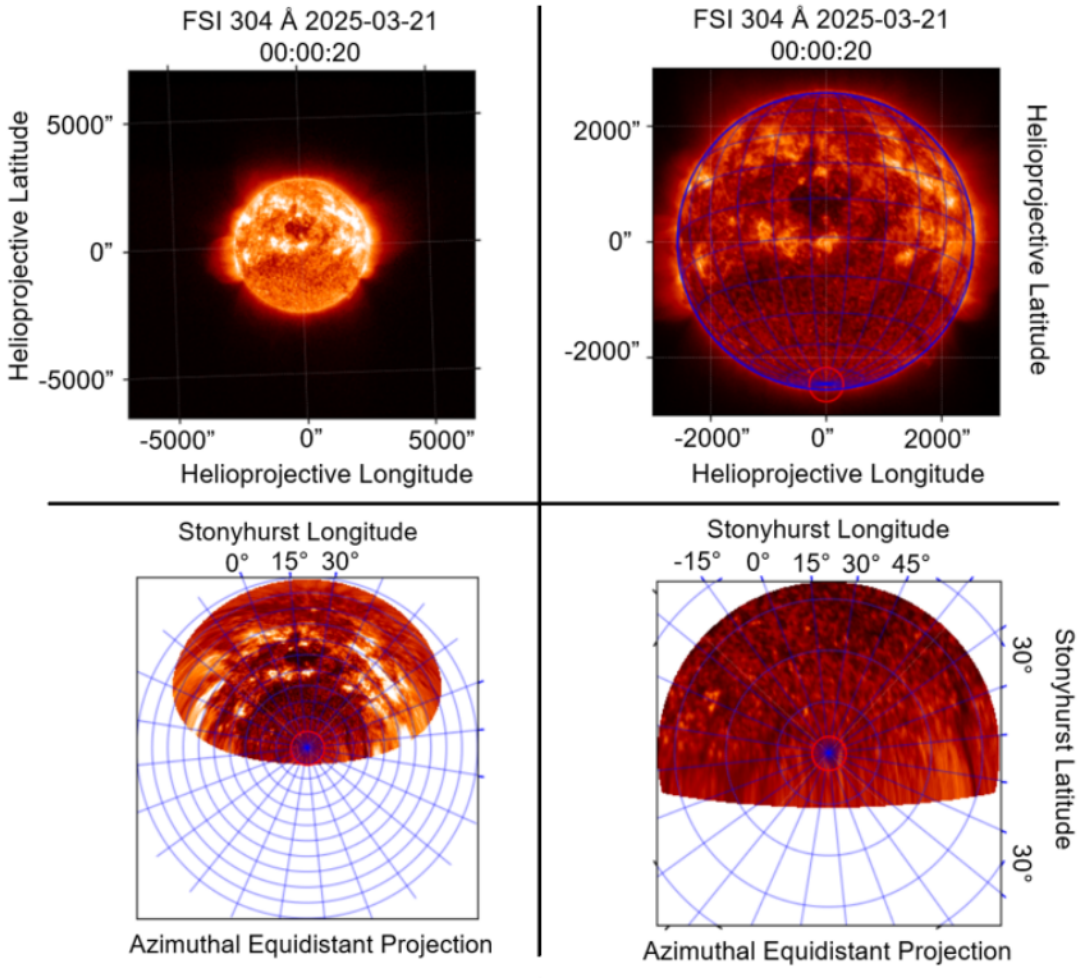

Figure 4.1: Combined figure of the entire preprocessing pipeline. Top left: The original EUI FSI image as obtained from Fido. Top right: The zoomed-in, derotated image with heliographic coordinate grid (blue) and South Pole marked in red. Bottom left: ARC projection of the entire image with the South Pole centrally placed. Bottom right: Cropped ARC projection with heliographic latitudes from -90 ° up to -40 °.

4.3 Construction of Data Cubes and Longitude-Time Maps

Following the preprocessing and reprojection steps, the observations were combined into three-dimensional data cubes, with two spatial dimensions and one temporal dimension (see Figure 3.1). These data cubes provide a time-dependent representation of the solar polar regions and form the basis for the analysis of coronal dynamics.

LT maps were constructed by extracting slices at fixed heliographic latitudes from the data cubes (see Chapter 3). To identify the pixels corresponding to a selected latitude, a tolerance of 0.1 ° was adopted. Using the target latitude and the tolerance criterion defined in Equation (3.2), all pixels within the specified latitude interval were selected and ordered according to their heliographic longitude.

Start Date	2025-03-21
End Date	2025-03-28
Number of Files	368
Wavelength	304 Å
Exposure time	10 s
Original Cadence	10 min
Down sampled Cadence	30 min
Visible Pole	South

Table 4.1: Summary of the main characteristics of the SolO/EUI dataset used in this work.

4.4 Manual Identification of Coronal Lines

To quantify the rate of the rotational behavior of coronal structures, individual lines visible in the LT maps were manually identified and measured. Figure 2.6 already showed an example of an LT map before the selection of these lines. Figures 4.2 and 4.3 now present the LT maps after the manual measurements were performed for all latitudes. The horizontal axis again corresponds to heliographic longitude, while the vertical axis represents time in units of 30 minutes. Persistent coronal structures appear as diagonal lines, whose slopes reflect their apparent rotational motion. Together with the rather straight lines in the LT maps, we also observe patchy and sometimes rather short-duration structures, which were not taken into consideration in the study. Namely, the aim was to select clear and well-defined straight lines that reflect the effect of the differential rotation on the individual and stable small-scale structures. Patchy and curved lines would present the combined effect of the differential rotation and the movements of the coronal structures intrinsic to themselves.

For example, for a heliographic latitude of -60°, as seen in the top panel of Figure 4.3, a total of 150 points were manually selected, corresponding to 75 individual lines. Each line was defined by two points, marking its beginning and end, from which the slope and the corresponding angular velocity were determined. For this specific latitude, the resulting mean angular velocity is 11.368 °/day.

The same procedure was repeated for all heliographic latitudes presented in Figures 4.2 and 4.3 to investigate the latitude dependence of the coronal rotation rate. Table 4.2 summarizes the number of measured lines and the corresponding mean angular velocity at each latitude. We note that, as we increase in the latitude, the number of selected lines decreases due to the smaller number of clearly observed drifting lines. Namely, the patchy and short duration pattern of bright structures becomes more and more prominent, in particular at -70° and -75°, influencing the number of well-defined lines available for the selection. We note that this effect also possibly partially reflects in the increased standard deviation for the higher latitudes (see Table 4.2)

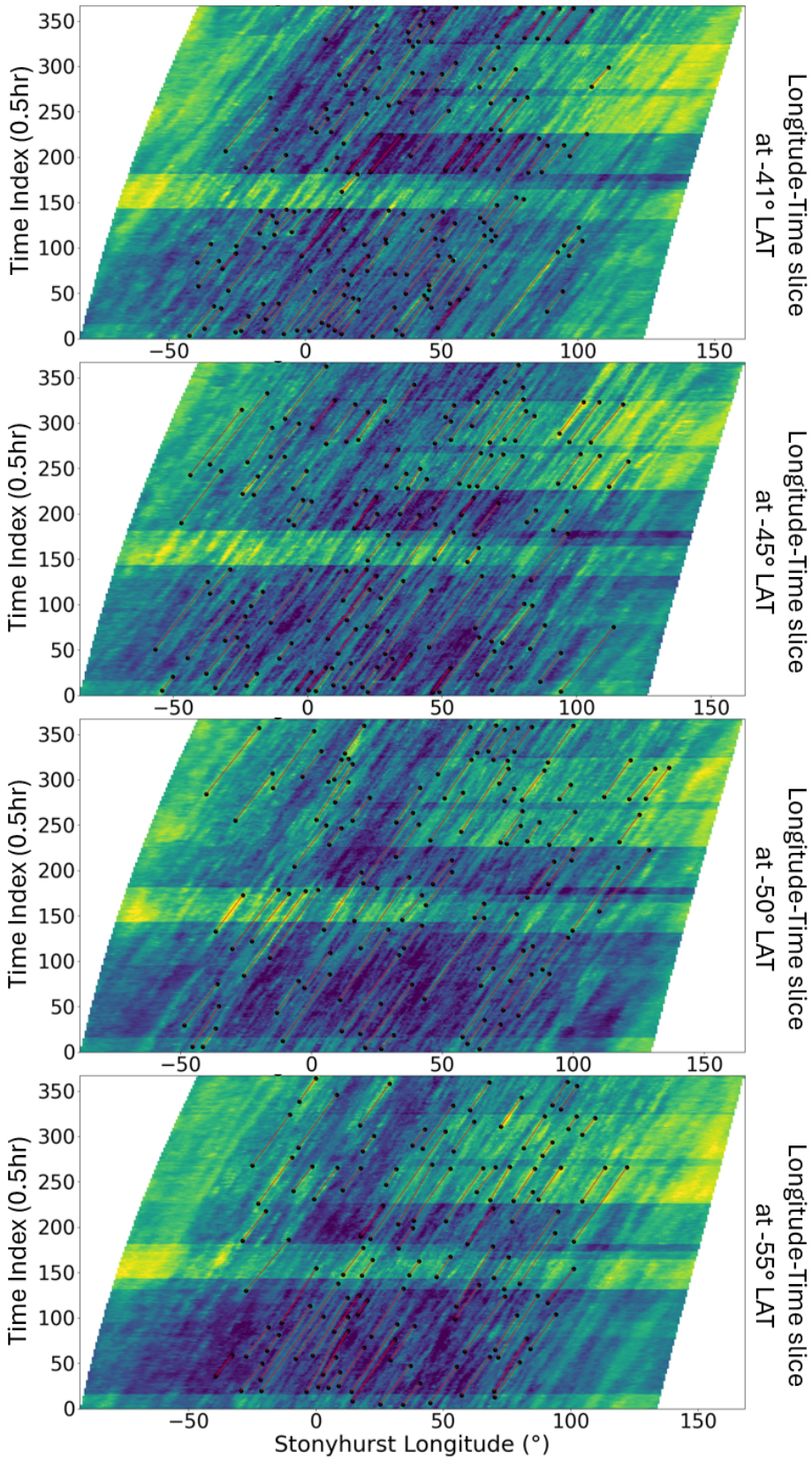

Figure 4.2: Longitude-time maps extracted at heliographic latitudes from -41° (top) up to -55° (bottom). The horizontal axis represents heliographic longitude, while the vertical axis shows time in units of 30 minutes. Diagonal bright lines correspond to the temporal evolution of coronal structures.

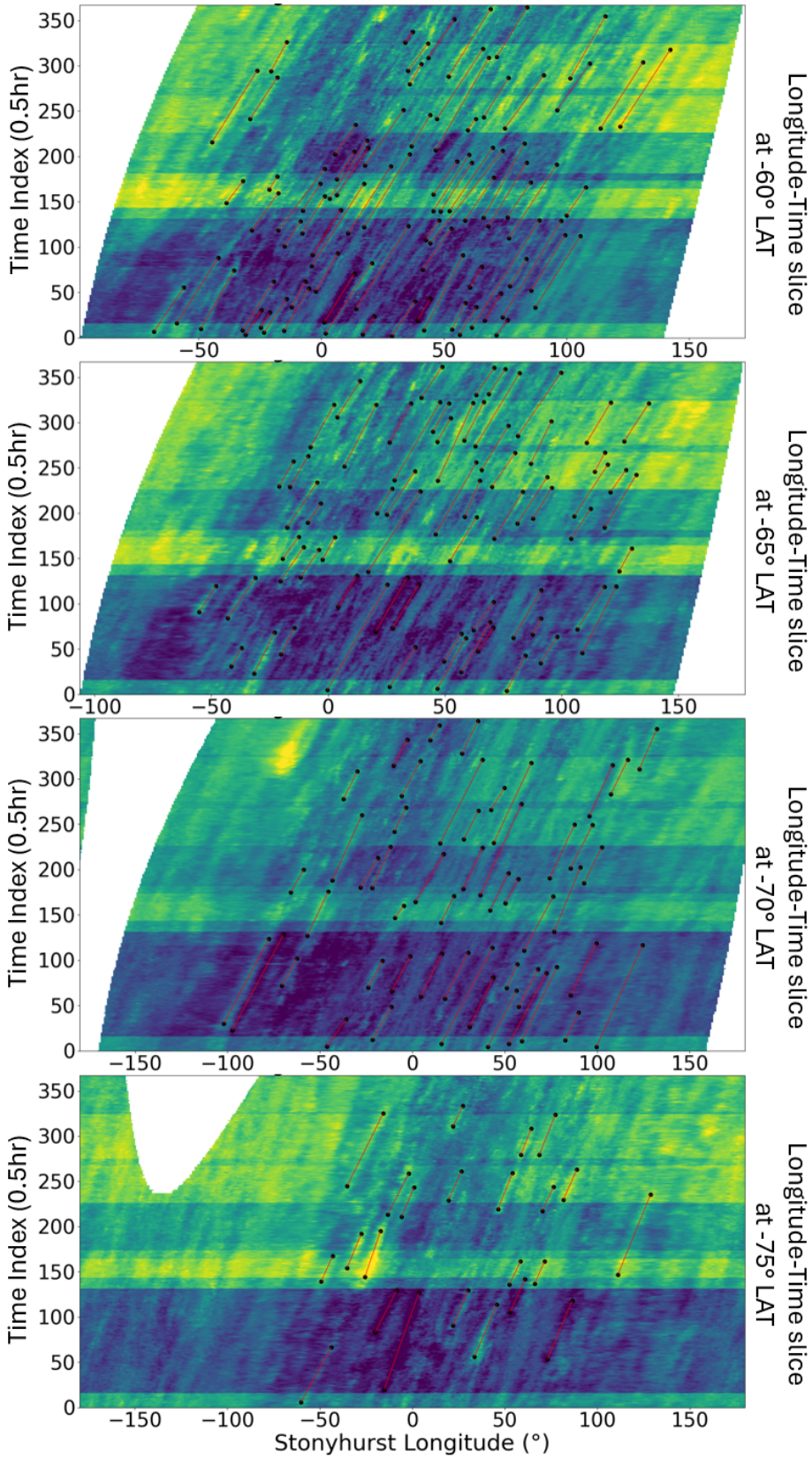

Figure 4.3: Longitude-time maps extracted at heliographic latitudes from -60° (top) and up to -75° (bottom). The horizontal axis represents heliographic longitude, while the vertical axis shows time in units of 30 minutes. Similar to Figure 4.3, diagonal lines correspond to the temporal evolution of coronal structures.

Latitude (°)	# Lines	Mean Angular Velocity (°/day)	Standard Deviation (°/day)
-41	93	12.518	0.877
-45	89	12.352	0.787
-50	74	12.189	0.998
-55	77	12.025	0.961
-60	75	11.368	0.992
-65	63	11.221	1.206
-70	49	12.135	1.477
-75	23	10.370	1.156

Table 4.2: Summary of the number of selected lines, mean angular velocity, and standard deviation for given latitude value.

The outer boundary of the analyzed polar region is located at -40° latitude. Because this latitude lies directly at the edge of the selected domain, the corresponding measurements are more sensitive to edge artifacts and incomplete data. To avoid these issues, the first analyzed latitude was chosen to be -41°, which provides a more representative sampling of the coronal structures within the selected region.

It can be seen from Figures 4.2 and 4.3 that the slopes of the manually selected lines gradually increase near higher latitude values. This indicates that different latitudes will have different angular velocities.

4.5 Statistical Distributions of Angular Velocities

The angular velocities, herein named also rotational velocities, derived from the manually identified lines were analyzed statistically to characterize their distribution at selected heliographic latitudes. For every latitude, a histogram was constructed using all measured angular velocities. A Gaussian function was then fitted to each histogram to estimate the mean rotation rate and the corresponding standard deviation. These quantities provide a compact description of the central tendency and spread of the measurements and form the basis for the subsequent comparison with theoretical differential rotation profiles.

The resulting histograms and Gaussian fits are shown in Figure 4.4. For almost all analyzed latitudes, the distributions exhibit a single, rather dominant peak, indicating that the measured angular velocities cluster around a characteristic value. Additionally, the majority of the distributions are approximately symmetric about their peak. In general, the Gaussian fits reproduce the location of the histogram maxima well. In most histograms, the peak of the fitted distribution coincides with the region containing the largest concentration of measurements. The agreement is particularly noticeable for the latitude ranges between -50° and -65°, where the histograms display a relatively smooth and continuous shape around their central values.

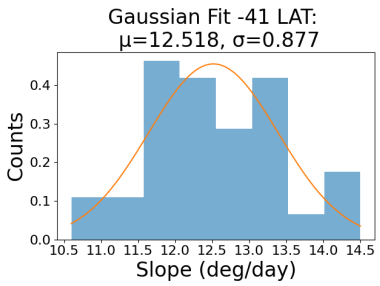

(a) Distribution for -41° latitude

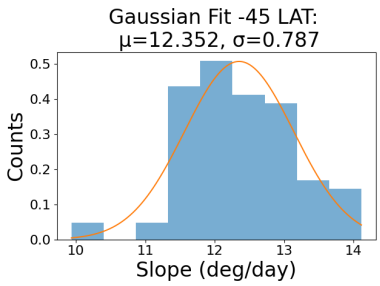

(b) Distribution for -45° latitude

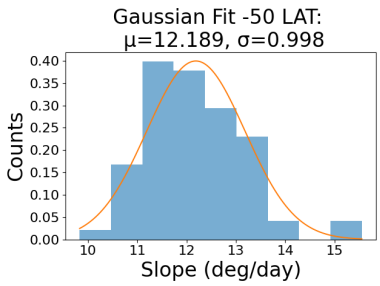

(c) Distribution for -50° latitude

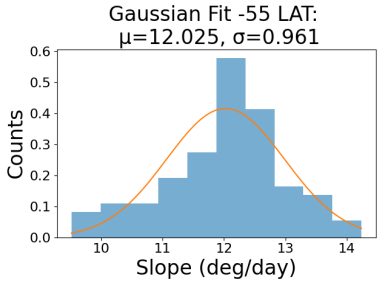

(d) Distribution for -55° latitude

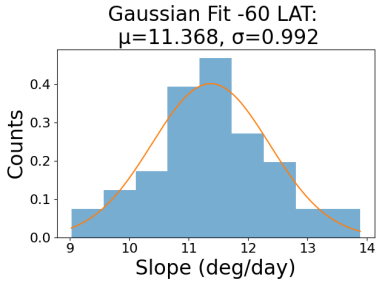

(e) Distribution for -60° latitude

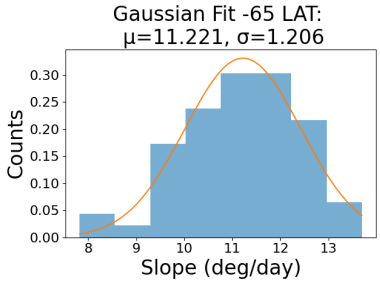

(f) Distribution for -65° latitude

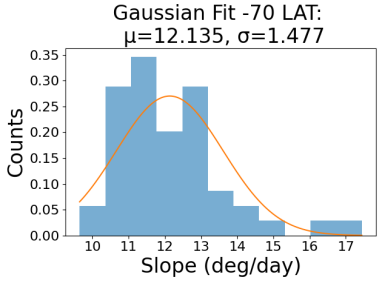

(g) Distribution for -70° latitude

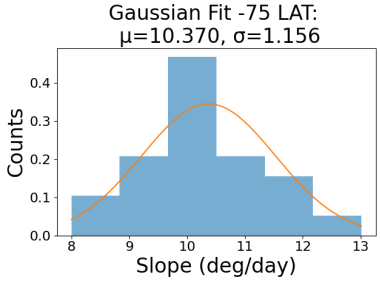

(h) Distribution for -75° latitude

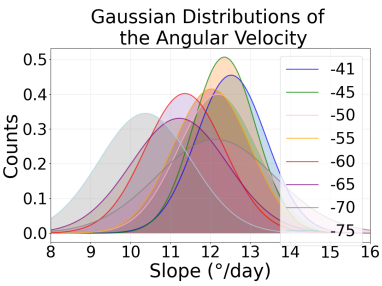

(i) Combined Gaussian distributions.

Figure 4.4: Combined figure of the distributions of the measured angular velocities for all latitude values ranging from -41° to -75°. A Gaussian overlay is fitted onto the data. The bottom rightmost panel combines all the Gaussians into one plot to examine the difference between the locations and widths of the distributions.

The centers of the distributions are located between approximately 10.4 and 12.5 °/day. The broadest distribution is observed at a latitude of -70°, where the fitted standard deviation is 1.477 °/day. The narrowest distribution occurs at a latitude of -45°, with a fitted standard deviation of 0.787 °/day. In the cases of latitude values of -45°, -55°, and -65°, the curves exhibit slight asymmetries towards the left, as they obtain a few small angular velocities with respect to the mean value. Here, values up to 8 °/day are observed, while the mean angular velocities are around 11 and 12 °/day. In contrast, latitude values of -50° and especially -70° show asymmetries toward the right, with rotational values reaching up to 17 °/day, heavily exceeding the mean angular velocity values. All these values causing the asymmetries are observed in the far tails of the Gaussian distributions.

The bottom rightmost panel in Figure 4.4 shows all Gaussians combined in one plot. Although this combined representation is visually dense, it still shows the trend of higher latitudes shifting progressively towards a lower slope value, and as such, a lower rotational speed. The overlap between neighboring latitude distributions is clearly visible. The distributions centered at lower latitudes show peaks that lie close together, resulting in substantial overlap. At higher latitudes, the distribution centers become increasingly separated from those of lower latitude bins. Consequently, the overlap between the highest latitude distributions and the lowest latitude distributions becomes noticeably smaller. We also note that, as we go towards the larger latitudes, the distributions start to be broader and have more pronounced tails.

Although the Gaussian means, in general, decrease with latitude, the standard deviations do not follow this similar trend. Instead, they generally increase with increasing latitude, going from 0.877 °/day up to almost 1.5 °/day. This behavior is also reflected visually in the varying widths of the fitted Gaussian curves.

4.6 Assessment of Normal Data Distribution

To evaluate whether the measured angular velocities are adequately described by Gaussian distributions, multiple quantile-quantile (Q-Q) plots were constructed (Wikipedia 2026b). These plots compare the observed quantiles with those expected for a normal distribution. Deviations from a straight line indicate departures from a normal distribution and may reveal the presence of outliers, skewness, or multiple populations. The resulting Q-Q plots are shown in Figure 4.5. In all cases, the majority of the data points lie close to the reference line over the central portion of the distributions, indicating that the ordered angular velocities closely follow the theoretical quantiles expected for a normal distribution. This near-linear behavior is most clearly visible for the latitude bands at -41°, -45°, -55°, and especially -60°, where the points remain tightly clustered around the line over nearly the entire quantile range.

For most latitude measurements, the central 50% of the ordered values are distributed almost symmetrically around the reference line. This can be seen from the absence of systematic curvature in the middle portion of the Q-Q plots. Here, the points closely trace the linear trend expected for a Gaussian distribution. At several latitudes, small deviations from the reference line are present near the lower and upper quantiles. These deviations are most pronounced at -50°, -65°, and especially -70°. In the case of -50°, the upper tail contains several points that are clearly separated from the main linear trend. Similar behavior is visible at -70° latitude, but with a larger amplitude. The lower quantiles generally show weaker deviations than the upper quantiles. Where departures are present, they are confined only to a small number of points. As visible also from the Figure 4.4, the distributions at both -50°, -70° latitudes show the existence of a number of events with a larger slope than approximately 15 °/day and between (15 – 17.5) °/day, respectively. We discuss these results in more detail in Chapter 5.

The Q-Q plot corresponding to -75° contains significantly fewer points than the other points, reflecting the smaller number of available measurements at this latitude, as also shown in Table 4.2. As a result, the plotted quantiles appear more sparsely distributed, although the points still closely follow an approximately linear trend.

The overall shape of the Q-Q plots is consistent with the characteristics already visible in the histogram distributions. Latitude bands exhibiting broader distributions and more pronounced tails in Figure 4.4 also display the largest departures from the theoretical normal quantiles. In contrast, the latitude bands with narrower and more symmetric histograms tend to produce Q-Q plots that remain closer to the reference line over the full quantile range.

Overall, the Q-Q plots show that the measured angular velocities exhibit an approximately linear relationship with the theoretical normal quantiles, with the largest departure occurring primarily in the outer quantiles. Additionally, there are no systematic deviations across all latitude bands, and when there are deviations present, they are localized to a specific latitude.

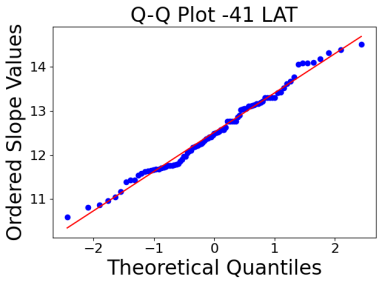

(a) Q-Q plot for -41° latitude

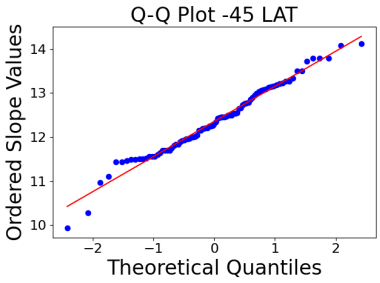

(b) Q-Q plot for -45° latitude

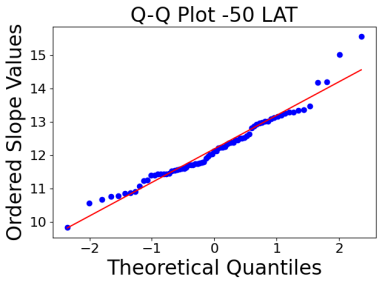

(c) Q-Q plot for -50° latitude

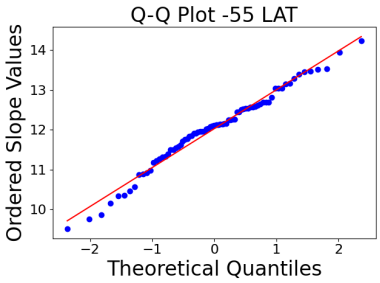

(d) Q-Q plot for -55° latitude

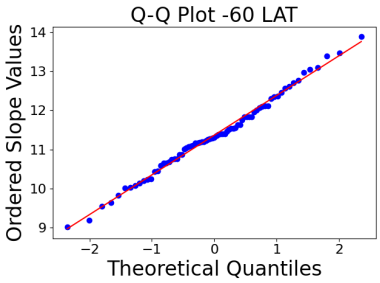

(e) Q-Q plot for -60° latitude

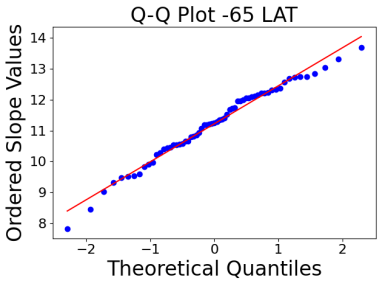

(f) Q-Q plot for -65° latitude

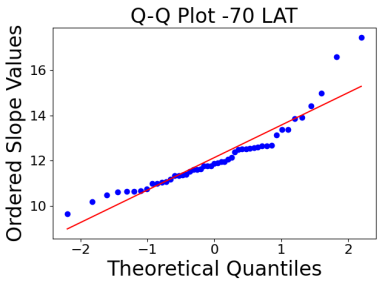

(g) Q-Q plot for -70° latitude

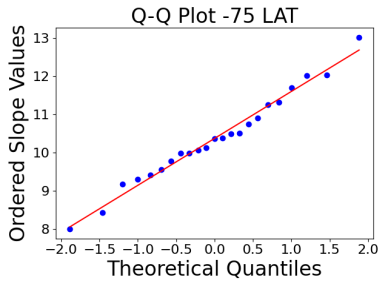

(h) Q-Q plot for -75° latitude

Figure 4.5: Combined figure of the Q-Q plots for all latitude values ranging from -41° to -75°. Q-Q plots are used to assess wether distributions of the angular velocity are normal distributed. Data closely following the reference line is assumed to be normal distributed.

4.7 Latitude Dependence of the Rotation Rate

The mean angular velocities obtained from the Gaussian fits were modeled with a regression technique using two differential rotation profiles. A first model included the full three-parameter form of the differential rotation relation, containing the coefficients A, B, and C, as given by Equation (3.3), while a second simplified model only included the coefficients A and B, as presented by Equation (3.4). Linear least-squares regression was then applied to determine the best-fitting coefficients in both cases.

The three-parameter model did not produce physically meaningful results for the present dataset. In particular, the fitting procedure forced the B-term contribution to negligible values, causing the resulting profile to flatten at lower heliographic latitudes. As a consequence, the simplified two-parameter model was adopted for the final analysis and is presented in Figure 4.6.

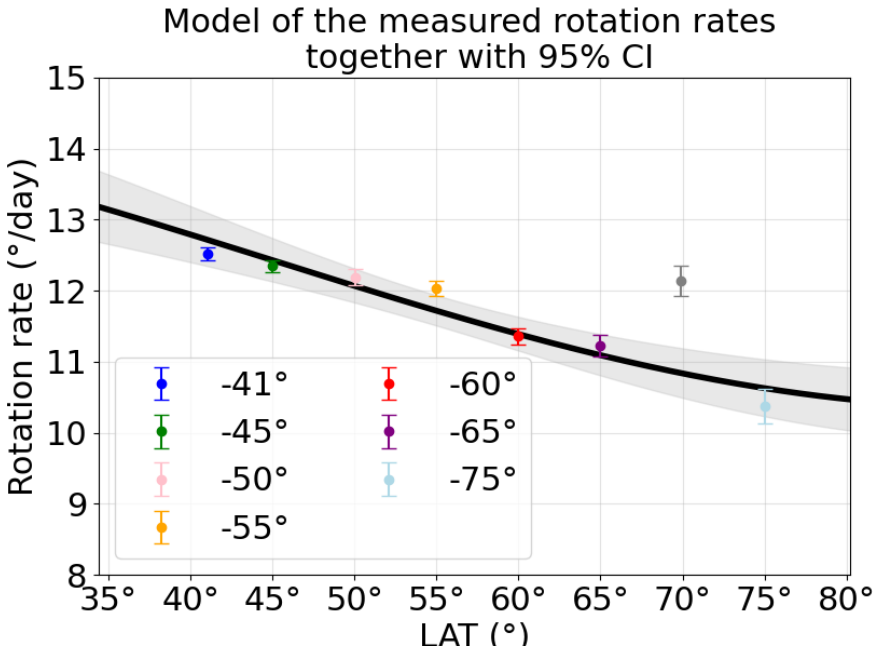

Figure 4.6: Least-squares regression model of the measured angular velocities. The black curve shows the resulting model: $\omega(\Phi) = 14.51 - 4.16\sin^2(\Phi)$. A 95% confidence interval (CI) is given in gray. The -70° measurement (grey) was taken out of consideration as it shows a significant difference. Detailed explanation for this exclusion is provided in Chapter 5.

For both fitting procedures, the measurement at -70° latitude was excluded from the regression analysis, as it was identified to be a significant outlier relative to the remaining measurements. Although this point was excluded from the fit, it is retained in the figures and the residual analysis to illustrate the magnitude of the deviation. The explanation and the possible reasons for the obtained results and for the exclusion of the -70° latitude measurements from the fitting analysis are discussed in Chapter 5. The resulting two-parameter fit reproduces the observed latitude dependence of the measured angular velocities rather well, with the fitted curve closely following the measurements across the sampled latitude range.

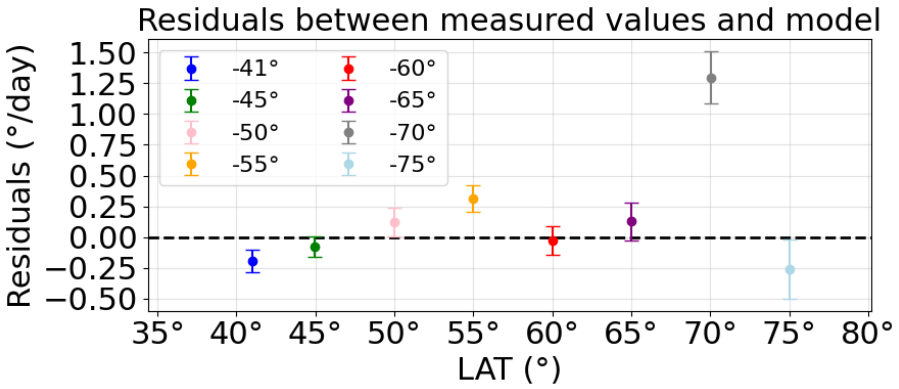

Figure 4.7: Residual plot showing the difference between the observed and modeled angular velocities. A residual of zero means a perfect fit.

Coefficient A	14.51 ± 0.35 °/day
Coefficient B	-4.16 ± 0.50 °/day

Latitude (°)	ω_{measured} (°/day)	ω_{model} (°/day)	σ_ω (°/day)	Residual (°/day)
-41	12.52	12.72	0.09	-0.20
-45	12.35	12.43	0.08	-0.08
-50	12.19	12.07	0.12	0.12
-55	12.03	11.72	0.11	0.31
-60	11.36	11.39	0.12	-0.03
-65	11.22	11.09	0.15	0.13
-70	12.13	10.83	0.21	1.30
-75	10.37	10.63	0.24	-0.26

Table 4.3: Measured angular velocities (ω_{measured}) together with the fitted two-parameter differential rotation model (ω_{model}), corresponding standard deviations (σ_ω), and residuals. The fitted model coefficients A and B are shown at the top of the table.

The uncertainties on the data points shown in Figure 4.6 correspond to the standard error on the mean, expressed as $\sigma/\sqrt{N}$ where σ represents the standard deviation of the measured angular velocity distribution and N is the number of manually identified lines within a given latitude band. The uncertainties increase toward higher latitudes, as previously shown in Table 4.2 and Figure 4.4

The obtained two-parameter differential rotation profile is characterized by the coefficients $A = 14.51 \pm 0.347\,°/\text{day}$ and $B = -4.16 \pm 0.502\,°/\text{day}$, where the quoted uncertainties represent the standard errors obtained from the regression analysis. The overall quality of the fit is reflected by a coefficient of determination of $R^2 > 0.93$. To further assess the reliability of the fitted coefficients, a 95% confidence interval (CI) was calculated for the regression model and is shown as a gray shaded area around the fitted curve in Figure 4.6. Within this interval, the coefficient A varies between 13.62 and 15.40 °/day, while the coefficient B varies between -5.45 and -2.87 °/day.

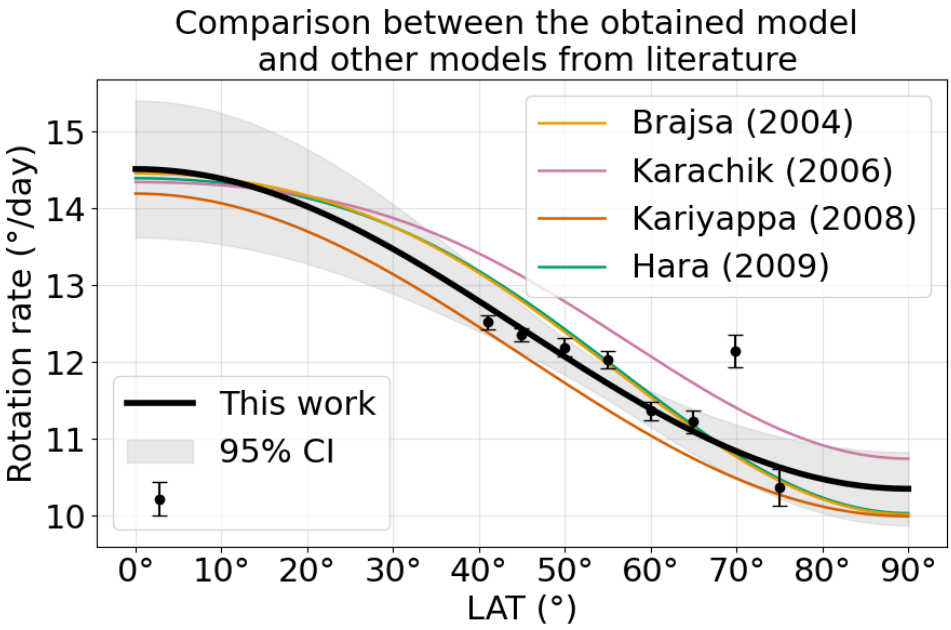

Figure 4.8: Comparison between the differential rotation model computed here (black curve) and previous models using coronal bright points as tracers (colored curves). The information about results from different studies was obtained from Wöhl et al. 2010. The black points represent the measured angular velocities. A 95% confidence interval (CI) is given in gray. The uncertainty is larger at latitudes below 40° as it relies on the fit and not on the data points.

Further, the quality of the regression was evaluated through the residuals shown in Figure 4.7. We present the difference between the obtained differential rotation model and the measured angular velocities. Most measurements deviate by less than approximately 0.31 °/day from the fitted profile, supporting the overall consistency of the model. The largest residual is again associated with the -70° latitude measurement, which differs from the fitted profile by approximately 1.30 °/day. A numerical summary of the measured angular velocities and the predicted angular velocities by the model is given in Table 4.3. This table gives the numerical values that are visually presented in Figures 4.6 and 4.7.

In order to put the results obtained in this study in a broader context, the herein obtained differential rotation profile was compared with several previously published coronal rotation models using coronal bright points (for more details see Wöhl et al. 2010, and references therein). Figure 4.8 shows a comparison of the results obtained in this study, together with a 95% CI represented with the shaded area, and results obtained employing coronal bright points (summarized also in the Table 16 of Wöhl et al. 2010). We note that the compared differential rotation profiles exhibit overall a similar behavior. The curves remain relatively close together at low latitudes and gradually diverge toward higher latitudes.

Among the considered models, the profile of Karachik et al. 2006 predicts the highest rotation rates at intermediate and high latitudes, while the profile of Kariyappa 2008 predicts the lowest values over the same latitude range. The model obtained

Time	$A \pm M_A$	$B \pm M_B$	$C \pm M_C$	Source
1992-2001	17.6 ± 0.4	-4.5 ± 1.1		Kariyappa 2008
1994-1997	14.39 ± 0.01	-1.91 ± 0.10	-2.45 ± 0.17	Hara 2009
1996	14.34 ± 0.03	-1.3 ± 0.3	-2.3 ± 0.5	Karachik et al. 2006
1998-1911	14.454 ± 0.027	-2.22 ± 0.07	-2.22 ± 0.07	Brajša et al. 2004
2005	16.0 ± 0.1	-0.7 ± 1.3	-4.9 ± 1.9	Karachik et al. 2006
2007	14.19 ± 0.17	-4.2 ± 0.8		Kariyappa 2008
2025-2026	14.51 ± 0.35	-4.16 ± 0.50		This work

Table 4.4: Extension to a comparison between differential rotation parameters A, B, and C, together with their respective mean errors M_i (Wöhl et al. 2010).

in this work remains located between these two profiles for most of the latitudes. The numerical comparison in Table 4.4 further illustrates the similarity between the differential rotation coefficients derived in this work and those reported previously. The fitted A-coefficient obtained here, $A = 14.51 \pm 0.35\,^\circ$/day, is very close to the value reported by Brajša et al. 2004, Hara 2009, and the 1996 observations of Karachik et al. 2006, all of which lie between approximately 14.3 and 14.5 °/day. The coefficient $B = -4.16 \pm 0.50\,^\circ$/day is among the more negative values listed in Table 4.4. It is nevertheless comparable to the values reported by Kariyappa 2008, particularly for the 2007 observations, which yielded $B = -4.2 \pm 0.8\,^\circ$/day.

In order to make a more detailed comparison, we aim to consider not only functional dependence but also the average values obtained at individual latitudes. Therefore, we make a direct comparison of our results and the EIT results from the study by Wöhl et al. 2010 (Figure 4.9). The top panel of Figure 4.9 shows Figure 2 from Wöhl et al. 2010. The bottom panel shows our results, in the same range of rotational velocity as in the top panel, i.e. 11 to 15 °/day. We note that the last two points of our study, at 70 ° and 75 °, are excluded from this presentation. As can be seen in Figure 4.8, our results for the 70 ° showed a significant discrepancy and can be considered as the outlier, while the results at 75 °, even if they show a bit larger error bars, do not significantly deviate from the ones at lower latitude. Together with the results of our study, the bottom panel in Figure 4.9 also reconstructs different least squares fits to all filtered data from the study by Wöhl et al. 2010. This detailed comparison clearly shows that our results systematically differ from those by Wöhl et al. 2010. Even if the range of rotational velocities is similar, the absolute values obtained in our study are decreasing noticeably faster, and they show a systematic shift of around 0.5 °/day in comparison with the results by Wöhl et al. 2010. Additionally, the error bars of the data points obtained in this study are significantly smaller than those obtained by Wöhl et al. 2010. One of the reasons for such a result is possibly the lower resolution of the observations employed in the study by Wöhl et al. 2010, where the authors used small bright coronal structures observed in the SOHO-EIT images. Another reason for such a result is probably projection effects, which clearly make a larger impact in the study by Wöhl et al. 2010. In order to further affirm our results, additional measurements can be done at several more latitudes. However, we do not expect a change in our conclusions.

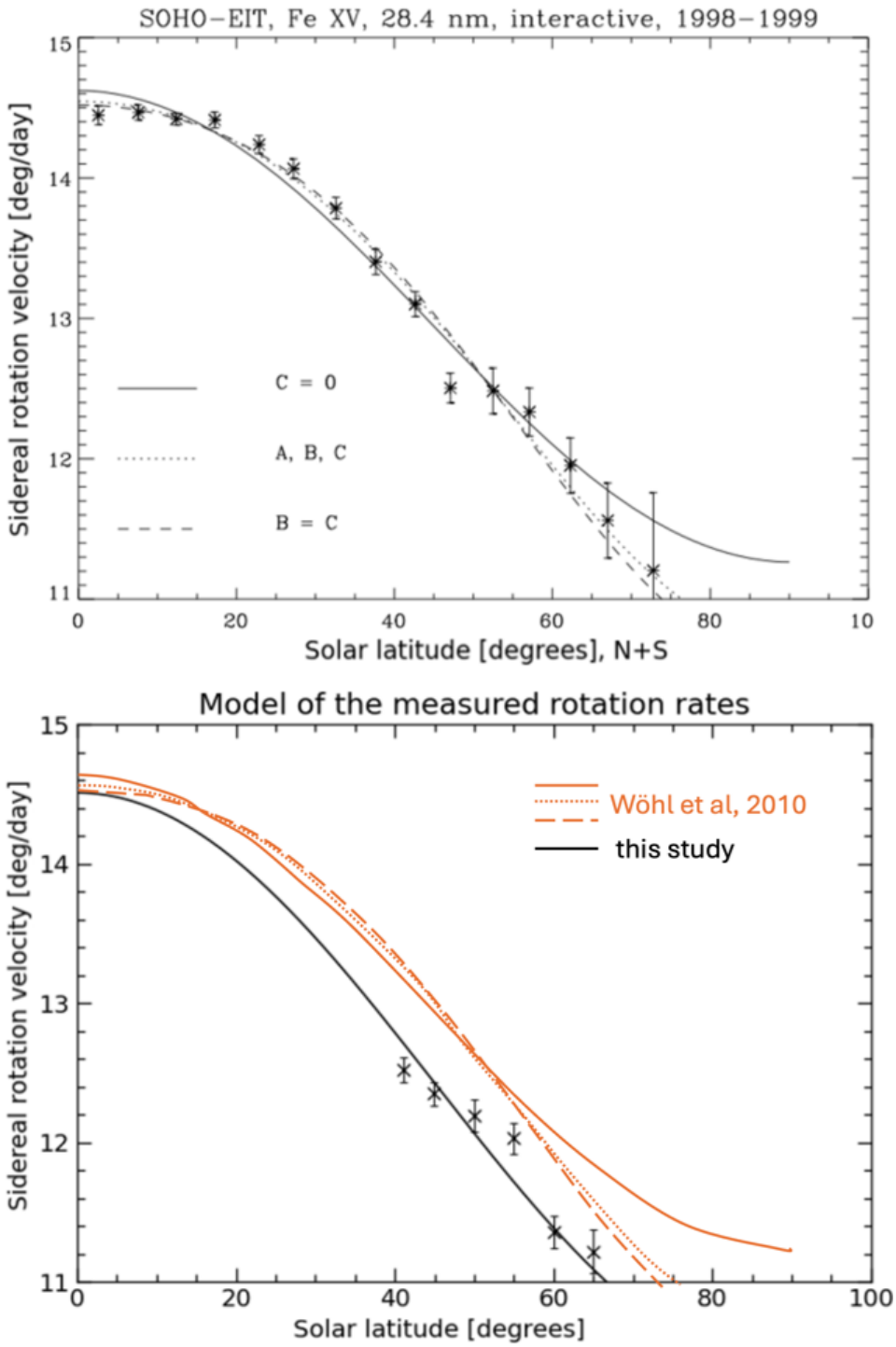

Figure 4.9: Top: Results obtained by Wöhl et al. 2010 using coronal bright points as tracers. Different models, based on the three parameters A, B, and C, are presented. Bottom: Direct comparison between the results obtained by Wöhl et al. 2010 (orange) and the fit obtained in this work (black). The black points on the right figure represent the data points obtained in this work.

Chapter 5

Results and Discussion

5.1 Compute Time Constraints

The construction of the data cube of reprojected images took on the order of half an hour to an hour for each slice. This excessive amount of time arose due to the fact that we did the WCS transformation from pixel indices to physical coordinates for each and every frame. It needs to be noted that all computations were performed on a personal desktop computer equipped with an AMD Ryzen 9 5900X 12-core processor and 32 GB of RAM, rather than on a dedicated high-performance computing (HPC) cluster. As mentioned, a tolerance of 0.1 ° was used to extract the desired latitude bands. When increasing this tolerance, the time necessary to construct the cube remained the same, but the construction of the longitude-time slices, the so-called LT maps, took longer, as more data needed to be loaded in. Additionally, marking points on the LT map later on took longer to load as multiple “layers” of images were stacked on top of each other by using a larger tolerance.

5.2 Measurement Accuracy of the Angular Velocities

As the construction of the LT maps was computationally and manually intensive, only nine latitude bands were selected, as presented in Table 4.2. The first results showed that the derived rotational, i.e., angular velocity, appeared to agree with the expected trend of decreasing angular velocity towards the higher heliographic latitudes. However, due to the smaller angular range of the coronal structures in the LT maps, the number of measurements decreased with the increase of the heliographic latitudes. That also resulted in the visible increase of the standard deviation (see Table 4.2).

The distributions of the measured angular velocity, shown in Figure 4.4, exhibit an approximately Gaussian-like behavior. The shape of the distributions is influenced by several factors. First, the identification and tracing of persistent coronal structures within the LT maps were performed manually. The “human-factor” introduces some level of uncertainty in the determination of the slopes. This effect becomes particularly important in regions where coronal structures appear diffuse, fragmented, or evolve, making the precise placement of the tracing lines subjective to some extent. This

effect was clearly visible at the larger latitudes. In addition, due to proper motions, not all coronal features are expected to rotate at the identical angular velocity even at fixed latitude, which leads to small deviations from the empirical differential rotation profile given by Equation (1.5). The combined influence of observational uncertainties and intrinsic coronal variability, therefore, naturally produces a distribution of measured rotation rates centered around the expected theoretical value.

The increase in the standard deviation of the Gaussian-like distributions toward higher latitudes, as presented in Table 4.2 and Figure 4.4 is easily understandable. At higher latitudes, fewer persistent coronal structures could be reliably identified and tracked within the LT maps, reducing the statistical robustness of the measurements. In addition, the reduced EUV contrast and the increasing presence of diffuse polar structures complicated the manual identification of coherent features. Consequently, the spread in the measured angular velocity increased with latitude, resulting in narrower distributions at lower latitudes and broader distributions closer to the poles.

The choice of histogram bin size also somewhat influences the apparent shape of the angular velocity distributions. Here, the bin size was determined automatically by Python's "auto" function to avoid introducing a subjective bias in the visualization of the data. The distributions with the different bins were also inspected, but not presented. Choosing substantially smaller bins increases the statistical noise and produces irregular fluctuations dominated by the limited sample size, particularly at high latitudes where fewer measurements were available. On the other hand, selecting significantly larger bins would over-smooth the distributions and potentially conceal deviations from Gaussian behavior visible in the outer quantiles of the distributions. The adopted automatic binning, therefore, provides a compromise between statistical stability and preserving the underlying structure of the measured rotation-rate distributions.

When assessing whether the distributions were indeed Gaussian, Q-Q plots were generated for each set of measurements, as presented in Figure 4.5. For a perfect Gaussian distribution, all measurements would lie on the reference red line. When a distribution differs from a perfect Gaussian distribution, this affects the location of the points on the Q-Q plot. In general, the Q-Q analysis showed that the angular velocity distributions were consistent with an approximation of a Gaussian distribution, particularly within their central regions. This suggests that the dominant variations in the angular velocity measurements are likely governed by a combination of multiple effects, for which Gaussian statistics provide a reasonable first-order approximation.

However, the observed deviations from this trend, especially in the outer quantiles, indicate that the distributions are not perfectly Gaussian in all quantiles. In particular, the enhanced deviations in the upper tails at a few latitude bands suggest the occasional presence of unusually large angular velocity measurements. These points may reflect additional dynamical processes appearing together with the differential rotation for some of the considered structures, and/or measurement uncertainties due to manual bias.

On the other hand, the absence of a uniform deviation pattern across all latitudes is also important. If the departures from a normal distribution would arise purely from instrumental or methodological effects, a more systematic behavior might be expected across all datasets. Instead, the non-systematically varying distributions' tail behavior, particularly visible for latitudes of -50°, -75°, and -70°, suggests that the statistical properties of the angular velocities may also depend on a case-by-case basis. The statistical significance of the points which deviate from the Gaussian distribution is not large, indicating that this deviation is indeed due to the selection of coronal structures which have non-negligible proper motion, as it will be further discussed in Section 5.3.

Despite the small tail deviations in the distributions, the approximately linear behavior over the majority of the quantile range indicates that the use of Gaussian-based statistics, such as means and standard deviations, remains broadly justified for describing the bulk properties of the distributions. Nevertheless, the non-Gaussian behavior in the tails implies that extreme values may contribute disproportionately to the variance at some latitudes and should therefore be interpreted with caution. Namely, this indicates that the error bars obtained in the study, in particular for some of the latitudes, could be even smaller than they are presently.

The strongest deviations occur at latitudes where the number of measurements is either limited or where several isolated high-valued points are present, as for example in the -75° and -70° distributions respectively. In the case of these highest-latitude bands, the reduced sample size may amplify the visual impact of individual measurements in the Q-Q plots, making departures from linearity appear more pronounced. Consequently, some of the observed deviations may arise from limited statistical sampling rather than reflecting an intrinsic non-Gaussian-like structure. Overall, the Q-Q analysis supports the conclusion that the angular velocity distributions are approximately Gaussian, and that somewhat latitude-dependent differences in the distributions' tails may contain physically relevant information.

5.3 Differential Rotation

Although the obtained two-parameter differential rotation profile reproduces the measured angular velocities well, several aspects need to be discussed. First, the three-parameter model did not produce physically meaningful results for the present dataset. In particular, the fitting procedure drove the contribution of the B-term toward negligible values, causing the fitted profile to flatten at lower heliographic latitudes. This behavior is most likely related to the limited number of sampled latitude bands. Since there are only mid to high latitude bands measured, the $sin^4(\Phi)$ term will dominate, causing a decrease in the B-value before the $\sin^2(\Phi)$ term. To produce a full three-parameter model, it would be necessary to include observations across the entire latitude spectrum. As a consequence, the simplified two-parameter model is a more appropriate one for the present analysis.

As discussed in Chapter 4, the large deviation from the expected differential rotation rate, shown also in Figures 4.6 and 4.7, was observed at the -70° latitude band. Inspection of simultaneous AIA 193 Å observations revealed the presence of a large

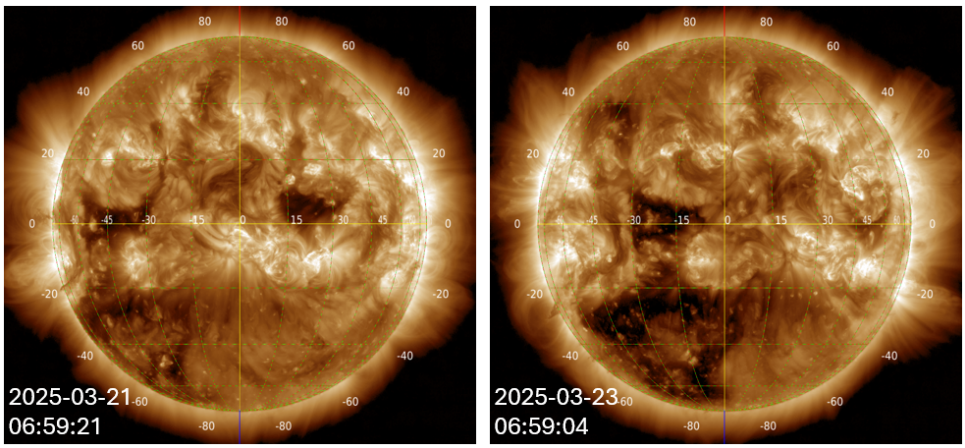

Figure 5.1: The SDO/AIA 193 Å observations across two days showing the large polar coronal hole, potentially influencing rotational analysis. We note that the position of the SolO is not along the Sun-Earth line and its separation angle with SDO changes through the considered time interval (21 – 28 March, 2025) from 25° to 60°.

polar coronal hole extending across this region. A visualization of this coronal hole is presented in Figure 5.1.

As coronal holes exhibit reduced EUV emission, together with altered coronal dynamics compared to surrounding quiet Sun regions, the observed discrepancy may be related to the magnetic topology present at this latitude. In particular, the reduced contrast and evolving open-field structures inside coronal holes may influence the identification and tracking of persistent coronal features in LT maps, as seen in Figure 4.3. The direct causal relationship between the presence of the polar coronal hole, which sourced the fast solar wind, and the obtained deviation at a latitude of -70° was not clearly established within the scope of this work. However, the coincidence between the obtained mismatch (see e.g. Figures 4.7 and 4.8) and the presence of the polar coronal hole suggests that local coronal magnetic structures may influence the measured rotation rates. Taking into account the particular shape of the southern polar coronal hole, its influence on the obtained results seems quite plausible. Namely, the crescent moon-like shape of the frontal part of the coronal hole had the deep part at latitudes of approximately -40° to -70° (see Figure 5.1). The most southern tip of the crescent seems to be at around -70°, which makes the influence of the coronal hole on our results rather probable. As such, the -70° measurement was taken as a statistical outlier and was not considered while applying the linear regression model.

The obtained coefficients of the two-parameter model are consistent in magnitude with previously reported values from the literature, particularly in studies using coronal bright points as rotational tracers Karachik et al. 2006; Kariyappa 2008; Brajša et al. 2004; Hara 2009. This agreement is especially noteworthy given that the present work focuses on high-latitude coronal observations obtained from EUI onboard Solar Orbiter. The agreement between the obtained rotation profile and previously established coronal rotation measurements, therefore, supports both the validity of the reprojection methodology and the scientific reliability of high-latitude EUI observations.

The overall quality of the regression further strengthens the obtained result. The fitted model yields a coefficient of determination exceeding $R^2 > 0.93$, indicating that the model explains the majority of the observed variance in the measurements. Additionally, the residuals remain relatively small across most latitude bands, with deviations generally remaining below 0.31 °/day. Together with the 95% confidence interval obtained from the fitted coefficients, this suggests that the two-parameter model provides a statistically robust representation of the measured latitude dependence of the coronal rotation rate.

The comparison between the obtained rotation profile and a few previously published coronal differential rotation models (Karachik et al. 2006; Kariyappa 2008; Brajša et al. 2004; Hara 2009) shows a generally consistent latitude dependence across all investigated studies. While small systematic differences between the individual models remain present, these are expected due to differences in observational wavelength, tracer selection, fitting methodology, and the specific coronal structures being analyzed. Nevertheless, the overall agreement between the independently obtained profiles further supports the conclusion that the rotational behavior measured in this work is physically consistent with previous coronal observations.

On the other hand, if we do not consider only a general, functional dependence but look into the detailed comparison of our results at selected latitudes with the recent work by Wöhl et al. 2010, a clear and systematic difference is obtained (Figure 4.9). The rotation rate obtained in our study shows a systematic shift and significantly smaller error bars in comparison with the results by Wöhl et al. 2010. Possible reasons for such a result are better resolution of SolO observations in comparison to SOHO-EIT data used in the study by Wöhl et al. 2010, and reduced projection effects due to particular, out of the ecliptic observations by SolO. The herein presented results, which are also the outcome of the first such study with the SolO/EUI observations, are important for the understanding of the Sun's differential rotation and are aimed to be published in a peer-reviewed journal.

5.4 Applicability of the Reprojection Framework to track Coronal Ejections

As an extension of the reprojection framework developed in this thesis, an attempt was made to apply the same methodology to study small-scale coronal ejections. This work was performed in the scope of a Space Weather project (Vanreppelen 2026; Schoefs 2026).

While in the previous chapters relatively motionless coronal structures were considered, in this part we aimed to study small, eruptive plasma motions extending radially outward from the solar surface. Such small eruptions are often considered to contribute, on small scales, to the mass transport occurring in the corona and solar wind.

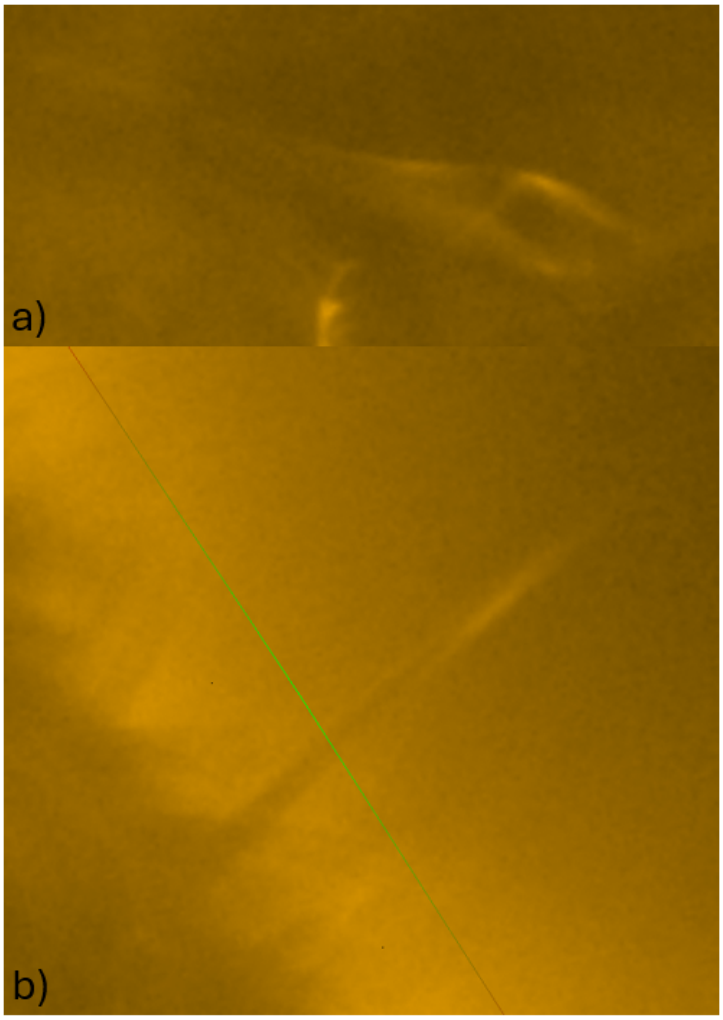

Figure 5.2: Two small-scale coronal ejections measured on 14 September 2025. a) On-disk measurement. b) Off-disk measurement. The line in the bottom figure represents the limb of the Sun, indicating that the small off-disk ejection crosses the limb.

The initial objective was to use the same ARC reprojection technique developed for the rotational analysis (Chapter 2) to measure the kinematics of these small-scale eruptions directly on the solar disk. However, while the reprojection procedure successfully minimizes surface foreshortening effects for structures located close to the solar limb, it proved not suitable for plasma structures extending vertically in the corona. Reprojection changes only the coordinate representation of the data and does not modify the original line-of-sight geometry of the observations. As a consequence, the apparent heights and trajectories of on-disk eruptions remain strongly affected by projection effects. A comparison between on- and off-disk ejections is presented in Figure 5.2.

A more fundamental problem to consider is that heliographic coordinates are only physically defined on the solar surface itself. For eruptive plasma structures extending beyond the limb, no unique heliographic coordinates exist. As a result, reliable reconstruction of the true three-dimensional geometry and propagation speed of the eruptions becomes very difficult without additional assumptions regarding the height and orientation of the studied ejections.

What could be directly noted was the fact that the on-disk measurements showed eruptions generally smaller and thus slower than in the case of the off-disk events. As these small-scale eruptions generally extended radially outward, on-disk measurements suffer from strong projection effects, and we observe a smaller apparent size, both in helioprojective and heliographic coordinates. Even with reprojecting the images, the latter coordinates do not significantly change. As such, the reprojected size would still be the same angular size as before, resulting in inaccurate measurements.

Additionally, identifying suitable on-disk events proved difficult. Small-scale coronal ejections generally exhibit low contrast against the highly structured coronal background and can be obscured by other dynamic activity on the solar disk. As a consequence, only a very small number of on-disk ejections were obtained.

We conclude that the reprojection framework developed in this thesis is best suited for studying long-lived and rather motionless coronal structures, such as rotational coronal features used in LT maps, rather than rapidly evolving radial ejections occurring in the corona. Consequently, the kinematic analysis of the small-scale eruptions was restricted to events observed near the visible limb, where the projected motion approximately coincides with the plane of the sky and the geometric interpretation becomes more reliable.

Although the reprojection approach was not appropriate for quantitative measurements of upward coronal ejections, this result remains important for defining the limitations of the methodology. Future investigations of coronal ejection dynamics may require other observation techniques, such as dedicated three-dimensional analysis, to properly account for the off-surface plasma motion.

Chapter 6

Conclusions and Further Outlook

This thesis investigated the rotational dynamics of coronal structures using observations from the EUI instrument onboard the ESA/NASA mission Solar Orbiter (SolO) that were taken with a unique out-of-ecliptic perspective on the solar polar regions. This investigation was built upon a dedicated data-processing pipeline developed to reproject solar observations into an azimuthal equidistant (ARC) system centered on the poles. This enabled the construction of longitude-time (LT) maps from which solar rotational motions can be measured.

The obtained measurements clearly reproduced the generally expected decrease in angular velocity with increasing heliographic latitude, confirming the impact of solar differential rotation on the observed coronal structures that do not show significant proper motions. The derived differential rotation profile shows a good agreement with previously published empirical rotation laws, demonstrating that the reprojection methodology and analysis framework developed in this work provide reliable measurements of solar rotational dynamics. Furthermore, the residuals between the observations and the fitted model remain limited, indicating that the adopted parametrization successfully captures the dominant latitude dependence of the rotation rate. Additionally to this general agreement with the previous studies, the detailed comparison with the results of recent study by Wöhl et al. 2010 shows a systematic shift in the rotation rate and significantly smaller error bars. Our results not only refine the one by Wöhl et al. 2010 but also clearly show how significant the impact of the projection effects can be.

A particularly important aspect of this work is the use of the novel SolO observations. Historically, measurements of solar rotation at high heliographic latitudes have been severely limited by the predominantly equatorial viewing geometry of solar observatories. Solar Orbiter, and EUI in particular, provide a unique opportunity to study the polar corona from increasingly elevated vantage points. As a result, this work contributes to the exploration of a latitude regime that has remained largely inaccessible in previous studies. The successful application of the methodology to these observations demonstrates that Solar Orbiter data can be used to investigate rotational dynamics in the polar corona with a level of detail that was previously unattainable.

Beyond providing the new results, which refine our understanding of the differential rotation, the methodology developed in this thesis provides a framework that can be directly compared with future differential rotation studies and empirical rotation laws. The obtained model parameters can therefore serve as an additional observational reference for future investigations of coronal rotation and its latitude dependence.

The applicability of the reprojection framework was also explored for small-scale coronal ejections. In contrast to rotational features, which are either rather motionless or move predominantly parallel to the solar surface, the considered small-scale eruptions propagate primarily in the radial direction. It was shown that the developed reprojection approach is unable to remove the associated line-of-sight projection effects, as information regarding the height of the structures above the solar surface is not recovered through the reprojection. Consequently, the methodology developed here is well-suited for studying long-lived rotational structures but not for quantitatively analyzing rapidly evolving radial ejections. This result establishes an important limitation of the technique and clarifies the range of phenomena for which it can be applied reliably.

Future work can further expand upon the results presented in this thesis. As Solar Orbiter continues its mission and reaches heliographic latitudes approaching 30°, observations of the polar regions will become increasingly favorable. This will provide access to a broader latitude range and allow the construction of differential rotation profiles extending from equatorial to polar regions. Increasing the number of measurements at each latitude will further improve the statistical robustness of the results and reduce uncertainties in the derived model parameters.

In addition, future studies may investigate whether the differential rotation profile can be described more accurately through the inclusion of higher-order terms, allowing the determination of a complete A-B-C differential rotation law. Improvements to the automated data-processing pipeline may also reduce computation times and facilitate the analysis of larger datasets. Finally, extending the methodology to observations obtained at other wavelengths could provide insight into the rotational behavior of structures located in different layers of the solar atmosphere.

Overall, the results presented in this thesis demonstrate that polar reprojection of SolO observations provides a robust and scientifically reliable framework for studying differential rotation in the solar corona. As Solar Orbiter continues to expand our view of the solar poles, the methods developed here offer a promising foundation for future investigations of high-latitude solar dynamics.

Scientific references

Ridpath, I (2012). *Stellar spectral classification*. URL: https://www.hermanusastronomy.co.za/wp-content/uploads/2018/11/Sun-%E2%80%93-Part-10-Stellar-spectral-classification-1.pdf.

Prša, Andrej et al. (2016). "Nominal values for selected solar and planetary quantities: IAU 2015 resolution B3". In: *The Astronomical Journal* 152.2, p. 41.

Cayrel de Strobel, G (1996). "Stars resembling the Sun". In: *The Astronomy and Astrophysics Review* 7.3, pp. 243–288.

Aerts, Conny and KU Leuven (2021). *STELLAR STRUCTURE & EVOLUTION*. Tech. rep.

Turck-Chièze a, S. et al. (1993). *The solar interior*. Tech. rep., pp. 57–235. URL: https://www.sciencedirect.com/science/article/pii/037015739390020E.

Interrante, Abbey and Abbey Interrante (Mar. 2025). "Layers of the Sun". In: URL: https://science.nasa.gov/blogs/the-sun-spot/2023/09/26/layers-of-the-sun/.

Adelberger, E. G. et al. (Apr. 2011). "Solar fusion cross sections. II. Theppchain and CNO cycles". In: *Reviews of Modern Physics* 83.1, pp. 195–245. DOI: 10.1103/revmodphys.83.195. URL: https://doi.org/10.1103/revmodphys.83.195.

Poletti, S (Jan. 2020). *Anatomy of the Sun*. URL: https://www.esa.int/ESA_Multimedia/Images/2020/01/Anatomy_of_the_Sun.

Kelley, Alessandra (2019). *Layers of the Sun, a scientific illustration*. URL: https://www.alessandrakelley.com/scimed/sunlayers.html.

Lang, Kenneth, Department of Physics, and Tufts University Astronomy Robinson Hall (1999). *Sun, Earth and Sky*. Tufts University. URL: http://ndl.ethernet.edu.et/bitstream/123456789/60570/1/Kenneth%20R.%20Lang_2006.pdf.

Schmitt, D. (Jan. 1993). "The Solar Dynamo". In: *The Cosmic Dynamo*. Ed. by F. Krause, K. H. Radler, and Gunther Rudiger. Vol. 157. IAU Symposium, p. 1.

Miesch, Mark S. (Jan. 2005). “Large-Scale Dynamics of the Convection Zone and Tachocline”. In: *Living Reviews in Solar Physics* 2. DOI: 10.12942/lrsp-2005-1. URL: https://doi.org/10.12942/lrsp-2005-1.

Basu, Sarbani, Sylvain G. Korzennik, and Sushanta C. Tripathy (Mar. 2026). “Latitude-dependent Time Variations of the Solar Tachocline”. In: *The Astrophysical Journal* 1000.2, p. 272. DOI: 10.3847/1538-4357/ae4c50. URL: https://doi.org/10.3847/1538-4357/ae4c50.

Beck, John G. (Jan. 2000). “A comparison of differential rotation measurements – (Invited Review)”. In: *Solar Physics* 191.1, pp. 47–70. DOI: 10.1023/a:1005226402796. URL: https://doi.org/10.1023/a:1005226402796.

Hotta, H., K. Kusano, and R. Shimada (July 2022). “Generation of Solar-like Differential Rotation”. In: *The Astrophysical Journal* 933.2, p. 199. DOI: 10.3847/1538-4357/ac7395. URL: https://doi.org/10.3847/1538-4357/ac7395.

Johns-Krull, Christopher M. (Jan. 2009). “Magnetic bond”. In: *Nature* 457.7226, pp. 158–159. DOI: 10.1038/457158a. URL: https://www.nature.com/articles/457158a.

Snodgrass, Herschel B. and Roger K. Ulrich (Mar. 1990). “Rotation of Doppler features in the solar photosphere”. In: *The Astrophysical Journal* 351, p. 309. DOI: 10.1086/168467. URL: https://ui.adsabs.harvard.edu/abs/1990ApJ...351..309S/abstract.

Mishra, Wageesh (Apr. 2022). “Evolution and Consequences of Coronal Mass Ejections in the Heliosphere”. In: DOI: 10.48550/arXiv.2204.09879.

Bame, S. J. et al. (Mar. 1974). “The quiet corona: Temperature and temperature gradient”. In: *Solar Physics* 35.1, pp. 137–152. DOI: 10.1007/bf00156963. URL: https://doi.org/10.1007/bf00156963.

Klimchuk, James A. (Feb. 2006). “On Solving the Coronal Heating Problem”. In: *Solar Physics* 234.1, pp. 41–77. DOI: 10.1007/s11207-006-0055-z. URL: https://doi.org/10.1007/s11207-006-0055-z.

De Moortel, Ineke and Philippa Browning (Apr. 2015). “Recent advances in coronal heating”. In: *Philosophical Transactions of the Royal Society A Mathematical Physical and Engineering Sciences* 373.2042, p. 20140269. DOI: 10.1098/rsta.2014.0269. URL: https://doi.org/10.1098/rsta.2014.0269.

Kuperus, Max, James A Ionson, and Daniel S Spicer (1981). “On the theory of coronal heating mechanisms”. In: *In: Annual review of astronomy and astrophysics. Volume 19.(A82-11551 02-90) Palo Alto, CA, Annual Reviews, Inc., 1981, p. 7-40.* 19, pp. 7–40.

Ball, David W. (2013). “Wien’s Displacement Law as a Function of Frequency”. In: *Journal of Chemical Education* 90.9, pp. 1250–1252. DOI: 10.1021/ed400113z.

eprint: https://doi.org/10.1021/ed400113z. URL: https://doi.org/10.1021/ed400113z.

Rochus, P. et al. (Jan. 2020). "The Solar Orbiter EUI instrument: The Extreme Ultraviolet Imager". In: *Astronomy and Astrophysics* 642, A8. DOI: 10.1051/0004-6361/201936663. URL: https://www.aanda.org/articles/aa/full_html/2020/10/aa36663-19/aa36663-19.html.

Lamy, Philippe et al. (2020). "Coronal Photopolarimetry with the LASCO-C2 Coronagraph over 24 Years [1996–2019]". In: *Solar Physics* 295.7, p. 89. DOI: 10.1007/s11207-020-01650-y.

Müller, D., B. Nicula, et al. (May 2017). "JHelioviewer". In: *Astronomy and Astrophysics* 606, A10. DOI: 10.1051/0004-6361/201730893. URL: https://www.aanda.org/articles/aa/full_html/2017/10/aa30893-17/aa30893-17.html.

Priest, Eric R. (Jan. 1982). *Solar Magnetohydrodynamics*. DOI: 10.1007/978-94-009-7958-1. URL: https://doi.org/10.1007/978-94-009-7958-1.

Gary, G. Allen (Oct. 2001). "Plasma Beta above a Solar Active Region: Rethinking the Paradigm". In: *solphys* 203.1, pp. 71–86. DOI: 10.1023/A:1012722021820.

Howard, Robert (1967). "Magnetic field of the Sun (observational)". In: *Annual Review of Astronomy and Astrophysics, vol. 5, p. 1* 5, p. 1. URL: https://ui.adsabs.harvard.edu/scan/manifest/1967ARA&A...5....1H.

Wiegelmann, Thomas et al. (Nov. 2014). *The magnetic field in the solar atmosphere*. Tech. rep., pp. 78–106. DOI: 10.1007/s00159-014-0078-7. URL: https://ui.adsabs.harvard.edu/abs/2014A%26ARv..22...78W/abstract.

Mackay, Duncan H. and Anthony R. Yeates (2012). *The Sun's Global Photospheric and Coronal Magnetic Fields: Observations and Models*. Tech. rep., p. 6. DOI: 10.12942/lrsp-2012-6. URL: http://www.livingreviews.org/lrsp-2012-6.

Moreau, René J. (1990). *Magnetohydrodynamics*. URL: https://books.google.be/books?hl=nl&lr=&id=47LnCAAAQBAJ&oi=fnd&pg=PR4&dq=magnetohydrodynamics&ots=5f0K9G0-d4&sig=Dh55TjJiMKfDlW_4KLkrzJq-32Q&redir_esc=y#v=onepage&q&f=false.

Nakariakov, Valery (2015). *Introduction to MHD*. Tech. rep. URL: http://goo.gl/oPgmzK.

Aschwanden, Markus J. (Jan. 2005). *Physics of the Solar Corona*. DOI: 10.1007/3-540-30766-4. URL: https://doi.org/10.1007/3-540-30766-4.

Chen, Francis F. and University of California at Los Angeles (2015). *Introduction to Plasma Physics and Controlled Fusion*. Third Edition. Springer. DOI: 10.1007/978-3-319-22309-4.

Cranmer, Steven R (2009). “Coronal holes”. In: *Living reviews in solar physics* 6.1, p. 3. URL: https://link.springer.com/article/10.12942/lrsp-2009-3.

Altschuler, Martin D, Dorothy E Trotter, and Frank Q Orrall (1972). “Coronal holes”. In: *Solar Physics* 26.2, pp. 354–365. URL: https://link.springer.com/article/10.1007/BF00165276.

Hollweg, Joseph V and Philip A Isenberg (2002). “Generation of the fast solar wind: A review with emphasis on the resonant cyclotron interaction”. In: *Journal of Geophysical Research: Space Physics* 107.A7, SSH–12. URL: https://agupubs.onlinelibrary.wiley.com/doi/full/10.1029/2001JA000270.

Feldman, U, E Landi, and NA Schwadron (2005). “On the sources of fast and slow solar wind”. In: *Journal of Geophysical Research: Space Physics* 110.A7. URL: https://agupubs.onlinelibrary.wiley.com/doi/full/10.1029/2004JA010918.

Borrero, Juan M. and Kiyoshi Ichimoto (Jan. 2011). “Magnetic Structure of Sunspots”. In: *Living Reviews in Solar Physics* 8, p. 4. DOI: 10.12942/lrsp-2011-4. URL: https://doi.org/10.12942/lrsp-2011-4.

Solanki, Sami K. (Apr. 2003). “Sunspots: An overview”. In: *The Astronomy and Astrophysics Review* 11.2-3, pp. 153–286. DOI: 10.1007/s00159-003-0018-4. URL: https://doi.org/10.1007/s00159-003-0018-4.

Van Driel-Gesztelyi, Lidia and Lucie May Green (Sept. 2015). “Evolution of Active Regions”. In: *Living Reviews in Solar Physics* 12.1. DOI: 10.1007/lrsp-2015-1. URL: https://doi.org/10.1007/lrsp-2015-1.

Bumba, V. et al. (1964). *A STUDY OF THE DEVELOPMENT OF ACTIVE REGIONS ON THE SUN*. Tech. rep., pp. 1492–1493.

Toriumi, Shin and Haimin Wang (May 2019). “Flare-productive active regions”. In: *Living Reviews in Solar Physics* 16.1, p. 3. DOI: 10.1007/s41116-019-0019-7. URL: https://doi.org/10.1007/s41116-019-0019-7.

Toriumi, Shin, Carolus J. Schrijver, et al. (Jan. 2017). “Magnetic Properties of Solar Active Regions That Govern Large Solar Flares and Eruptions”. In: *The Astrophysical Journey* 834.1, 56, p. 56. DOI: 10.3847/1538-4357/834/1/56. arXiv: 1611.05047 [astro-ph.SR].

Zhang, Juan et al. (2018). “Latitudinal migration of sunspots based on the ESAI database”. In: *Research in Astronomy and Astrophysics*, 7(12pp). DOI: 10.1088/16744527/18/1/7. URL: https://www.raa-journal.org/issues/all/2018/v18n1/202203/P020220324642773766595.pdf.

Kiger, Patrick J. (Aug. 2009). “How Sunspots Work”. In: URL: https://science.howstuffworks.com/sunspot.htm.

DeRosa, M. L., A. S. Brun, and J. T. Hoeksema (Sept. 2012). "SOLAR MAGNETIC FIELD REVERSALS AND THE ROLE OF DYNAMO FAMILIES". In: *The Astrophysical Journal* 757.1, p. 96. DOI: 10.1088/0004-637x/757/1/96. URL: https://doi.org/10.1088/0004-637x/757/1/96.

Smith, Edward J. (Aug. 2001). "The heliospheric current sheet". In: *Journal of Geophysical Research Atmospheres* 106.A8, pp. 15819–15831. DOI: 10.1029/2000ja000120. URL: https://doi.org/10.1029/2000ja000120.

Hoeksema, J. Todd, John M. Wilcox, and Philip H. Scherrer (Dec. 1983). "The structure of the heliospheric current sheet: 1978–1982". In: *Journal of Geophysical Research Atmospheres* 88.A12, pp. 9910–9918. DOI: 10.1029/ja088ia12p09910. URL: https://doi.org/10.1029/ja088ia12p09910.

Raouafi, N. E. et al. (July 2016). "Solar Coronal Jets: Observations, Theory, and Modeling". In: *Space Science Reviews* 201.1-4, pp. 1–53. DOI: 10.1007/s11214-016-0260-5. URL: https://pmc.ncbi.nlm.nih.gov/articles/PMC7477949/.

Harvey, Karen L. and Frank Recely (Dec. 2002). "Polar Coronal Holes During Cycles 22 and 23". In: *Solar Physics* 211.1, pp. 31–52. DOI: 10.1023/A:1022469023581.

Müller, D., O. C. St. Cyr, et al. (May 2020). *The Solar Orbiter mission Special issue*. Tech. rep., A1–. DOI: 10.1051/0004-6361/202038467. URL: https://doi.org/10.1051/0004-6361/202038467.

Pesnell, W. Dean, B. J. Thompson, and P. C. Chamberlin (Jan. 2012). "The Solar Dynamics Observatory (SDO)". In: *solphys* 275.1-2, pp. 3–15. DOI: 10.1007/s11207-011-9841-3.

Berghmans, D. et al. (July 2023). "First perihelion of EUI on the Solar Orbiter mission". In: *aap* 675, A110, A110. DOI: 10.1051/0004-6361/202245586. arXiv: 2301.05616 [astro-ph.SR].

Thompson, W. T., L-3 Communications GSI, and NASA Goddard Space Flight Center (Jan. 2006). *Coordinate systems for solar image data*. Tech. rep., pp. 791–803. DOI: 10.1051/0004-6361:20054262. URL: https://www.aanda.org/articles/aa/pdf/2006/14/aa4262-05.pdf.

Snyder, John P. (1993). *Google Books*. URL: https://www.google.be/books/edition/Flattening_the_Earth/0UzjTJ4w9yEC?hl=nl&gbpv=1&dq=isbn:0226767477&printsec=frontcover.

Sheeley, N. R. et al. (Nov. 1999). "Continuous tracking of coronal outflows: Two kinds of coronal mass ejections". In: *Journal of Geophysical Research Atmospheres* 104.A11, pp. 24739–24767. DOI: 10.1029/1999ja900308. URL: https://doi.org/10.1029/1999ja900308.

Davies, J. A. et al. (Jan. 2009). "A synoptic view of solar transient evolution in the inner heliosphere using the Heliospheric Imagers on STEREO". In: *Geophysical Re-*

search Letters 36.2. DOI: 10.1029/2008gl036182. URL: https://doi.org/10.1029/2008gl036182.

Conlon, T. M., S. E. Milan, and J. A. Davies (May 2014). "Assessing the Effect of Spacecraft Motion on Single-Spacecraft Solar Wind Tracking Techniques". In: *Solar Physics* 289.10, pp. 3935–3947. DOI: 10.1007/s11207-014-0549-z. URL: https://doi.org/10.1007/s11207-014-0549-z.

Plotnikov, I. et al. (June 2016). *Long-Term Tracking of Corotating Density Structures Using Heliospheric Imaging*. Tech. rep., pp. 1853–1875. DOI: 10.1007/s11207-016-0935-9.

The SunPy Community et al. (2020). "The SunPy Project: Open Source Development and Status of the Version 1.0 Core Package". In: *The Astrophysical Journal* 890 (1), pp. 68–. DOI: 10.3847/1538-4357/ab4f7a. URL: https://iopscience.iop.org/article/10.3847/1538-4357/ab4f7a.

Wöhl, H. et al. (May 2010). "A precise measurement of the solar differential rotation by tracing small bright coronal structures in SOHO-EIT images". In: *Astronomy and Astrophysics* 520, A29. DOI: 10.1051/0004-6361/200913081. URL: https://doi.org/10.1051/0004-6361/200913081.

Karachik, Nina, Alexei A. Pevtsov, and Isroil Sattarov (May 2006). "Rotation of Solar Corona from Tracking of Coronal Bright Points". In: *apj* 642.1, pp. 562–567. DOI: 10.1086/500820.

Kariyappa, R. (Sept. 2008). "Solar coronal rotation determined by X-ray bright points in Hinode/XRT and Yohkoh/SXT full-disc images". In: *aap* 488.1, pp. 297–301. DOI: 10.1051/0004-6361:200809598. arXiv: 0804.3508 [astro-ph].

Brajša, R. et al. (Feb. 2004). "Height correction in the measurement of solar differential rotation determined by coronal bright points". In: *aap* 414, pp. 707–715. DOI: 10.1051/0004-6361:20034082.

Hara, Hirohisa (June 2009). "Differential Rotation Rate of X-ray Bright Points and Source Region of their Magnetic Fields". In: *apj* 697.2, pp. 980–984. DOI: 10.1088/0004-637X/697/2/980.

Vanreppelen, L (2026). "Space Weather Project: Kinematics and Statistics of Small-Scale Coronal Ejections Part I". In.

Schoefs, R (2026). "Space Weather Project: Kinematics and Statistics of Small-Scale Coronal Ejections Part II". In.

Online documentation and websites

ATNF (2026). *Spectral Classes - Australia Telescope National Facility*. URL: https://www.atnf.csiro.au/resources/education/senior-astrophysics/spectroscopy/spectral-class/.

NCAR (2026). *What type of star is the Sun? — High Altitude Observatory*. URL: https://www2.hao.ucar.edu/education/about-the-sun/what-type-star-sun.

NASA (Aug. 2023). *It's Surprisingly Hard to Go to the Sun - NASA*. URL: https://www.nasa.gov/solar-system/its-surprisingly-hard-to-go-to-the-sun/.

Nave, R (2024). *Composition of the Sun*. URL: http://hyperphysics.phy-astr.gsu.edu/hbase/Tables/suncomp.html.

UCAR (2026). *Inside the Sun — Center for Science Education*. URL: https://scied.ucar.edu/learning-zone/sun-space-weather/inside-sun.

Bridgman, Tom (Nov. 2012). *The Active Sun from SDO: HMI Intensity*. URL: https://svs.gsfc.nasa.gov/3988/.

JHelioviewer - ESA (2017). *JHelioviewer*. URL: https://www.jhelioviewer.org/.

OpenStax (2017). *15.2 The Solar Cycle and Sunspots*. URL: https://pressbooks.bccampus.ca/astronomy1105/chapter/15-2-the-solar-cycle/.

SIDC (2014). *Maunder "butterfly" Diagram — SIDC*. URL: https://www.sidc.be/SILSO/maunder.

– (2026). *Monthly and smoothed sunspot number — SIDC*. URL: https://www.sidc.be/SILSO/monthlyssnplot.

Genç Halit, Yusuf (Nov. 2021). *What is solar cycle ?* URL: https://engineerforspace.com/2021/11/03/what-is-solar-cycle/.

ESA (2022). *What are solar flares?* URL: https://www.esa.int/Science_Exploration/Space_Science/What_are_solar_flares.

NOAA/SWPC (n.d.[a]). *About Space Weather: Coronal mass ejections*. URL: https://www.swpc.noaa.gov/phenomena/coronal-mass-ejections.

SIDC (2023). *Spot the moss, spicules, and coronal rain — SIDC*. URL: https://www.sidc.be/article/spot-moss-spicules-and-coronal-rain.

NASA/ESA (2026). *Realtime LASCO images*. URL: https://soho.nascom.nasa.gov/data/realtime-images.html.

NOAA/SWPC (n.d.[b]). *About Space Weather: Coronal holes*. URL: https://www.swpc.noaa.gov/phenomena/coronal-holes.

ESA (2019). *Solar Orbiter overview*. URL: https://www.esa.int/Science_Exploration/Space_Science/Solar_Orbiter_overview.

– (2026). *Solar Orbiter*. URL: https://www.esa.int/Science_Exploration/Space_Science/Solar_Orbiter.

SIDC (2021). *EUI website*. URL: https://www.sidc.be/EUI/about/instrument.

Wikipedia (Apr. 2026a). *Azimuthal equidistant projection*. URL: https://en.wikipedia.org/wiki/Azimuthal_equidistant_projection.

SunPy (n.d.[a]). *Fido*. URL: https://docs.sunpy.org/en/stable/generated/api/sunpy.net.Fido.html.

Group, FITS Working and IAUFWG (July 2016). *Definition of the Flexible Image Transport System (FITS)*. URL: https://fits.gsfc.nasa.gov/standard40/fits_standard40aa-le.pdf.

SunPy (n.d.[b]). *Maps (sunpy.map)*. URL: https://docs.sunpy.org/en/stable/reference/map.html.

– (n.d.[c]). *Rotating a Map*. URL: https://docs.sunpy.org/en/stable/generated/gallery/map/map_rotation.html.

– (n.d.[d]). *Cropping a Map*. URL: https://docs.sunpy.org/en/stable/generated/gallery/map/submaps_and_cropping.html.

Astropy (n.d.[a]). *SkyCoord — Astropy v7.2.0*. URL: https://docs.astropy.org/en/stable/api/astropy.coordinates.SkyCoord.html.

– (n.d.[b]). *World Coordinate System (Astropy.WCs)*. URL: https://docs.astropy.org/en/latest/wcs/index.html.

SunPy (n.d.[e]). *HMIMap*. URL: https://docs.sunpy.org/en/stable/generated/api/sunpy.map.sources.HMIMap.html#sunpy.map.sources.HMIMap.pixel_to_world.

Wikipedia (Feb. 2026b). *Q–Q plot*. URL: https://en.wikipedia.org/wiki/Q%E2%80%93Q_plot.

Chapter 7

Appendices

7.1 Appendix I: Data Extraction (Fido) Code

```
       import astropy.units as u
from sunpy.net import Fido, attrs as a
import sunpy_soar

start = "2025-03-21T00:00:00"
end = "2025-03-28T15:30:00"
range = a.Time(start, end)

from sunpy.net import Fido, attrs as a

eui_results = Fido.search(
    range,
    a.Instrument.eui,
    a.Level(2),
    a.soar.Product('eui-fsi304-image'),
)

print(eui_results)

outdir = "..."

files = Fido.fetch(eui_results, path=outdir)
```

7.2 Appendix II: Preprocessing and Reprojection Code

```
       import sunpy.map
from astropy.coordinates import SkyCoord
from sunpy.coordinates import frames
import astropy.units as u
import matplotlib.pyplot as plt
import math
import glob
import os
import numpy as np
from astropy.visualization.mpl_normalize import ImageNormalize
from astropy.visualization import AsinhStretch

# Import all files from a folder
fits_files = sorted(glob.glob(r"D:\KULeuven\Master Thesis\Foto en data dump\backup\fsi304_map\*.fits"))

# Folder to store each result
output_folder = r"D:\KULeuven\Master Thesis\Foto en data dump\backup\fsi304_high_lat_pictures"
os.makedirs(output_folder, exist_ok=True)

fits_output_folder = r"D:\KULeuven\Master Thesis\Foto en data dump\backup\fsi304_high_lat_fits"
os.makedirs(fits_output_folder, exist_ok=True)

# Main code that will transform each FITS file to a readable picture, derotate/centered/zoomed 1st result and reporjected 2nd result
for i, file in enumerate(fits_files):
    # Give an update in the terminal
    print(f"Frame {i+1} of {len(fits_files)} frames processing")

    ##############################################
    ##### GETTING CLEAR VIEW OF ORIGINAL DATA #####
    ##############################################
```

```
# Use sunpy to easily read out the fits file
my_map = sunpy.map.Map(file)

# Read-out values of the original data's rotation matrix. This will be used to de-rotate the original data and get a derotated view in the 1st result
cos = my_map.rotation_matrix[0,0] # Upper left cell
sin = my_map.rotation_matrix[1,0] # Lower left cell

# Find the rotation by using the arctan and convert to degrees. Use atan2 to know the correct quadrant (otherwise rotation cap of -90°/90°)
rotation = math.degrees(math.atan2(sin, cos))

# Derotate by the calculated angle. A positive rotation means the axes-frame is rotated clockwise
# if rotation<0:
#     my_map = my_map.rotate(-rotation*u.deg)
# else:
#     my_map = my_map.rotate(rotation*u.deg)

# The center of each original frame is always (0,0) in arcseconds. This coordinate will be used to center the 1st result
center = SkyCoord(0*u.arcsec, 0*u.arcsec, frame=my_map.coordinate_frame)

# A read-out value of the sun's radius in arcseconds. This radius will be used to get a clear view of the sun in the 1st result
radius = my_map.rsun_obs # arcsec

# Generate a new frame-limit for the zoomed-in map. This zoomed-in map will create a clear view with the sun almost filling the complete frame
# The 1/6th of the radius as "extra" space is chosen arbitrarily. Can be changed to anyone's liking
bottom_left = SkyCoord(Tx=0*u.arcsec -radius - 1/6 * radius, Ty=0*u.arcsec -radius - 1/6 * radius, frame=my_map.coordinate_frame)
top_right = SkyCoord(Tx=0*u.arcsec + radius + 1/6 * radius, Ty=0*u.arcsec + radius + 1/6 * radius, frame=my_map.coordinate_frame)

# This creates the actual zoomed-in map
my_map = my_map.submap(bottom_left, top_right=top_right)

########################
##### REPROJECTION #####
########################

# We need to choose the point on the map that will be the origin of the new reprojected image
# In this case, this will be solar north or south, depending on which pole is visible in the frames

# Find the tilt of the original data by asking for the latitude of the observer
tilt = my_map.carrington_latitude

if tilt > 0:
    origin = SkyCoord(my_map.heliographic_longitude, 90*u.deg, frame=frames.HeliographicStonyhurst, obstime=my_map.date, observer=my_map.observer_coordinate)
else:
    origin = SkyCoord(my_map.heliographic_longitude, -90*u.deg, frame=frames.HeliographicStonyhurst, obstime=my_map.date, observer=my_map.observer_coordinate)
# The latitude is fixed (90° or -90°). The longitude can be chosen independantly
# Here, the carrington longitude of the observer is chosen (as it is the center longitude in the original data)
# This chosen longitude will create a clear reference longitude for the later reprojection

frame=my_map.coordinate_frame

# The size of the new reprojected map in pixels (height/width)
out_shape = (1500,1500)

# The pixel scale of the new reprojected map
scale = [0.067, 0.067]*u.deg/u.pix

# This creates the actual reprojected data frame in a fits-file-form
out_header = sunpy.map.make_fitswcs_header(
    out_shape, # Size
    origin, # Origin
    scale=scale, # Scale
    projection_code="ARC" # The actual reprojection method.
)

# Reprojecting the old map to a new map such that plotting can be done easily
out_map = my_map.reproject_to(out_header)

# Masking the reprojected map such that the poles are "zoomed-in" to
y, x = np.indices(out_map.data.shape) # Contains the rows and columns respectively
cx, cy = np.array(out_map.data.shape[::-1]) / 2  # center coordinate (cx, cy)
r = np.sqrt((x - cx)**2 + (y - cy)**2)

center_pixel = SkyCoord(out_map.wcs.pixel_to_world(cx, cy))
edge_pixel = SkyCoord(out_map.wcs.pixel_to_world(cx+100, cy))
separation = center_pixel.separation(edge_pixel).to(u.deg)
pixels_per_deg = 100 / separation.value
desired_deg = 50
radius_pixels = desired_deg * pixels_per_deg
mask = r < radius_pixels
out_map.data[~mask] = np.nan

# This rotation fixed the north pole as "up" in this case. Not nessecary, but cleaner to look at
if tilt > 0:
    out_map = out_map.rotate(180*u.deg)

filename = f"reprojected_{i}.fits"
save_path = os.path.join(fits_output_folder, filename)

out_map.save(save_path, overwrite=True)
print(f"Saved reprojected fits {i+1} of {len(fits_files)}")

vmin = np.nanpercentile(my_map.data, 1)   # 1st percentile to avoid outliers
vmax = np.nanpercentile(my_map.data, 99)  # 99th percentile
norm = ImageNormalize(vmin=vmin, vmax=vmax, stretch=AsinhStretch())

# Plotting the first result (derotated, zoomed-in, centered original data)
```

```
    fig = plt.figure(figsize=(8,4))
    ax = fig.add_subplot(1, 2, 1, projection=my_map)
    # ax.set_axis_off()
    my_map.plot(axes=ax)
    my_map.draw_grid(axes=ax, color='blue') # A grid to see the latitudes/longitudes
    my_map.draw_limb(axes=ax, color='blue') # PLotting the limb
    ax.plot_coord(origin, 'o', color='red', fillstyle='none', markersize=20) # Highlight the north/south pole with a red circle

    # Plotting the second result (reprojected image with pole in the center)
    ax = fig.add_subplot(1, 2, 2, projection = out_map)
    # ax.set_axis_off()
    out_map.plot(axes=ax, norm=norm)
    out_map.draw_grid(axes=ax, color='blue') # A grid to see the latitudes/longitudes
    # out_map.draw_limb(axes=ax, color='blue') # Plotting the limb
    ax.plot_coord(origin, 'o', color='red', fillstyle='none', markersize=20) # Highlight the north/south pole with a red circle
    ax.set_title('Postel projection centered at ROI', y=-0.1)

    # Save each frame to the chosen folder
    output_path = os.path.join(output_folder, f"frame_{i:03d}.png")
    plt.savefig(output_path)
    plt.close(fig)

    print(f"figure {i+1}  of {len(fits_files)} saved")

    del my_map, out_map, fig, ax
```

7.3 Appendix III: Data Cube Construction and Slicing Code

```
       # ----------------------------------------
# 1) Load files and build CAR cube
# ----------------------------------------
import glob
import numpy as np
import astropy.units as u
from sunpy.map import Map
import matplotlib.pyplot as plt
from matplotlib.colors import LogNorm

files = sorted(glob.glob(r"D:\KULeuven\Master Thesis\Foto en data dump\backup\fsi304_high_lat_fits\*.fits"))
maps = Map(files, sequence=True)
maps.maps.sort(key=lambda m: m.date)

cube = np.stack([m.data for m in maps], axis=0)
n_time, n_lat, n_lon = cube.shape

m0 = maps[0]   # first map for coordinate queries

# ----------------------------------------
# 2) Build full latitude + longitude grids
# ----------------------------------------

# pixel grids
x_idx = np.arange(n_lon)
y_idx = np.arange(n_lat)

X, Y = np.meshgrid(x_idx, y_idx)

coords = m0.pixel_to_world(X * u.pix, Y * u.pix)

lat_grid = coords.lat.deg
lon_grid = coords.lon.deg
# print("Lat grid", lat_grid)
print(lat_grid[750, 750])
# print("Lon grid", lon_grid)

# ----------------------------------------
# 3) Select pixels near target latitude
# ----------------------------------------

target_lat = -60        # degrees
tolerance = 0.05        # latitude width

lat_mask = np.abs(lat_grid - target_lat) < tolerance
# print("Lat mask", lat_mask)

# ----------------------------------------
# 4) Extract longitude values for mask
# ----------------------------------------

selected_lons = lon_grid[lat_mask]
# print("Selected lons", selected_lons)

# sort by longitude
sort_idx = np.argsort(selected_lons)
sorted_lons = selected_lons[sort_idx]
# print("Sorted lons", sorted_lons)
```

```
# print(sorted_lons[0], sorted_lons[-1])
print(f"Longitude range = {np.abs(sorted_lons[-1] - sorted_lons[0])}")

# ----------------------------------------
# 5) Extract time{longitude slice
# ----------------------------------------

# flatten spatial dimensions
cube_2d = cube.reshape(n_time, -1)
flat_mask = lat_mask.flatten()

# select latitude ring
time_lat_values = cube_2d[:, flat_mask]  # (n_time, n_selected_pixels)

# sort by longitude
time_long_slice = time_lat_values[:, sort_idx]

# ----------------------------------------
# 6) Remove columns that are entirely NaN
# ----------------------------------------

col_nan_count = np.sum(np.isnan(time_long_slice), axis=0)
valid_cols = col_nan_count < n_time

time_long_slice = time_long_slice[:, valid_cols]
sorted_lons = sorted_lons[valid_cols]

print("Final longitude span:",
      sorted_lons[0], sorted_lons[-1])
print("Final longitude range:",
      np.abs(sorted_lons[-1] - sorted_lons[0]))

print("Final slice shape:", time_long_slice.shape)


# ----------------------------------------------------------
# 7) Plot the result
# ----------------------------------------------------------

points = []

def onclick(event):
    if event.inaxes is None:
        return

    # ignore clicks while zoom or pan is active
    if fig.canvas.toolbar.mode != "":
        # modes are: "zoom rect", "pan/zoom"
        return

    # store clicked point
    points.append((event.xdata, event.ydata))
    print(f"Point {len(points)-1}: {points[-1]}")

    # Draw the point
    ax.plot(event.xdata, event.ydata, "ro", linewidth=1, color="black")

    # If we have an even number of points, connect the last two
    if len(points) % 2 == 0:
        x1, y1 = points[-2]
        x2, y2 = points[-1]
        ax.plot([x1, x2], [y1, y2], "r-", linewidth=1)

    fig.canvas.draw()


# Display the image
fig, ax = plt.subplots()
extent = [sorted_lons[0], sorted_lons[-1], 0, n_time-1]
data = time_long_slice[np.isfinite(time_long_slice)]
vmin = np.percentile(data, 1)     # bottom 1%
vmax = np.percentile(data, 99.9)    # top 99%
ax.imshow(time_long_slice, aspect='auto', origin='lower', extent=extent, cmap="viridis", norm=LogNorm(vmin=vmin, vmax=vmax))


cid = fig.canvas.mpl_connect('button_press_event', onclick)

plt.title(f"Longitude-Time slice at {target_lat}° LAT", fontsize=36)
plt.xlabel("Stonyhurst Longitude (°)", fontsize=36)
plt.ylabel("Time Index (0.5hr)", fontsize=36)
plt.xticks(fontsize=32)
plt.yticks(fontsize=32)
plt.show()

# ----------------------------------------------------------
# 8) Caclulate slopes and intensities
# ----------------------------------------------------------

print("\nPOINT PAIRS AND SLOPES")
slopes = []

for i in range(0, len(points) - 1, 2):
    # Select points
    (x1, y1) = points[i]
    (x2, y2) = points[i + 1]
```

```
    # Convert to nearest indices for intensity values
    lon_idx1 = np.argmin(np.abs(sorted_lons - x1))
    lon_idx2 = np.argmin(np.abs(sorted_lons - x2))
    time_idx1 = int(round(y1))
    time_idx2 = int(round(y2))

    # Extract intensities
    I1 = time_long_slice[time_idx1, lon_idx1]
    I2 = time_long_slice[time_idx2, lon_idx2]

    # Calculate slope
    slope = (y2 - y1) / (x2 - x1)
    slopes.append(slope)
    print(f"Pair {i//2}: ({x1:.2f}, {y1:.2f}) -> ({x2:.2f}, {y2:.2f}), slope = {slope:.4f}")

if slopes:
    avg_slope = sum(slopes) / len(slopes)
    print(f"\nAverage slope of all line segments: {avg_slope:.4f}")
else:
    print("\nNot enough points to form a single line segment.")

print("Slope ", 1/avg_slope * 2 * 24)

# ------------------------------------------------------
# 9) save the result to a txt file
# ------------------------------------------------------

output_file = f"line_slopes_output{target_lat}_304_2.txt"

with open(output_file, "w") as f:
    f.write("Pair\tX1\tY1\tX2\tY2\tSlope\tIntensity1\tIntensity2\n")
    for i in range(0, len(points) - 1, 2):
        (x1, y1) = points[i]
        (x2, y2) = points[i + 1]

        # Convert click coordinates to indices
        lon_idx1 = np.argmin(np.abs(sorted_lons - x1))
        lon_idx2 = np.argmin(np.abs(sorted_lons - x2))
        time_idx1 = int(round(y1))
        time_idx2 = int(round(y2))

        # Extract intensities
        I1 = time_long_slice[time_idx1, lon_idx1]
        I2 = time_long_slice[time_idx2, lon_idx2]

        slope = (y2 - y1) / (x2 - x1)
        f.write(f"{i//2}\t{x1:.6f}\t{y1:.6f}\t{x2:.6f}\t{y2:.6f}\t{slope:.6f}\t{I1:.6f}\t{I2:.6f}\n")

    if slopes:
        avg_slope = sum(slopes) / len(slopes)
        f.write(f"\nAverage slope:\t{((1/avg_slope)*24):.6f}\n")
    else:
        f.write("\nNot enough points to form a single line segment.\n")

print(f"\nSaved results to: {output_file}")
```

7.4 Appendix IV: Slope Reading and Plotting Code

```
        import math as m
import numpy as np
from scipy.stats import norm


x_deg = [41, 45, 50, 55, 60, 65, 70, 75]
x_rad = []
rot_values = [12.52, 12.35, 12.19, 12.03, 11.36, 11.22, 12.13, 10.37]
sigmas = [0.877, 0.787, 0.998, 0.961, 0.992, 1.206, 1.477, 1.156]
sizes = [93, 89, 74, 77, 75, 63, 49, 23]

sigmas_new = sigmas / np.sqrt(sizes)


for x in x_deg:
    new_x = x * m.pi / 180
    x_rad.append(new_x)

print(x_rad)

import numpy as np
import matplotlib.pyplot as plt

# Constants (deg/day)
A = 14.713
B = -2.396
C = -1.787

def solar_differential_rotation(theta):
    return A + B * np.sin(theta)**2 + C * np.sin(theta)**4

# Latitude array
```

```
latitudes = np.linspace(40*m.pi/180, 90*m.pi/180, 500)

# Compute rotation
omega = solar_differential_rotation(latitudes)

omega_values = []
for x in x_rad:
    w = solar_differential_rotation(x)
    omega_values.append(w)
print(omega_values)

colors = ["blue", "green", "pink", "orange", "red", "purple", "gray", "lightblue"]

plt.figure(figsize=(10,7))
plt.plot(latitudes, omega)
for x,y,s,c in zip(x_rad,rot_values,sigmas,colors):
    plt.errorbar(x,y, yerr=s, fmt="o", capsize=3, label=f"{(x*180/np.pi):.0f}°", color=c)
plt.xlabel("Heliographic Latitude (rad)", fontsize=26)
plt.ylabel("Angular Velocity (°/day)", fontsize=26)
plt.xticks(fontsize=24)
plt.yticks(fontsize=24)
plt.title("Comparison between observed \n and expected angular velocities", fontsize=24)
plt.legend(fontsize=20)
plt.tight_layout()
plt.grid()
# plt.show()

residuals = []
for x,y in zip(omega_values, rot_values):
    r = x - y
    residuals.append(r)

plt.figure(figsize=(10,7))
plt.hlines(0, x_rad[0], x_rad[-1], linewidth=3, color="black")
for x,y,c in zip(x_rad,residuals,colors):
    plt.scatter(x,y, label=f"{(x*180/np.pi):.0f}°", color=c)
plt.legend(fontsize=20)
plt.title("Residual plot between observed \n and expected angular velocities", fontsize=24)
plt.xlabel("Heliographic Latitude (rad)", fontsize=26)
plt.ylabel("Angular Velocity (°/day)", fontsize=26)
plt.xticks(fontsize=24)
plt.yticks(fontsize=24)
plt.grid()
plt.tight_layout()
plt.show()

res_perc = []
for x,y in zip(residuals,omega_values):
    r = x/y * 100
    res_perc.append(r)

print("Latitude values in degrees:", x_deg)
print("Latitude values in radians:", x_rad)
print("Observed angular velocities:", rot_values)
print("Observed standard deviations:", sigmas)
print("Expected angular velocities:", omega_values)
print("Observed residuals:", residuals)
print("Observed percentage based residuals:", res_perc)

import pandas as pd

# Create a DataFrame with all quantities
df = pd.DataFrame({
    "Latitude (deg)": x_deg,
    "Latitude (rad)": x_rad,
    "Observed omega": rot_values,
    "Sigma": sigmas,
    "Expected omega": omega_values,
    "Residual": residuals,
    "Residual%": res_perc
})

# Optional: round values for easier reading
df = df.round(3)

# Display in terminal
print(df)
```

7.5 Appendix V: Statistical Analysis: Histograms, Gaussians, and QQ-Plots

```
        import numpy as np
from scipy.stats import norm
import matplotlib.pyplot as plt
import pandas as pd
from scipy.stats import norm

lat = -50
```

```
data = pd.read_csv(f"latitude_slopes_folder/line_slopes_output{lat}_304_2.txt", sep='\s+')

pair = data["Pair"]
X1 = data["X1"]
Y1 = data["Y1"]
X2 = data["X2"]
Y2 = data["Y2"]
slope = data["Slope"]
I1 = data["Intensity1"]
I2 = data["Intensity2"]

# Slope histogram plotting

slope_clean = np.array(slope)
slope_clean = slope_clean[np.isfinite(slope_clean)]

print(np.median(slope_clean))

mu, std = norm.fit(slope_clean)

x = np.linspace(min(slope_clean), max(slope_clean), 500)
pdf = norm.pdf(x, mu, std)

plt.hist(slope_clean, bins="auto", density=True, alpha=0.6)
plt.plot(x, pdf)
plt.xlabel("Slope (deg/day)", fontsize=24)
plt.ylabel("Counts", fontsize=24)
plt.xticks(fontsize=16)
plt.yticks(fontsize=16)
plt.title(f"Gaussian Fit {lat} LAT: \n mu={mu:.3f}, sigma={std:.3f}", fontsize=24)
plt.tight_layout()
plt.show()

import scipy.stats as stats

stats.probplot(slope_clean, dist="norm", plot=plt)
plt.title(f"Q-Q Plot {lat} LAT", fontsize=24)
plt.xticks(fontsize=16)
plt.yticks(fontsize=16)
plt.xlabel("Theoretical Quantiles", fontsize=24)
plt.ylabel("Ordered Slope Values", fontsize=24)
plt.tight_layout()
plt.show()


data41 = pd.read_csv(r"C:\Users\lukav\OneDrive\Leuven mapje\Master Thesis\Coding\latitude_slopes_folder\line_slopes_output-41_304_2.txt", sep="\t")["Slope"][:-1]
data45 = pd.read_csv(r"C:\Users\lukav\OneDrive\Leuven mapje\Master Thesis\Coding\latitude_slopes_folder\line_slopes_output-45_304_2.txt", sep="\t")["Slope"][:-1]
data50 = pd.read_csv(r"C:\Users\lukav\OneDrive\Leuven mapje\Master Thesis\Coding\latitude_slopes_folder\line_slopes_output-50_304_2.txt", sep="\t")["Slope"][:-1]
data55 = pd.read_csv(r"C:\Users\lukav\OneDrive\Leuven mapje\Master Thesis\Coding\latitude_slopes_folder\line_slopes_output-55_304_2.txt", sep="\t")["Slope"][:-1]
data60 = pd.read_csv(r"C:\Users\lukav\OneDrive\Leuven mapje\Master Thesis\Coding\latitude_slopes_folder\line_slopes_output-60_304_2.txt", sep="\t")["Slope"][:-1]
data65 = pd.read_csv(r"C:\Users\lukav\OneDrive\Leuven mapje\Master Thesis\Coding\latitude_slopes_folder\line_slopes_output-65_304_2.txt", sep="\t")["Slope"][:-1]
data70 = pd.read_csv(r"C:\Users\lukav\OneDrive\Leuven mapje\Master Thesis\Coding\latitude_slopes_folder\line_slopes_output-70_304_2.txt", sep="\t")["Slope"][:-1]
data75 = pd.read_csv(r"C:\Users\lukav\OneDrive\Leuven mapje\Master Thesis\Coding\latitude_slopes_folder\line_slopes_output-75_304_2.txt", sep="\t")["Slope"][:-1]
data80 = pd.read_csv(r"C:\Users\lukav\OneDrive\Leuven mapje\Master Thesis\Coding\latitude_slopes_folder\line_slopes_output-80_304_2.txt", sep="\t")["Slope"][:-1]

data_dict = {
    "41": 360/data41,
    "45": 360/data45,
    "50": 360/data50,
    "55": 360/data55,
    "60": 360/data60,
    "65": 360/data65,
    "70": 360/data70,
    "75": 360/data75,
    "80": 360/data80,
}

labels = [-41, -45, -50, -55, -60, -65, -70, -75, -80]
means = [12.52, 12.35, 12.19, 12.03, 11.36, 11.22, 12.13, 10.37]
sigmas = [0.877, 0.787, 0.998, 0.961, 0.992, 1.206, 1.477, 1.156]
colors = ["blue", "green", "pink", "orange", "red", "purple", "gray", "lightblue"]

# Choose an x-range wide enough to cover all distributions
x_min = min(mu - 4*sigma for mu, sigma in zip(means, sigmas))
x_max = max(mu + 4*sigma for mu, sigma in zip(means, sigmas))
x = np.linspace(x_min, x_max, 1000)

plt.figure(figsize=(10, 10))

for mu, sigma, label, color in zip(means, sigmas, labels, colors):
    # Gaussian probability density function
    y = (1 / (sigma * np.sqrt(2*np.pi))) * np.exp(-0.5 * ((x - mu) / sigma)**2)

    # Plot the curve
    plt.plot(x, y, linewidth=2, label=label, color=color, alpha=0.7)

    # Fill under the curve with transparency
    plt.fill_between(x, y, alpha=0.25)

plt.xlabel("Angular Velocity (°/day)", fontsize=30)
plt.ylabel("Distribution", fontsize=30)
plt.title("Gaussian Distributions of \n the Angular Velocity", fontsize=30)
plt.xlim(8, 16)
plt.xticks(fontsize=24)
plt.yticks(fontsize=24)
```

```
plt.legend(fontsize=24)
plt.grid(alpha=0.3)
plt.tight_layout()
plt.show()
```

7.6 Appendix VI: Regression and Comparison

```
       import numpy as np
import matplotlib.pyplot as plt
import statsmodels.api as sm
import pandas as pd

theta = np.array([0.716, 0.785, 0.873, 0.960, 1.047, 1.134, 1.309])
omega = np.array([12.52, 12.35, 12.19, 12.03, 11.36, 11.22, 10.37])
sigma = np.array([0.877, 0.787, 0.998, 0.961, 0.992, 1.206, 1.156])
sigma_N = np.array([0.091, 0.083, 0.116, 0.110, 0.115, 0.152, 0.241])

sin2 = np.sin(theta)**2

X = sm.add_constant(sin2)

model2 = sm.OLS(omega, X)
results = model2.fit()

A2, B2 = results.params

print(results.summary())
print(f"A = {A2:.4f}")
print(f"B = {B2:.4f}")

ci = results.conf_int(alpha=0.05)

# print(ci)

A_low, A_high = ci[0]
B_low, B_high = ci[1]

# print(A_low, B_low)

theta_cont = np.linspace(0, np.pi/2, 400)
omega_cont2 = A2 + B2*np.sin(theta_cont)**2

omega_low = A_low + B_low * np.sin(theta_cont)**2
omega_high = A_high + B_high * np.sin(theta_cont)**2

# literature models

omega_model_3 = (
    17.6
    - 4.5*np.sin(theta_cont)**2
)

omega_model_4 = (
    14.39
    - 1.91*np.sin(theta_cont)**2
    - 2.45*np.sin(theta_cont)**4
)

omega_model_5 = (
    14.34
    - 1.30*np.sin(theta_cont)**2
    - 2.30*np.sin(theta_cont)**4
)

omega_model_6 = (
    14.454
    - 2.22*np.sin(theta_cont)**2
    - 2.22*np.sin(theta_cont)**4
)

omega_model_7 = (
    16.0
    - 0.7*np.sin(theta_cont)**2
    - 4.9*np.sin(theta_cont)**4
)

omega_model_8 = (
    14.19
    - 4.2*np.sin(theta_cont)**2
)

fig, ax = plt.subplots(figsize=(9, 6))

# Literature models
# l1, = ax.plot(theta_cont, omega_model_3, color="#0072B2", lw=1.8, label="Kariyappa (2008)")
l2, = ax.plot(theta_cont, omega_model_4, color="#009E73", lw=1.8, label="Hara (2009)")
l3, = ax.plot(theta_cont, omega_model_5, color="#CC79A7", lw=1.8, label="Karachik (2006)")
l4, = ax.plot(theta_cont, omega_model_6, color="#E69F00", lw=1.8, label="Brajsa (2004)")
# l5, = ax.plot(theta_cont, omega_model_7, color="#56B4E9", lw=1.8, label="Karachick (2006)")
l6, = ax.plot(theta_cont, omega_model_8, color="#D55E00", lw=1.8, label="Kariyappa (2008)")
```

```
# Your model + data
ci = ax.fill_between(theta_cont, omega_low, omega_high,
                     color="0.75", alpha=0.35, label="95% CI")

fit, = ax.plot(theta_cont, omega_cont2, color="black", lw=4, label="This work")

data = ax.errorbar(theta, omega, yerr=sigma_N, color="black", label="Data", zorder=5, fmt='o', capsize=5)

# First legend: literature models
leg1 = ax.legend(
    # handles=[l2, l3, l4, l6],
    handles=[l4, l3, l6, l2],
    loc="lower left",
    fontsize=22,
    title_fontsize=22,
    frameon=True
)

# Keep first legend when adding second one
ax.add_artist(leg1)

# Second legend: your result
ax.legend(
    handles=[fit, ci, data],
    loc="upper right",
    fontsize=22,
    title_fontsize=22,
    frameon=True
)

ax.set_xlabel("LAT (°)", fontsize=22)
ax.set_ylabel("Rotation rate (°/day)", fontsize=22)
ax.grid(True, alpha=0.35)
ax.tick_params(axis='both', labelsize=22)
ax.set_title("Comparison between the obtained model \n and other models from literature", fontsize=22)

degree_ticks = np.array([0, 10, 20, 30, 40, 50, 60, 70, 80, 90])
radian_ticks = np.deg2rad(degree_ticks)

ax.set_xticks(
    radian_ticks,
    [f"{d}°" for d in degree_ticks],
    fontsize=22
)


plt.tight_layout()
plt.show()

plt.subplots(figsize=(9, 6))
# plt.errorbar(theta, omega, yerr=sigma, color="black", label="Data", zorder=5, fmt='o', capsize=5)
plt.fill_between(theta_cont, omega_low, omega_high, color="0.75", alpha=0.35)
plt.plot(theta_cont, omega_cont2, color="black", lw=4)

colors = ["blue", "green", "pink", "orange", "red", "purple", "gray", "lightblue"]
for x,y,s,c in zip(theta,omega,sigma_N,colors):
    plt.errorbar(x,y, yerr=s, fmt="o", capsize=5, label=f"{(-x*180/np.pi):.0f}°", color=c, zorder=5)
plt.xlim(0.6, 1.4)
plt.ylim(8,15)

plt.xlabel("LAT (°)", fontsize=22)
plt.ylabel("Rotation rate (°/day)", fontsize=22)
plt.grid(True, alpha=0.35)

degree_ticks = np.array([35, 40, 45, 50, 55, 60, 65, 70, 75, 80])
radian_ticks = np.deg2rad(degree_ticks)

plt.xticks(
    radian_ticks,
    [f"{d}°" for d in degree_ticks],
    fontsize=22
)

plt.yticks(fontsize=22)
plt.legend(fontsize=22, ncol=2)
plt.title("Model of the measured rotation rates \n together with 95% CI", fontsize=22)
plt.show()

omega_model_points = A2 + B2*np.sin(theta)**2
residuals = omega - omega_model_points

plt.subplots(figsize=(9, 4))

for x, r, s, c in zip(theta, residuals, sigma_N, colors):
    plt.errorbar(
        x, r,
        yerr=s,
        fmt="o",
        capsize=5,
        color=c,
        label=f"{(-x*180/np.pi):.0f}°",
        zorder=5
    )

plt.axhline(0, color="black", lw=2, linestyle="--")
```

```
plt.xlim(0.6, 1.4)

degree_ticks = np.array([35, 40, 45, 50, 55, 60, 65, 70, 75, 80])
radian_ticks = np.deg2rad(degree_ticks)

plt.xticks(
    radian_ticks,
    [f"{d}°" for d in degree_ticks],
    fontsize=22
)

plt.yticks(fontsize=22)
plt.xlabel("LAT (°)", fontsize=22)
plt.ylabel("Residuals (°/day)", fontsize=22)
plt.title("Residuals between measured values and model", fontsize=22)

plt.grid(True, alpha=0.35)
plt.legend(fontsize=16, ncol=2)

plt.tight_layout()
plt.show()

df = pd.DataFrame({
    "theta_rad": theta,
    "theta_deg": -theta * 180 / np.pi,
    "omega_measured": omega,
    "omega_model": omega_model_points,
    "sigma_omega": sigma_N,
    "residual": residuals
})

df_rounded = df.round(2)

print(df_rounded)
```

Code of conduct and transparency statement on the use of GenAI for KU Leuven-students (academic year 2025-2026)

Generative AI (GenAI) assistance tools can be used to generate various types of content, including text, images, code, video, music, or combinations thereof. Common examples of such tools include ChatGPT, Google Gemini, Microsoft Copilot, Midjourney, Claude.ai, Perplexity.ai, and DALL·E, among others.

This code of conduct is a tool that helps students to be transparent about the use of GenAI and fits within the university's principles on academic integrity.

Important guidelines and remarks

- **Sensitive or personal data:** Some GenAI tools protect your input and sensitive or personal data better than others. There is often no transparency on what the owners of the AI applications do with the data entered. Therefore, **do not enter sensitive or personal data in free GenAI tools.** More info about what sensitive and personal data are, is described in the three confidentiality levels of the KU Leuven data classification model (non-confidential, confidential, strictly confidential). For confidential data you should preferably use **M365 Copilot Chat with your KU Leuven account**. If you use another GenAI tool, you must be **absolutely certain** it does **not store or reuse the data you enter**. **Try to avoid entering these data. Do so only if strictly necessary, and only to the extent required. For personal data, work with anonymous or pseudonymized data.** Additionally, in case of strictly confidential data this should first be discussed with the teaching staff of the course or your thesis supervisor.
- **Copyrighted materials**: For **lawfully obtained copyrighted material** you should preferably use **M365 Copilot Chat with your KU Leuven account**. If you use another GenAI tool, you must be **absolutely certain** it does **not store or reuse the data you enter**.
- GenAI assistance may not be used for data or topics covered by a **Non-Disclosure Agreement (NDA)**. Even in the absence of an NDA, certain information may still need to be treated as confidential—for example, due to regulatory requirements or the risk of significant harm to the university if disclosed. In case of doubt, check with your teaching staff or supervisor.
- If your master's thesis is under **embargo**, you should first discuss with your supervisor whether the use of GenAI is permitted.
- Before using a GenAI tool, always consider whether its use is responsible, including from a **sustainability perspective** (e.g. when using GenAI as a search engine, language assistant,…).
- **Take a scientific and critical attitude** when interacting with GenAI assistance and interpreting its output, that may not always be correct.
- As a student you are responsible for complying with Article 84 of the Regulations on Education and Examinations: your report or thesis should reflect your own knowledge, understanding and skills. Be aware that plagiarism rules also apply to (work that is the result of) the use of GenAI assistance tools.

> ***Exam Regulations Article 84****: "Every conduct individual students display with which they (partially) inhibit or attempt to inhibit a correct judgement of their own knowledge, understanding and/or skills or those of other students, is considered an irregularity which may result in a suitable penalty. A special type of irregularity is plagiarism, i.e. copying the work (ideas, texts, structures, designs, images, plans, codes , ...) of others or prior personal work in an exact or slightly modified way without adequately acknowledging the sources. Every possession of prohibited resources during an examination (see article 65) is considered an irregularity."*

- In order to maintain academic integrity and avoid plagiarism, **more information about being transparent on the use of GenAI assistance and about correctly citing and referencing GenAI** can be found on this website for students (Dutch/English).
- **Additional reading: KU Leuven guidelines on responsible use of Generative AI tools, and other information** (Dutch/English)

A few final words

If you are uncertain whether or not you should declare your use of GenAI tools, we suggest that you discuss this with your instructor or supervisor. It is always safer to declare GenAI use, even when it is not strictly required. However, declaring GenAI use does not entail that its use is allowed; the right column in the table below provides more detailed instructions in this regard (code of conduct).

Moreover, advanced AI tools are evolving rapidly, and their capabilities have expanded significantly in a short period of time. As a result, we do not yet have all the answers about their responsible use. Finally, it is important to follow-up on the most recent evolutions in AI technologies, to have an open mind but also to be a bit cautious, to communicate with instructors, teaching assistants, supervisors and peers, to be as transparent as we can, and to learn together as we move along.

Student name: LUKA VANREPPELEN **Student number:** r1046217

Please indicate with "X" whether it relates to a course assignment or to the Bachelor's or Master's thesis:

O This form is related to a **course assignment**.

Course name: ..... **Course number:** .....

This form is related to **my** O **Bachelor's or** X **Master's thesis**.

Title Bachelor's or Master's thesis: Analysis of the dynamics observed at the solar coronal poles by the Extreme Ultraviolet Imager onboard Solar Orbiter

Supervisor: Jasmina Magdalenić Zhukov, David Berghmans

Daily supervisor: Jasmina Magdalenić Zhukov, David Berghmans

Please indicate with "X":

O **I did not use** any GenAI assistance tool.

X **I did use** GenAI Assistance. In this case **specify which ones** (e.g. ChatGPT, M365 Copilot,...):

Chat GPT

GenAI assistance used as/for:	**Name of the GenAI tool(s) used.** If helpful, also describe in which way you were using GenAI related to what is specified as code of conduct.	**Code of conduct:**
		For each of the categories below, always take into account the important guidelines and remarks mentioned above (e.g. copyrighted data, sensitive or personal data,…).
As a language assistant for reviewing or improving texts I wrote myself	Chat GPT	This use is similar to using spelling and grammar check tools. In general, you do not have to refer to such kind of GenAI use in the text. **However, be careful:** - When using GenAI tools on texts you did not write yourself to improve the text, **you have to refer to the original source or author**, otherwise you are committing plagiarism and thus an irregularity.
As a paraphrasing tool	Chat GPT Writing text, and asking to polish the language	This use is allowed except when it is prohibited by the teacher or the program of study. You may paraphrase your own text or texts by an author other than yourself and take inspiration from what a GenAI tool or another tool suggests (unless it is not allowed). In general, you do not have to refer to such kind of GenAI use or other paraphrasing tools in the text. **However, be careful:** - If it entails text by an author other than yourself, **you are not allowed to include that paraphrased text without reference to the original source or author.** Without such reference, you would be committing plagiarism and thus an irregularity.
For translation aid to improve texts I wrote myself or to better understand text from others		This use is allowed except when it is prohibited by the teacher or the program of study. It is similar to using translation tools (Google translate, DeepL, …). In general, you do not have to refer to such kind of GenAI use in the text.

		However, be careful: - **You are not allowed to include that translated text without reference to the original source or author.** Without such reference, you would be committing plagiarism and thus an irregularity. - Always check the translated text for correctness and meaning.
As a search engine to get information on a topic or to search for existing research on the topic	ChatGPT	This use is similar to e.g. a Google search or checking Wikipedia. If you write your own text based on this information, you do not have to refer to the use of GenAI in the text. **You only have to refer to the existing research and references you have checked and used** (without such references you would be committing plagiarism and thus committing an irregularity). **However, be careful:** - Be aware that the output of the GenAI tool cannot be guaranteed as a 100% reliable source of information. The output may not be entirely correct and/or be limited due to the databases it uses. Moreover, knowledge evolves and may change over time; therefore, the database of the GenAI tool may not be up to date. Therefore, **verify the information and do not just copy-paste it** as you should understand and critically process everything you are writing.
For literature search		This use is comparable to e.g. a Google Scholar search. You do not have to refer to such kind of GenAI use; **you only have to refer to the literature references you have checked and used** (without such references you would be committing plagiarism and thus committing an irregularity).. **However, be careful:** - Be aware that the search output is restricted to the database the GenAI tool is built on. After this initial search, look for scientific sources and conduct your own analysis of the source documents. **Interpret, analyse and process**

		the information you obtained; verify it and do not just copy-paste it as you should understand and critically process everything you are writing. - Be aware that some GenAI tools may **output no or wrong references**. As a student you are responsible for further checking and verifying the absence or correctness of references; do not just copy-paste it.
For generating programming code	ChatGPT • Solving bugs/issues • Plotting-related questions	Use of GenAI for coding is allowed except when it is prohibited by the teacher or the program of study. If used for coding, correctly mention the use of GenAI assistance in accordance with the instructions on the page on being transparant about the use of GenAI.
For generating new (research) ideas		This use of GenAI is allowed except when it is prohibited by the teacher or the program of study. Correctly mention the use of GenAI assistance in accordance with the instructions on the page on being transparant about the use of GenAI. **Be careful:** - Further verify in this case whether the idea is novel or not. It is likely that it is related to existing work. **If so, that existing work should be correctly referenced in the text** (without such reference you would be committing plagiarism and thus committing an irregularity). -
For generating synthetic data		Use of GenAI for generating synthetic data is allowed, **provided that it is methodologically and ethically justifiable**, except when it is prohibited by the teacher or the program of study. Always correctly mention the use of GenAI assistance in accordance with the instructions on the page on being transparant about the use of GenAI. **Be careful:** - Always **carefully evaluate** the generated synthetic data for quality and possible bias since the output is highly dependent on the quality of the data on which the models are trained.

For generating blocks of text (other than the allowed use without referencing mentioned above)		According to Article 84 of the Regulations on Education and Examinations your text should allow to correctly and properly assess your own knowledge, understanding and skills. **Therefore, inserting blocks of text without quotes and a reference to GenAI assistance in your work is not allowed.** **Be careful:** - If it is really needed to insert a block of text from a GenAI tool, for instance because of the nature of your assignment, mention it as a citation by using quotes and correctly mention the use of GenAI assistance in accordance with the instructions page on being transparant about the use of GenAI. - However, in general, such GenAI use should be kept to an **absolute minimum**; you should always check the original sources.
For generating visuals, video or audio		Use of GenAI for generating visuals, audio or video is allowed except when it is prohibited by the teacher or the program of study. **Be careful:** - If used, refer to GenAI for visuals according to the usual referencing style, following the instructions on the page on referencing GenAI. - If you work with existing visuals, audio or video, **that existing work should be correctly referenced in the text** (without such reference you would be committing plagiarism and thus an irregularity). - Explain the usage in the methods section (if there is one) and optionally attach (or link to) the prompts with the full output (or history).
Other use (specify here; this may also include a combination of types of use mentioned above):		To make sure other use of GenAI is allowed within the course or thesis, and if so, the conditions that may apply, contact the teaching staff of the course or the supervisor of the thesis **beforehand** and explain the intended GenAI use. Also inform the programme director.

		Motivate how you would comply with Article 84 of the exam regulations. Explain the use and the added value of the AI tool you consider to use and how it is in accordance with the assignment or thesis and the KU Leuven guidelines on responsible use of Generative AI tools. Depending on the kind of GenAI use, it may be needed to properly reference it in the text, in accordance with the instructions page on being transparant about the use of GenAI.

Department of Physics and Astronomy
Celestijnenlaan 200D bus 2412
3001 LEUVEN, BELGIË
tel. +32 16 32 71 24
www.fys.kuleuven.be